Advancements in Full Wavefield Migration

Hoogerbrugge, L.A.

DOI
10.4233/uuid:b429fddf-e36b-4d7f-ad95-1a2bb89eeeb2

Publication date
2025

Document Version
Final published version

Citation (APA)
Hoogerbrugge, L. A. (2025). *Advancements in Full Wavefield Migration*. [Dissertation (TU Delft), Delft University of Technology]. https://doi.org/10.4233/uuid:b429fddf-e36b-4d7f-ad95-1a2bb89eeeb2

Advancements in Full Wavefield Migration

Leo Hoogerbrugge

ADVANCEMENTS IN FULL WAVEFIELD MIGRATION

ADVANCEMENTS IN FULL WAVEFIELD MIGRATION

Dissertation

for the purpose of obtaining the degree of doctor
at Delft University of Technology
by the authority of the Rector Magnificus, prof. dr. ir. T.H.J.J. van der Hagen,
chair of the Board for Doctorates
to be defended publicly on
Wednesday, 28 May 2025 at 12:30 o'clock

by

Leonard Arie HOOGERBRUGGE

Master of Science in Applied Physics, Delft University of Technology, the Netherlands,
born in Voorburg, the Netherlands

This dissertation has been approved by the promotors.

Composition of the doctoral committee:

Rector Magnificus,	chairperson
Dr. ir. D.J. Verschuur,	Delft University of Technology, *promotor*
Dr. K.W.A. van Dongen,	Delft University of Technology, *copromotor*
Independent members:	
Prof. dr. ir. C.P.A. Wapenaar	Delft University of Technology,
Prof. dr. ir. M.B. van Gijzen	Delft University of Technology,
Prof. dr. T. van Leeuwen	Utrecht University,
Dr. P.R. Haffinger	Delft Inversion,
Dr. M. Ravasi	Shearwater Geoservices Limited,

The work in this dissertation was conducted at the Imaging Physics (ImPhys) department, Faculty of Applied Sciences, Delft University of Technology, and was financially supported by the Delphi Consortium.

Printed by: Ridderprint

ISBN 978-94-6384-781-0

An electronic copy of this dissertation is available at
https://repository.tudelft.nl/.

CONTENTS

SUMMARY

Seismic imaging is a method for generating images of the subsurface of the Earth without the need to drill down to observe it directly. Using a seismic source, high-amplitude acoustic waves are generated, which propagate through the Earth. When these waves encounter interfaces between different layers, part of their energy is reflected, traveling back upwards. At the surface, these scattered waves are recorded using an array of sensors. These recorded wavefields are then used as input for a seismic imaging algorithm, which attempts to reconstruct an accurate image of the subsurface based on these measurements.

While many different seismic imaging methods exist, this thesis focuses specifically on Full-Wavefield Migration (FWM). FWM is a least-squares migration method, based on iteratively updating the image in order to minimize the misfit between the recorded data and the forward modelled wavefield at the surface. Using this iterative approach, FWM is able to incorporate multiple scattering effects into the imaging process, increasing the accuracy of the resulting images. Also, by using explicit convolutional operators based on the one-way wave equation, the computational cost of FWM is reduced compared to alternative iterative imaging methods based on finite-difference modelling.

In this thesis, we describe a number of recent advancements to the FWM method. Our main focus is the extension of the FWM method to include converted waves. In order to take these effects into account, we need accurate reflection and transmission operators. However, the true, elastic reflection and transmission operators are notoriously non-linear, making them difficult to work with. Therefore, we introduce a novel set of approximations of these operators, which we name the extended Shuey approximations. To benchmark these approximations, we apply them in a simple, 1.5D scenario. This test shows that the extended Shuey approximations yield improved results for forward modelling and imaging, compared to the conventional Shuey approximation.

We then use these extended Shuey approximations to derive accurate reflection and transmission operators for the 2D case. Combining these operators with the existing theoretical framework of FWM we develop a robust imaging algorithm which takes converted waves into account. We then apply this algorithm, which we name elastic FWM, to two synthetic models. We show that, for these models, the elastic FWM method outperforms the conventional, acoustic FWM method. We also demonstrate that, using this method, additional information regarding the elastic medium parameters of the subsurface can be recovered.

Finally, we examine the known issue of slow convergence for the conventional, acoustic FWM algorithm. We introduce a novel preconditioner, based on approximating the pseudo-inverse using Proper Orthogonal Decomposition (POD). Using this preconditioner, we demonstrate improved convergence for the synthetic Marmousi model and a field data set from the Vøring basin in Norway.

SAMENVATTING

Seismische beeldvorming is een methode om afbeeldingen van de ondergrond van de aarde te maken zonder boringen uit te voeren om deze direct waar te nemen. Met een seismische bron worden akoestische golven met een hoge amplitude opgewekt, die door de aarde propageren. Wanneer deze golven overgangen tussen verschillende aardlagen tegenkomen wordt een deel van hun energie gereflecteerd en naar boven gepropageerd. Aan het oppervlak worden deze verstrooide golven opgenomen door een reeks sensoren. Deze opgenomen geluidsgolven worden vervolgens als input gebruikt voor een seismisch afbeeldingsalgoritme, welk probeert een accurate afbeelding te reconstrueren van de ondergrond op basis van deze metingen.

Hoewel er vele verschillende seismisch afbeeldingsalgoritmes bestaan, zal deze thesis zich specifiek concentreren op Full-Wavefield Migration (FWM). FWM is een zogeheten kleinste-kwadraten migratie methode, die gebaseerd zijn op het iteratief bijwerken van de afbeelding om het verschil te minimaliseren tussen de opgenomen data en het voorwaarts gemodelleerde golfveld aan de oppervlakte. Door gebruik te maken van deze iteratieve aanpak is FWM in staat om meervoudige-verstrooiingseffecten in het afbeeldingsproces op te nemen, wat leidt tot een verbeterde nauwkeurigheid van de afbeeldingen. Tevens zijn de computationele kosten van FWM, door het gebruik van operatoren gebaseerd op expliciete convoluties op basis van de een-weg golfvergelijking, verminderd ten opzichte van alternatieve afbeeldingsmethodes gebaseerd op eindige-differentie methodes.

In deze thesis beschrijven we een aantal recente vorderingen in de FWM afbeeldingsmethode. Onze voornaamste focus is de uitbreiding van FWM om geconverteerde golven mee te nemen. Om deze effecten in ogenschouw te nemen hebben we accurate reflectie en transmissie operatoren nodig. De echte, elastische reflectie en transmissie operatoren zijn echter notoir niet-lineair, wat ze moeilijk in het gebruik maakt. Daarom introduceren we een nieuwe set benaderingen voor deze operatoren, die we de uitgebreide Shuey benaderingen noemen. Om deze benaderingen te toetsen, passen we ze toe op een eenvoudig, 1.5D scenario. Deze toets laat zien dat de uitgebreide Shuey benaderingen een beter resultaat opleveren voor voorwaartse modellering en inversie, ten opzichte van de conventionele Shuey benadering.

Vervolgens gebruiken we deze uitgebreide Shuey benaderingen om accurate reflectie en transmissie operatoren af te leiden voor de 2D situatie. Door deze operatoren te combineren met het theoretische raamwerk van FWM ontwikkelen we een robuust afbeeldingsalgoritme dat rekening houdt met geconverteerde golven. Vervolgens passen we dit algoritme, dat we elastische FWM noemen, toe op twee synthetische modellen. We laten zien dat, voor deze modellen, elastische FWM beter presteert dan de conventionele, akoestische FWM methode. We laten ook zien dat met deze methode aanvullende informatie over de elastische parameters van de ondergrond kan worden bepaald.

Als laatste bekijken we het bekende probleem van langzame convergentie voor het conventionele, akoestische FWM algoritme. We introduceren een nieuwe preconditioner, gebaseerd op het benaderen van de pseudo-inverse door gebruik van Proper Orthogonal Decomposition (POD). Door gebruik te maken van deze preconditioner behalen we een verbeterde convergentie voor het synthetische Marmousi model als ook voor een veld dataset afkomstig van het Vøring basin in Noorwegen.

1

INTRODUCTION

1.1. SEISMIC IMAGING

Seismic imaging is a method for generating images of the subsurface of the Earth, based on measurements usually taken at the surface. The goal is to gather information about the subsurface without having to drill down into the Earth to observe it directly. In this sense, the goals of seismic imaging are similar to the goals of medical imaging, where one wishes to image part of a patient's body without having to perform invasive surgeries to examine the region directly. Much of the process of seismic imaging is analogous to the process of medical ultrasound imaging, for example. Both begin by taking measurements of the region of interest using acoustic waves. Once the measurement is performed, an imaging algorithm is applied to the data to obtain an image of the region of interest, as shown in figure 1.1. Finally, using the resulting image, alongside other information, relevant conclusions can be drawn about the region being imaged.

The main difference between seismic imaging and medical imaging is the area to which it is applied. Seismic imaging was originally developed for the discovery of hydrocarbon resources, i.e. oil and gas fields, within the subsurface. As these fields

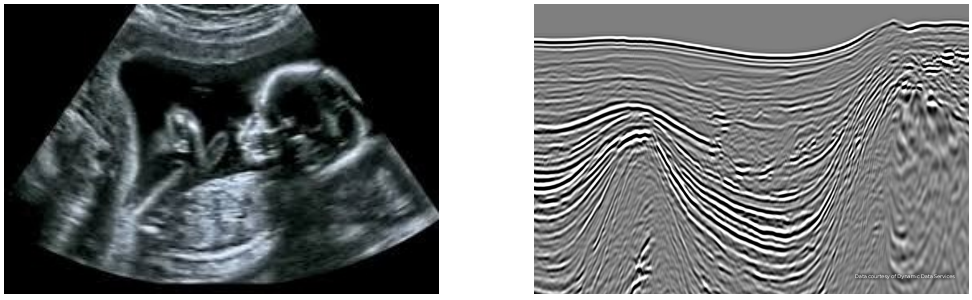

(a) (b)

Figure 1.1: An example of an ultrasound image of a baby [1] (left) and an example of a seismic image of the Earth [2] (right).

1

are often located deep within the subsurface, as illustrated in figure 1.2, drilling down to these areas is costly. The cost of drilling a single oil well is in the order of 10 million USD [3], and may be up to an order of magnitude more in challenging areas [4]. To mitigate the risks of drilling a so-called 'dry' well, where no oil or gas is found, seismic imaging methods are applied to explore the prospective drilling site. Note that, even with modern, sophisticated techniques, more than 50% of exploration wells are still dry [5]. This illustrates the need for the development of more precise seismic imaging techniques.

Seismic imaging is not limited to hydrocarbon exploration, however. Due to the energy transition, the need for oil and gas exploration is decreasing, while other applications are becoming feasible. An example of this development has been the application of seismic imaging techniques to perform site characterization for offshore wind farms [7]. In a similar vein, seismic imaging is used in carbon capture and storage programs to monitor storage sites [8], as these are often located in depleted gas fields. Locating geothermal reservoirs is another application where seismic imaging has been used [9], as many of the principles of locating geothermal

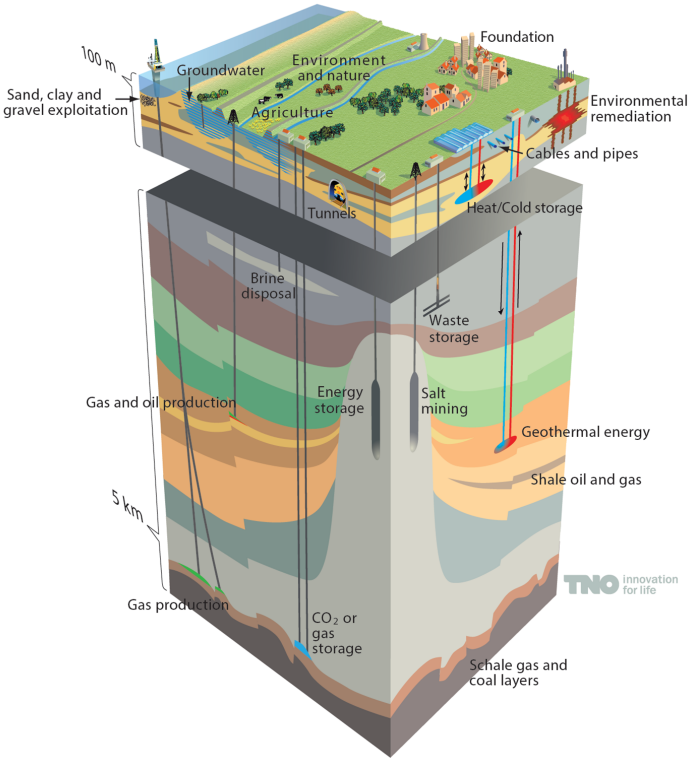

Figure 1.2: Diagram showing the relative depths of different regions of interest within the subsurface [6].

wells are similar to those of locating oil and gas wells. Finally, techniques originating from seismic imaging in complex media have also been applied to medical ultrasound imaging, as the underlying physics of the propagation and scattering of acoustic waves is the same for both fields [10]. As the medical ultrasound community moves towards the imaging of areas containing large contrasts, such as bones and the skull, these techniques are becoming increasingly important within that field [11].

Let us now examine the different elements of the seismic imaging process in more detail, beginning with the acquisition of seismic data. First, using a seismic source, high-amplitude acoustic waves are generated, which travel into the subsurface. This source may take the form of a truck with a heavy vibrating plate for measurements on land, or an air gun, which produces acoustic waves by releasing compressed air [13], for measurements on water. The waves generated by this source propagate through the subsurface, encountering interfaces between different geological layers. At these interfaces, part of the energy of the wave is reflected, leading to waves traveling back up towards the surface. At the surface, these reflected waves are recorded using an array of sensors, called geophones, if the measurements are on land, or hydrophones, if they are on water. This process is illustrated in figure 1.3.

While the topic of seismic acquisition is outside the scope of this thesis, it is non-trivial to generate high-quality seismic data in this manner, and therefore significant research is done into the process of collecting this data. This is of note, as without the availability of high-quality seismic data, many of the more complicated imaging techniques, such as those described in section 1.2, cannot function. Also note that within the field of seismic acquisition, multiple alternative methods exist to acquire seismic data compared to the description given above. For example, instead of an 'active' source located at the surface, 'passive' sources, based on naturally occurring seismic activity within the subsurface, can be used instead [14]. Also, additional information, such as gravity and electromagnetic measurements, can

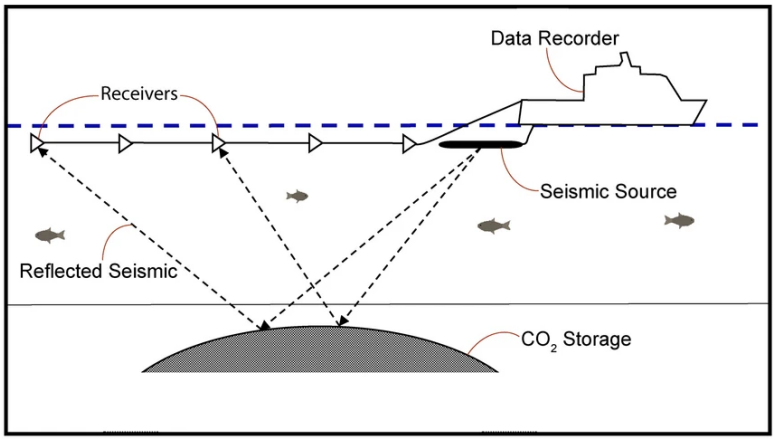

Figure 1.3: Marine seismic acquisition setup [12].

be used alongside conventional acoustic measurements in so-called multi-physics imaging setups [15].

After a set of measurements has been acquired, the next step in seismic imaging is to apply an imaging algorithm to recover an image of the subsurface. This step, often referred to as 'migration' within the seismic imaging community, will be the focus of the rest of this thesis. An overview of the existing literature on migration methods is given in section 1.2. Finally, after an image has been generated, conclusions must be drawn about the region of interest. As the images produced by seismic imaging techniques generally only provide structural information, the underlying medium properties must be inferred using additional geological data. This process, commonly referred to as 'interpretation', falls outside the scope of this thesis.

1.2. IMAGING ALGORITHMS

In this section, we will give a general, mostly chronological, overview of the different imaging algorithms used in seismic imaging. In the very early days of seismic imaging, no imaging algorithms were used at all. Instead, operators in the field would attempt to interpret the recorded wavefields directly [16]. While this approach gave rudimentary information about the subsurface, it was quickly realized that higher degrees of accuracy could be achieved by using some form of imaging. One of the first true seismic imaging algorithms was developed in the 1950's by Hagedoorn [17], who used Huygens' principle to determine the total travel time of recorded events. With this approach, reflecting surfaces within the subsurface could be mapped. Using similar principles, the method of common midpoint (CMP) stacking [18] was developed. In this method, events are sorted by the midpoint between source and receiver, after which a travel time correction, referred to as normal moveout (NMO) correction, is applied. After NMO correction is applied, the events are summed together, generating an image of the reflectivity at each midpoint. While this method relies on strong assumptions, most noticeably assuming that all the layers in the subsurface are flat, it is highly efficient and surprisingly robust, and is still used as a baseline for comparison with other imaging methods [19].

As computers became more powerful, more advanced imaging techniques were developed. The main advancement in this period was the application of wave equation principles by Claerbout [20]. Claerbout realized that, in cases where the source was known, one can extrapolate the source wavefield forward in time to model the incident wavefield at each point in the medium. Using the same principles, one can also propagate the recorded wavefield *backwards* in time, modelling the scattered wavefield at each point in the medium. Using these two wavefields, one can finally apply the imaging condition, which states that at every point where the incident and scattered wavefields meet, there must be a reflector. More formally, the imaging condition states that a reflector must exist at each point where the correlation between the incident and scattered wavefields is non-zero. Using these principles, more accurate images can be made of the subsurface, most noticeably in areas with lateral variations in the velocity profile.

In order to get around the limitations of computers at the time, Claerbout also

introduced the concept of wavefield separation. By separating the total wavefield into up- and downgoing components, one-way propagation methods could be used, reducing the computational cost of the method compared to full, two-way modelling. While Claerbout's original method of one-way propagation was based on finite-difference methods, in later years, this approach was reformulated into an integral approach by Berkhout [21]. Using Green's functions, Berkhout was able to formulate explicit convolutional operators for one-way propagation. In recent years, due to increasing computational power, the full, two-way, modelling of wavefields has become feasible. This has led to the development of reverse-time migration (RTM) [22, 23], which solves the full, two-way wave equation to model the wavefields. Using this approach, regions with strongly dipping reflectors and strong diving waves can be imaged, which is challenging when using one-way wave propagation methods.

The most recent advancement in imaging methods has been the introduction of least-squares migration (LSM) techniques, first introduced by Nemeth [24]. With LSM, the full propagation and scattering of the wavefield throughout the medium is modelled in order to generate modelled data at the surface, where it is compared to the true, measured data. The difference between these two wavefields, called the residual, is then propagated backwards into the medium. Finally, using the backpropagated residual, the reflectivity at each point in the medium is updated. This process is then repeated as many times as desired, leading to an update of the reflectivity at each iteration. This iterative approach has multiple advantages, the main one being that it allows acquisition issues such as missing receivers and variations in illumination to be compensated. Based on these principles, several powerful imaging algorithms have been developed. The most well-known of these is least-squares RTM (LS-RTM) [25], an iterative extension to the conventional RTM approach. Another example is Full-Wavefield Migration (FWM) [26], an iterative imaging algorithm using one-way operators, which we will explore in more detail in section 1.3.

Note that, as imaging algorithms have become more sophisticated, the need for an accurate velocity model has also increased. In a conventional imaging workflow, it is assumed that a (kinematically) accurate velocity model exists, which is used as an input for imaging. In recent years, however, this velocity estimation step has increasingly been incorporated into the imaging algorithm itself, often by iteratively updating both the velocity and reflectivity model simultaneously. The most well-known example in this field is Full Waveform Inversion (FWI) [27, 28], which attempts to reconstruct the underlying medium properties directly. In situations where this approach is not feasible, combined velocity estimation and imaging algorithms are commonly used. Examples of these algorithms are Reflection Waveform Inversion (RWI) [29, 30] and Joint Migration Inversion (JMI) [31, 32]. As this thesis focuses on imaging, detailed examinations of these methods are outside the scope of this thesis. However, it is important to note that generating an accurate velocity model is an essential step in generating an accurate image of the subsurface.

1

1.3. FULL-WAVEFIELD MIGRATION

This thesis focuses mainly on the method of Full-Wavefield Migration (FWM). FWM is a LSM method originally developed by Berkhout [33, 34] and expanded on by others [26, 35]. The method is based on one-way propagators, represented by the convolutional operators **W** [21].

FWM has a number of advantages compared to other popular imaging methodologies. In particular, while many imaging methodologies struggle with multiple scattering events, FWM incorporates primary and multiple scattering in a single, unified framework. In seismic imaging, two types of multiple scattering events, commonly referred to as 'multiples', are generally present in the data, as illustrated in figure 1.4. The first type are called surface multiples, represented by the blue lines in figure 1.4, where the wavefield reflects at the surface of the medium and travels back into the subsurface. The second type are called internal multiples, represented by the green lines in figure 1.4, where an upgoing wavefield reflects downwards at an interface in the subsurface. If these multiple scattering events are not accounted for in the imaging step, additional, spurious reflectors are generated within the image, reducing the quality of the final image. To avoid this problem, multiple-removal techniques are often applied to the data in an effort to remove these events from the measured data [36, 37]. FWM, however, takes these events into account by incorporating these multiples into its imaging algorithm. This makes the method more robust with respect to multiples, as well as providing additional illumination in areas that may not be reached by primary events [38].

An additional advantage of FWM compared to other LSM techniques is its relatively low computational cost. As FWM utilizes one-way propagators in an integral approach, it is computationally much less expensive compared to a method such as LS-RTM, which utilizes finite-difference modelling. Specifically, due to the use of integral-based operators, the underlying grid used in FWM can be made much coarser compared to the grids utilized in finite-difference modelling methods,

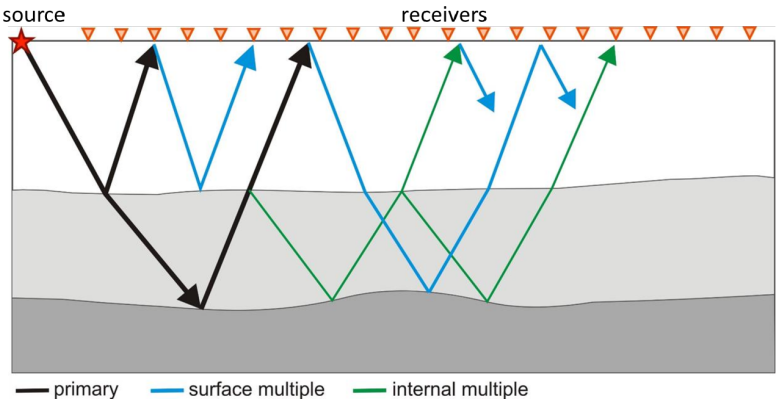

Figure 1.4: Diagram showing the wavepaths of primaries (black), surface multiples (blue) and internal multiples (green) [39].

drastically reducing computational times. This effect is particularly noticeable in areas with low velocities, as these areas require very fine grids in finite-difference setups. This makes FWM especially good in taking converted waves into account [33, 34], as the low velocities associated with converted wave events pose a particular challenge in finite-difference frameworks.

Finally, due to the use of explicit operators within the FWM framework, one can choose which effects to take into account and which to ignore in each part of the model. Specifically, one can choose to use simple, angle-independent, acoustic imaging methods for the overburden, while still accurately modelling the wavepaths at the reservoir level, for example [40]. In this manner, a balance between computational efficiency and accuracy can be achieved. In finite-difference based approaches, by contrast, all scattering and propagation effects are modelled automatically. While in principle this is an advantage, it also requires one to take all effects into account throughout the entire subsurface, increasing the computational cost unnecessarily in areas of the model where the geometry is relatively simple.

However, FWM also faces a number of challenges. First of all, in certain cases the method can suffer from slow convergence. To address this issue, pre-conditioning can be applied in the inversion process [41]. Secondly, when applied in combination with velocity estimation, FWM struggles to accurately model the full, angle-dependent reflectivity [42]. This is due to an overparameterisation of the problem in these cases. Finally, because of the use of one-way operators, the method struggles to image areas containing steep reflectors or strong diving waves. While certain strategies have been proposed to extend the FWM framework to an omni-directional approach that takes these effects into account [43, 44], it remains challenging to incorporate these effects in FWM.

1.4. THESIS OUTLINE

In this thesis, we present a number of recent advancements within FWM, with a focus on the modelling and imaging of converted waves. Specifically, we will attempt to answer the following research questions:

- *Can we accurately incorporate the reflection and transmission coefficients for elastic wave propagation in a forward and inverse modelling scheme?*

  To answer this question, in chapter 2 we present a novel set of accurate approximations to the full set of elastic reflection and transmission coefficients, which we name the extended Shuey's approximations. These extended approximations are based on applying Taylor expansions to the so-called Zoeppritz equations. We show that the results of these approximations reduce to the well-known Shuey's approximation in the linear case. In addition, we show how Shuey's approximation can be extended to retrieve more accurate approximations for both the PP-reflection coefficient as well as the other reflection and transmission coefficients. We then apply these approximations to a simple forward and inverse modelling scenario to give a proof-of-concept of how these approximations can improve the accuracy of modelling wave conversions in practice.

- *Can we extend the 2D FWM algorithm to include converted wave effects?*

  To make this extension, in chapter 3 we combine the extended Shuey approximations of chapter 2 with the theoretical framework developed by Berkhout [33] to formulate a robust algorithm for the forward and inverse modelling of converted waves in FWM. We show that this approach reduces the number of parameters required to accurately describe the angle-dependent reflection and transmission operators compared to traditional, angle-dependent FWM approaches, thereby avoiding over-parametrization. We then test the algorithm on synthetic data of a model with flat reflectors as well as on a model containing a lens-shaped anomaly and compare the results to the results obtained by acoustic FWM.

- *Can we improve the convergence of the 2D, acoustic FWM algorithm?*

  To investigate this, in chapter 4 we present a novel preconditioner for acoustic FWM, based on approximating the pseudo-inverse using Proper Orthogonal Decomposition (POD) [45]. The preconditioned FWM algorithm, which we call Model-Order Reduced FWM (MOR-FWM), is tested on both the synthetic Marmousi model as well as on a field dataset from the Vøring basin.

A summary of the work done and the conclusions drawn based on the results are presented in chapter 5. In this chapter, we also give our recommendations for future work on the FWM method.

REFERENCES

[1] R. Ghauri. *What is medical ultrasound?* Accessed: 2024-12-10. URL: https://www.linkedin.com/pulse/what-medical-ultrasound-rustam-ghauri.

[2] DUG. *Seismic Processing*. Accessed: 2024-11-22. URL: https://dug.com/geoscience-services/seismic-processing.

[3] M. Z. Lukawski, B. J. Anderson, C. Augustine, L. E. Capuano, K. F. Beckers, B. Livesay, and J. W. Tester. "Cost analysis of oil, gas, and geothermal well drilling". In: *Journal of Petroleum Science and Engineering* 118 (2014), pp. 1–14. DOI: https://doi.org/10.1016/j.petrol.2014.03.012.

[4] L. Amado. "Chapter 12 - Field Case Evaluations". In: *Reservoir Exploration and Appraisal*. Boston: Gulf Professional Publishing, 2013, pp. 53–156. ISBN: 978-1-85617-853-2. DOI: https://doi.org/10.1016/B978-1-85617-853-2.00012-0. URL: https://www.sciencedirect.com/science/article/pii/B9781856178532000120.

[5] T. A. O. Ganat. *Technical Guidance for Petroleum Exploration and Production Plans*. Cham, Switzerland: Springer, 2020. ISBN: 9783030452506.

[6] NLOG. *Spatial Planning*. Accessed: 2024-11-22. URL: https://www.nlog.nl/en/spatial-planning.

[7] S. Kreiter, T. Mörz, J. Metzen, D. Hepp, B. Ossig, D. Otto, L. Socko, H. Keil, V. Spiess, and D. Hebbeln. "Site characterization of foundation soil for Offshore Wind Farms - an example from the German North Sea". In: *Geophysical Research Abstracts*. Vol. 12. EGU General Assembly. May 2010.

[8] M. Fawad and N. H. Mondol. "Monitoring geological storage of CO2: a new approach". In: *Scientific Reports* 11.1 (Mar. 2021). ISSN: 2045-2322. DOI: 10.1038/s41598-021-85346-8. URL: http://dx.doi.org/10.1038/s41598-021-85346-8.

[9] Q. Yasin, A. Gholami, M. Majdański, B. Liu, and N. Golsanami. "Seismic characterization of geologically complex geothermal reservoirs by combining structure-oriented filtering and attributes analysis". In: *Geothermics* 112 (2023). ISSN: 0375-6505. DOI: https://doi.org/10.1016/j.geothermics.2023.102749. URL: https://www.sciencedirect.com/science/article/pii/S0375650523001037.

[10] U. Taskin. "Full-Waveform Inversion for Breast Ultrasound". PhD thesis. Delft University of Technology, 2021. DOI: 10.4233/UUID:A8C89EB8-B60F-4904-8425-F38FCB956A15. URL: http://resolver.tudelft.nl/uuid:a8c89eb8-b60f-4904-8425-f38fcb956a15.

[11] G. Renaud, J. L. Johnson, and D. Cassereau. “Real-time Kirchhoff migration for ultrasound imaging of the bone cortex”. In: *SEG Technical Program Expanded Abstracts 2018*. Society of Exploration Geophysicists, Aug. 2018, pp. 4797–4801. DOI: 10.1190/segam2018-2996779.1. URL: http://dx.doi.org/10.1190/segam2018-2996779.1.

[12] M. Fawad and N. H. Mondol. “Monitoring geological storage of CO2: a new approach”. In: *Scientific Reports* 11.1 (Mar. 2021). ISSN: 2045-2322. DOI: 10.1038/s41598-021-85346-8. URL: http://dx.doi.org/10.1038/s41598-021-85346-8.

[13] L. Amundsen and M. Landrø. “Marine Seismic Sources”. In: *Geo Expro* (Feb. 2010).

[14] B. Artman. “Imaging passive seismic data”. In: *GEOPHYSICS* 71.4 (July 2006), SI177–SI187. ISSN: 1942-2156. DOI: 10.1190/1.2209748. URL: http://dx.doi.org/10.1190/1.2209748.

[15] Y. Huang, A. Abubakar, D. Colombo, K. Gao, J.-H. Kim, M. Mantovani, M. Meju, C. Shin, A. Vesnaver, R. Yan, P. Yu, and L. Zhang. “Introduction to special section: Multiphysics imaging for exploration and reservoir monitoring”. In: *Interpretation* 6.3 (Aug. 2018), SGi–SGii. ISSN: 2324-8866. DOI: 10.1190/int-2018-0713-spseintro.1. URL: http://dx.doi.org/10.1190/INT-2018-0713-SPSEINTRO.1.

[16] J. B. Bednar. “A brief history of seismic migration”. In: *GEOPHYSICS* 70.3 (May 2005), 3MJ–20MJ. ISSN: 1942-2156. DOI: 10.1190/1.1926579. URL: http://dx.doi.org/10.1190/1.1926579.

[17] J. G. Hagedoorn. “A PROCESS OF SEISMIC REFLECTION INTERPRETATION”. In: *Geophysical Prospecting* 2.2 (June 1954), pp. 85–127. ISSN: 1365-2478. DOI: 10.1111/j.1365-2478.1954.tb01281.x. URL: http://dx.doi.org/10.1111/j.1365-2478.1954.tb01281.x.

[18] W. H. Mayne. “COMMON REFLECTION POINT HORIZONTAL DATA STACKING TECHNIQUES”. In: *GEOPHYSICS* 27.6 (Dec. 1962), pp. 927–938. ISSN: 1942-2156. DOI: 10.1190/1.1439118. URL: http://dx.doi.org/10.1190/1.1439118.

[19] S. H. Gray. “4. Seismic imaging”. In: *Encyclopedia of Exploration Geophysics*. Society of Exploration Geophysicists, Jan. 2014, S1–1–S1–16. ISBN: 9781560803027. DOI: 10.1190/1.9781560803027.entry4. URL: http://dx.doi.org/10.1190/1.9781560803027.entry4.

[20] J. F. Claerbout. “TOWARD A UNIFIED THEORY OF REFLECTOR MAPPING”. In: *GEOPHYSICS* 36.3 (June 1971), pp. 467–481. ISSN: 1942-2156. DOI: 10.1190/1.1440185. URL: http://dx.doi.org/10.1190/1.1440185.

[21] A. J. Berkhout. *Seismic migration: Imaging of Acoustic Energy by Wave Field Extrapolation*. Elsevier, 1984.

[22] E. Baysal, D. D. Kosloff, and J. W. C. Sherwood. “Reverse time migration”. In: *GEOPHYSICS* 48.11 (Nov. 1983), pp. 1514–1524. ISSN: 1942-2156. DOI: 10.1190/1.1441434. URL: http://dx.doi.org/10.1190/1.1441434.

[23] H.-W. Zhou, H. Hu, Z. Zou, Y. Wo, and O. Youn. "Reverse time migration: A prospect of seismic imaging methodology". In: *Earth-Science Reviews* 179 (Apr. 2018), pp. 207–227. ISSN: 0012-8252. DOI: 10.1016/j.earscirev.2018.02.008. URL: http://dx.doi.org/10.1016/j.earscirev.2018.02.008.

[24] T. Nemeth, C. Wu, and G. T. Schuster. "Least-squares migration of incomplete reflection data". In: *GEOPHYSICS* 64.1 (Jan. 1999), pp. 208–221. ISSN: 1942-2156. DOI: 10.1190/1.1444517. URL: http://dx.doi.org/10.1190/1.1444517.

[25] W. Dai, P. Fowler, and G. T. Schuster. "Multi-source least-squares reverse time migration". In: *Geophysical Prospecting* 60.4 (June 2012), pp. 681–695. ISSN: 1365-2478. DOI: 10.1111/j.1365-2478.2012.01092.x. URL: http://dx.doi.org/10.1111/j.1365-2478.2012.01092.x.

[26] M. Davydenko and D. J. Verschuur. "Full-wavefield migration: using surface and internal multiples in imaging". In: *Geophysical Prospecting* 65.1 (Feb. 2016), pp. 7–21. ISSN: 1365-2478. DOI: 10.1111/1365-2478.12360. URL: http://dx.doi.org/10.1111/1365-2478.12360.

[27] J. Virieux and S. Operto. "An overview of full-waveform inversion in exploration geophysics". In: *GEOPHYSICS* 74.6 (Nov. 2009), WCC1–WCC26. ISSN: 1942-2156. DOI: 10.1190/1.3238367. URL: http://dx.doi.org/10.1190/1.3238367.

[28] A. Tarantola. *Inverse problem theory: Methods for data fitting and model parameter estimation*. Elsevier Science Publ. Co., Inc, 1987.

[29] S. Xu, D. Wang, F. Chen, G. Lambaré, and Y. Zhang. "Inversion on Reflected Seismic Wave". In: *SEG Technical Program Expanded Abstracts 2012*. Society of Exploration Geophysicists, Sept. 2012. DOI: 10.1190/segam2012-1473.1. URL: http://dx.doi.org/10.1190/segam2012-1473.1.

[30] S. Abolhassani and E. Verschuur. "High-Resolution One-Way Reflection Waveform Inversion". In: *84th EAGE Annual Conference & Exhibition*. European Association of Geoscientists & Engineers, 2023, pp. 1–5. DOI: 10.3997/2214-4609.202310517. URL: http://dx.doi.org/10.3997/2214-4609.202310517.

[31] X. Staal. "Combined imaging and velocity estimation by Joint Migration Inversion". PhD thesis. Delft University of Technology, 2015. DOI: 10.4233/UUID:F9CFA765-DAC4-4954-9B6B-01B8C7345018. URL: http://resolver.tudelft.nl/uuid:f9cfa765-dac4-4954-9b6b-01b8c7345018.

[32] A. J. Berkhout. "Review Paper: An outlook on the future of seismic imaging, Part III: Joint Migration Inversion". In: *Geophysical Prospecting* 62.5 (Aug. 2014c), pp. 950–971. ISSN: 1365-2478. DOI: 10.1111/1365-2478.12158. URL: http://dx.doi.org/10.1111/1365-2478.12158.

[33] A. J. Berkhout. "Review Paper: An outlook on the future of seismic imaging, Part I: forward and reverse modelling". In: *Geophysical Prospecting* 62.5 (Aug. 2014a), pp. 911–930. ISSN: 1365-2478. DOI: 10.1111/1365-2478.12161. URL: http://dx.doi.org/10.1111/1365-2478.12161.

[34] A. J. Berkhout. “Review Paper: An outlook on the future of seismic imaging, Part II: Full-Wavefield Migration”. In: *Geophysical Prospecting* 62.5 (Aug. 2014b), pp. 931–949. ISSN: 1365-2478. DOI: 10.1111/1365-2478.12154. URL: http://dx.doi.org/10.1111/1365-2478.12154.

[35] A. Nath and D. J. Verschuur. “Imaging with surface-related multiples to overcome large acquisition gaps”. In: *Journal of Geophysics and Engineering* (July 2020). ISSN: 1742-2140. DOI: 10.1093/jge/gxaa027. URL: http://dx.doi.org/10.1093/jge/gxaa027.

[36] D. J. Verschuur, A. J. Berkhout, and C. P. A. Wapenaar. “Adaptive surface-related multiple elimination”. In: *GEOPHYSICS* 57.9 (Sept. 1992), pp. 1166–1177. ISSN: 1942-2156. DOI: 10.1190/1.1443330. URL: http://dx.doi.org/10.1190/1.1443330.

[37] D. Zhang. “Surface-related multiple estimation and removal with focus on shallow water”. PhD thesis. Delft University of Technology, 2022. DOI: 10.4233/UUID:B46B14E3-C0CF-4ACA-A21D-B7EEDA6EB2DF. URL: http://resolver.tudelft.nl/uuid:b46b14e3-c0cf-4aca-a21d-b7eeda6eb2df.

[38] Y. Liu, X. Chang, D. Jin, R. He, H. Sun, and Y. Zheng. “Reverse time migration of multiples for subsalt imaging”. In: *GEOPHYSICS* 76.5 (Sept. 2011), WB209–WB216. ISSN: 1942-2156. DOI: 10.1190/geo2010-0312.1. URL: http://dx.doi.org/10.1190/geo2010-0312.1.

[39] P. Y. Raya and W. W. Weibull. *Seismic imaging with primaries and multiples*. 2019. URL: https://api.semanticscholar.org/CorpusID:209006012.

[40] A. Garg and D. J. Verschuur. “From surface seismic data to reservoir elastic parameters using a full-wavefield redatuming approach”. In: *Geophysical Journal International* 221.1 (Dec. 2019), pp. 115–128. ISSN: 1365-246X. DOI: 10.1093/gji/ggz557. URL: http://dx.doi.org/10.1093/gji/ggz557.

[41] S. Abolhassani, L. Hoogerbrugge, and D. J. Verschuur. “One-way reflection waveform inversion with depth-dependent gradient preconditioning”. In: *Geophysical Journal International* (Nov. 2024). ISSN: 1365-246X. DOI: 10.1093/gji/ggae397. URL: http://dx.doi.org/10.1093/gji/ggae397.

[42] S. Qu. “Simultaneous joint migration inversion as a high-resolution time-lapse imaging method for reservoir monitoring”. PhD thesis. Delft University of Technology, 2020. DOI: 10.4233/UUID:F22C0DA3-9D85-4C3A-9C07-949E242869D6. URL: http://resolver.tudelft.nl/uuid:f22c0da3-9d85-4c3a-9c07-949e242869d6.

[43] M. Davydenko. “Full wavefield migration: Seismic imaging using multiple scattering effects”. PhD thesis. Delft University of Technology, 2016. DOI: 10.4233/UUID:1CDA75D5-8998-49FE-997E-B38C9B7F8B8B. URL: http://resolver.tudelft.nl/uuid:1cda75d5-8998-49fe-997e-b38c9b7f8b8b.

[44] S. Masaya. “Seismic imaging based on Joint Migration Inversion”. PhD thesis. Delft University of Technology, 2018. DOI: 10.4233/UUID:4B348428-50DC-4594-90F0-FC1BF90661A2. URL: http://resolver.tudelft.nl/uuid:4b348428-50dc-4594-90f0-fc1bf90661a2.

[45] B. Moore. “Principal component analysis in linear systems: Controllability, observability, and model reduction”. In: *IEEE Transactions on Automatic Control* 26.1 (Feb. 1981), pp. 17–32. ISSN: 0018-9286. DOI: 10.1109/tac.1981.1102568. URL: http://dx.doi.org/10.1109/TAC.1981.1102568.

2

EXTENDING SHUEY'S APPROXIMATION USING TAYLOR EXPANSIONS FOR FORWARD AND INVERSE MODELLING

As seismic imaging moves towards the imaging of more complex media, properly modelling elastic effects in the subsurface is becoming of increasing importance. In this context, elastic wave conversion, where acoustic, pressure (P-) waves are converted into elastic, shear (S-) waves, is of great importance. Accounting for these wave conversions, in the framework of forward and inverse modelling of elastic waves, is crucial to creating accurate images of the subsurface in high-contrast, elastic media. The underlying mechanism of wave conversion is well understood and described by the Zoeppritz equations. However, as these equations are highly non-linear, approximations are commonly used. The most well-known of these approximations is Shuey's approximation. However, this approximation only holds for small angles and small contrasts, making it insufficient for realistic forward and inverse modelling scenarios, where angles and contrasts may be large. In this paper we present a novel set of approximations, based on Taylor expansions of the Zoeppritz equations, which we name the extended Shuey approximations. We examine the quality of these approximations to the Zoeppritz equations and compare them to existing approximations described in literature. For a first demonstration. we apply these extended Shuey approximations to the elastic Full-Wavefield Modelling algorithm for a simple, synthetic, 1.5D example, where we show that we can accurately model the P- and S-wavefields in a forward modelling case. Finally, we apply our approximations

This chapter is based on the paper: L. Hoogerbugge, K.W.A. van Dongen and D.J. Verschuur. "Extending Shuey's approximation using Taylor expansions for forward and inverse modelling". In: Geophysical Journal International 241(2) (April 2025), pp. 876–890.

to the elastic Full-Wavefield Migration algorithm for a simple, synthetic, 1.5D example, where we show that we can recover an accurate image in an inverse modelling case.

2

2.1. INTRODUCTION

Properly modelling the propagation and scattering of elastic waves throughout the subsurface of the Earth is an important aspect in many seismic applications. In this context, the process of wave conversion, which occurs due to the elastic nature of the Earth's subsurface, has received increased interest in recent years. Wave conversion is a process where acoustic, pressure waves, known as P-waves, convert into elastic, shear waves, known as S-waves. This conversion takes place when a wavefield strikes an interface between two different media. This process is highly relevant in multiple areas, such as subsurface imaging in complex media, anisotropy analysis and reservoir characterization [1].

The underlying mechanism by which wave conversion occurs is well understood in literature, and exact reflection and transmission coefficients can be derived for flat interfaces between two media. These exact reflection and transmission coefficients are known as the Zoeppritz equations (see [2] and [3]). However, while these equations are exact, they are also notoriously difficult to work with. This is due to the non-linearity of the Zoeppritz equations, which presents itself in two different ways. First of all, the Zoeppritz equations depend on the medium properties of the two media in a very non-linear fashion. This makes it difficult to use these equations in inversion settings, where one wishes to recover the medium properties from the measurement data. Secondly, as an additional complication, the Zoeppritz equations need to account for critical angles, where the reflection and transmission coefficients diverge, which can cause a multitude of issues.

Due to these challenges, when working with the Zoeppritz equations in practice, approximations are commonly applied. By far the most well-known of these approximations is Shuey's approximation [4]. With Shuey's approximation the Zoeppritz equations are linearised, which makes them simple to invert, and removes the critical points from the Zoeppritz equations. Due to this ease of inversion, it has become the standard in amplitude variation with offset (AVO) analysis. However, Shuey's approximation is only accurate for small angles and weak contrasts, which limits its applicability. Also, it only describes the PP-reflection coefficient, which means that wave conversions are not taken into account.

To address these issues, alternative approximations have been developed. The most influential of these alternative approximations are the linearized approximations of Aki and Richards [3]. These approximations do address wave conversions, extending their applicability. However, these approximations are also only applicable in situations where the contrasts are weak. Other approximations, such as by Wang [5], have also been developed. However, most of these approximations focus on the PP-reflection coefficient, as this coefficient has been of the most interest historically.

In recent years, the forward and inverse modelling of wave-paths including wave conversions have become of greater interest. As the focus of seismic imaging shifts towards more challenging scenarios, specifically those with strong reflectors [6], or

towards cases where the goal is the recovery of the elastic parameters [7], it is important to accurately describe these wave conversions. To do this, high quality approximations of the full set of Zoeppritz equations are required.

In this paper, we present a novel set of accurate approximations to the full set of Zoeppritz equations, which we name the extended Shuey's approximations, based on applying Taylor expansions to the Zoeppritz equations. We show that the result of this approximation reduces to the well-known Shuey's approximation in the linear case. In addition, we show how it can be extended to retrieve more accurate approximations for both the PP-reflection coefficient as well as the other reflection and transmission coefficients. We then apply our approximation to a simple forward and inverse modelling scenario to give a proof-of-concept of how this approximation can improve the accuracy of modelling wave conversions in practice.

2.2. THEORY

This section is split into three parts. First, in section 2.2.1, we derive the extended Shuey's approximations, where we focus on the R_{PP} term, and show that they are a natural extension of the traditional Shuey approximation. Next, in section 2.2.2, we apply this approximation to a simple, elastic, forward modelling algorithm called elastic Full-Wavefield Modelling (FWMod). Finally, in section 2.2.3 we discuss the inverse problem associated with the forward model of section 2.2.2, referred to as elastic Full-Wavefield Migration.

2.2.1. DERIVATION OF THE EXTENDED SHUEY'S APPROXIMATIONS

We begin by deriving the extended Shuey's approximations of the Zoeppritz equations. Consider a flat, laterally invariant interface between two media located at a depth level $z = z_n$. Following the notation used in [3], each medium is characterised by its P-wave velocity α, S-wave velocity β and mass density ρ. The subscript 1 is used to denote properties within the medium above the interface (at a depth $z < z_n$), while properties within the medium below the interface (at a depth $z > z_n$) are denoted by the subscript 2.

In this situation, the reflection and transmission coefficients are given analytically by the Zoeppritz equations. As these equations are unwieldy to write down directly, we once again follow the notation used in [3] and introduce a set of intermediate variables. We begin by introducing the dimensionless contrast parameters

$$c_\alpha = \frac{\alpha_2 - \alpha_1}{\frac{1}{2}(\alpha_2 + \alpha_1)}, \; c_\beta = \frac{\beta_2 - \beta_1}{\frac{1}{2}(\beta_2 + \beta_1)}, \; c_\rho = \frac{\rho_2 - \rho_1}{\frac{1}{2}(\rho_2 + \rho_1)}. \tag{2.1}$$

Rewriting the medium parameters above and below the interface in terms of these contrast parameters gives

$$\begin{aligned} \alpha_1 &= \bar{\alpha}\left(1 - \tfrac{1}{2}c_\alpha\right), \quad \beta_1 = \bar{\beta}\left(1 - \tfrac{1}{2}c_\beta\right), \quad \rho_1 = \bar{\rho}\left(1 - \tfrac{1}{2}c_\rho\right), \\ \alpha_2 &= \bar{\alpha}\left(1 + \tfrac{1}{2}c_\alpha\right), \quad \beta_2 = \bar{\beta}\left(1 + \tfrac{1}{2}c_\beta\right), \quad \rho_2 = \bar{\rho}\left(1 + \tfrac{1}{2}c_\rho\right), \end{aligned} \tag{2.2}$$

where

$$\bar{\alpha} = \tfrac{1}{2}(\alpha_1 + \alpha_2), \quad \bar{\beta} = \tfrac{1}{2}(\beta_1 + \beta_2), \quad \bar{\rho} = \tfrac{1}{2}(\rho_1 + \rho_2). \tag{2.3}$$

Next, we introduce the intermediate variables a, b, c and d, which we write in terms of the contrast parameters c_α, c_β and c_ρ, viz.

$$\begin{aligned} a &= \bar{\rho}\tilde{a} = \bar{\rho}\left(c_\rho - \tilde{d}\hat{V}^2\sin^2(\theta)\right), & b &= \bar{\rho}\tilde{b} = \bar{\rho}\left(1 + \tfrac{1}{2}c_\rho - \tilde{d}\hat{V}^2\sin^2(\theta)\right), \\ c &= \bar{\rho}\tilde{c} = \bar{\rho}\left(1 - \tfrac{1}{2}c_\rho + \tilde{d}\hat{V}^2\sin^2(\theta)\right), & d &= \bar{\rho}\bar{\beta}^2\tilde{d} = \bar{\rho}\bar{\beta}^2\left(4c_\beta + 2c_\rho\left(1 + \tfrac{1}{4}c_\beta^2\right)\right), \end{aligned} \tag{2.4}$$

with generalized angle of incidence θ, and where we use the shorthand notation $\hat{V} = \bar{\beta}/\bar{\alpha}$. Also note the use of the ˜ symbol in equation 2.4 to indicate dimensionless variables.

In equation 2.4 we have introduced the generalized angle of incidence θ, which is defined implicitly using Snell's law, viz

$$\frac{\sin(\theta)}{\bar{\alpha}} = \frac{\sin(i_1)}{\alpha_1} = \frac{\sin(i_2)}{\alpha_2} = \frac{\sin(j_1)}{\beta_1} = \frac{\sin(j_2)}{\beta_2}, \tag{2.5}$$

where i_1 and i_2 are the angles of incidence and refraction of the P-waves in the medium above and below the interface, respectively, while j_1 and j_2 are the angles of incidence and refraction of the S-waves in the medium above and below the interface. Using equations 2.5, along with the trigonometric identity $\sin^2(\theta) + \cos^2(\theta) = 1$, we write the associated cosine terms as

$$\begin{aligned} \cos(i_1) &= \sqrt{1 - \left(1 - \tfrac{1}{2}c_\alpha\right)^2\sin^2(\theta)}, & \cos(j_1) &= \sqrt{1 - \hat{V}^2\left(1 - \tfrac{1}{2}c_\beta\right)^2\sin^2(\theta)}, \\ \cos(i_2) &= \sqrt{1 - \left(1 + \tfrac{1}{2}c_\alpha\right)^2\sin^2(\theta)}, & \cos(j_2) &= \sqrt{1 - \hat{V}^2\left(1 + \tfrac{1}{2}c_\beta\right)^2\sin^2(\theta)}. \end{aligned} \tag{2.6}$$

Next, we introduce the additional intermediate variables

$$\begin{aligned} E &= \frac{\bar{\rho}}{\bar{\alpha}}\tilde{E} = \frac{\bar{\rho}}{\bar{\alpha}}\left(\tilde{b}\frac{\cos(i_1)}{1 - c_\alpha/2} + \tilde{c}\frac{\cos(i_2)}{1 + c_\alpha/2}\right), & F &= \frac{\bar{\rho}}{\hat{V}\bar{\alpha}}\tilde{F} = \frac{\bar{\rho}}{\hat{V}\bar{\alpha}}\left(\tilde{b}\frac{\cos(j_1)}{1 - c_\beta/2} + \tilde{c}\frac{\cos(j_2)}{1 + c_\beta/2}\right), \\ G &= \bar{\rho}\tilde{G} = \bar{\rho}\left(\tilde{a} - \tilde{d}\hat{V}\frac{\cos(i_1)}{1 - c_\alpha/2}\frac{\cos(j_2)}{1 + c_\beta/2}\right), & H &= \bar{\rho}\tilde{H} = \bar{\rho}\left(\tilde{a} - \tilde{d}\hat{V}\frac{\cos(i_2)}{1 + c_\alpha/2}\frac{\cos(j_1)}{1 - c_\beta/2}\right), \\ D &= EF + GHp^2 = \frac{\bar{\rho}^2}{\bar{\alpha}^2}\left(\frac{\tilde{E}\tilde{F}}{\hat{V}} + \tilde{G}\tilde{H}\sin^2(\theta)\right), \end{aligned} \tag{2.7}$$

where we have once again indicated dimensionless variables with the ˜ symbol. Finally, using equations 2.2, 2.4, 2.6 and 2.7, the Zoeppritz PP-reflection coefficient for waves coming from above equals

$$R_{PP}^{\cup}(\sin(\theta), c_\alpha, c_\beta, c_\rho) = \frac{\left(\tilde{b}\frac{\cos(i_1)}{1 - c_\alpha/2} - \tilde{c}\frac{\cos(i_2)}{1 + c_\alpha/2}\right)\frac{\tilde{F}}{\hat{V}} - \left(\tilde{a} + \tilde{d}\hat{V}\frac{\cos(i_1)}{1 - c_\alpha/2}\frac{\cos(j_2)}{1 + c_\beta/2}\right)\tilde{H}\sin^2(\theta)}{\frac{\tilde{E}\tilde{F}}{\hat{V}} + \tilde{G}\tilde{H}\sin^2(\theta)}. \tag{2.8}$$

As expected, $R_{PP}^{\cup}(\sin(\theta), c_\alpha, c_\beta, c_\rho)$ is dimensionless, and only depends on the

dimensionless variables c_α, c_β, c_ρ, $\hat{V}$, as well as the angle $\sin(\theta)$. In a similar way, the expressions for the remaining reflection and transmission coefficients can be found.

The goal of our work is to find accurate approximations of the Zoeppritz reflection and transmission coefficients. To do this, we begin by noting that c_α, c_β, c_ρ and $\sin(\theta)$ all have a magnitude smaller than 1 for normal seismic applications. Therefore, a natural approximation is given by taking the Taylor expansion of equation 2.8 with respect to c_α, c_β, c_ρ and $\sin(\theta)$. For a function of multiple variables, the Taylor expansion is given by

$$R_{PP}^{\cup}\left(\sin(\theta), c_\alpha, c_\beta, c_\rho\right) \approx \sum_{n,m,k,l} \frac{1}{n!m!k!l!} \frac{d^{n+m+k+l} R_{PP}^{\cup}}{d(\sin(\theta))^n dc_\alpha^m dc_\beta^k dc_\rho^l}\bigg|_{(\mathbf{0})} \sin^n(\theta)\, c_\alpha^m c_\beta^k c_\rho^l, \quad (2.9)$$

where the argument $|_{(\mathbf{0})}$ is used as shorthand for $\sin(\theta)=0$, $c_\alpha=0$, $c_\beta=0$ and $c_\rho=0$. As the Zoeppritz equations are well-behaved up to the critical angle $\sin(\theta_c)=\tilde{\alpha}/\max(\alpha_1,\alpha_2)$, we know that the Taylor series of equation 2.9 will converge to R_{PP} for angles $\theta<\theta_c$, given enough terms. For ease of interpretation, we order the terms of equation 2.9 in terms of the power n of the $\sin^n(\theta)$ term and the total power $\lambda=m+k+l$ of the contrast terms c_α^m, c_β^k and c_ρ^l, hence

$$R_{PP}^{\cup}\left(\sin(\theta), c_\alpha, c_\beta, c_\rho\right) \approx \sum_{n=0}^{N}\sum_{\lambda=0}^{\Lambda} \left(\tilde{R}_{PP}^{\cup}\right)_\lambda^n, \quad (2.10)$$

with

$$\left(\tilde{R}_{PP}^{\cup}\right)_\lambda^n = \sum_{m=0}^{\lambda}\sum_{k=0}^{\lambda-m} \frac{1}{n!m!k!(\lambda-k-m)!} \frac{d^{n+\lambda} R_{PP}^{\cup}}{d(\sin(\theta))^n dc_\alpha^m dc_\beta^k dc_\rho^{(\lambda-k-m)}}\bigg|_{(\mathbf{0})} \sin^n(\theta)\, c_\alpha^m c_\beta^k c_\rho^{(\lambda-k-m)}. \quad (2.11)$$

While equation 2.11 is difficult to evaluate by hand, by using mathematical software such as Maple it is straightforward to calculate the necessary terms. The first few terms of equation 2.11 are given by

$$\begin{aligned}
&\left(\tilde{R}_{PP}^{\cup}\right)_1^0 = \frac{1}{2}\left(c_\alpha + c_\rho\right), \quad \left(\tilde{R}_{PP}^{\cup}\right)_2^0 = 0, \quad \left(\tilde{R}_{PP}^{\cup}\right)_3^0 = -\frac{1}{8} c_\alpha c_\rho \left(c_\alpha + c_\rho\right),\\
&\left(\tilde{R}_{PP}^{\cup}\right)_1^2 = \left(\frac{1}{2}c_\alpha - 2\hat{V}^2\left(c_\rho + 2c_\beta\right)\right)\sin^2(\theta), \quad \left(\tilde{R}_{PP}^{\cup}\right)_2^2 = \left(\hat{V}^3\left(c_\rho + 2c_\beta\right)^2 - \frac{1}{4}\hat{V} c_\rho^2\right)\sin^2(\theta),\\
&\left(\tilde{R}_{PP}^{\cup}\right)_1^4 = \frac{1}{2} c_\alpha \sin^4(\theta), \quad \ldots
\end{aligned} \quad (2.12)$$

Also note that $\left(\tilde{R}_{PP}^{\cup}\right)_\lambda^n = 0$ for odd values of n, as we know that $R_{PP}^{\cup}$ is an even function with respect to θ (meaning that it contains no $\sin^n(\theta)$ terms for odd values of n).

Let us now examine the terms of equation 2.11 in more detail. We begin by writing the two-term Shuey approximation, which, using the notation used in this paper, is

denoted as

$$R_{PP}^{\cup}\left(\sin\left(\theta\right),c_{\alpha},c_{\beta},c_{\rho}\right)\approx\frac{1}{2}\left(c_{\alpha}+c_{\rho}\right)+\left(\frac{1}{2}c_{\alpha}-2\hat{V}^{2}\left(c_{\rho}+2c_{\beta}\right)\right)\sin^{2}\left(\theta\right). \tag{2.13}$$

However, this is exactly equal to the approximation given by taking $N=2$ and $\Lambda=1$ in equation 2.10. Continuing in this manner, we examine the three-term Shuey approximation, which can be written as

$$R_{PP}^{\cup}\left(\sin\left(\theta\right),c_{\alpha},c_{\beta},c_{\rho}\right)\approx\frac{1}{2}\left(c_{\alpha}+c_{\rho}\right)+\left(\frac{1}{2}c_{\alpha}-2\hat{V}^{2}\left(c_{\rho}+2c_{\beta}\right)\right)\sin^{2}\left(\theta\right)+\frac{1}{2}c_{\alpha}\left(\tan^{2}\left(\theta\right)-\sin^{2}\left(\theta\right)\right). \tag{2.14}$$

We note that the Taylor expansion of $\tan^{2}\left(\theta\right)-\sin^{2}\left(\theta\right)$ is given by

$$\tan^{2}\left(\theta\right)-\sin^{2}\left(\theta\right)\approx\sin^{4}\left(\theta\right)+\sin^{6}\left(\theta\right)+\sin^{8}\left(\theta\right)+\ldots, \tag{2.15}$$

which, once again, matches the approximation given in equation 2.10 for $N=8$ and $\Lambda=1$. Therefore, we conclude that the approximation presented here can be viewed as an extension to Shuey's approximation.

In a similar way, we can construct approximations to the rest of the Zoeppritz equations. For example, the SP-reflection coefficient $R_{SP}^{\cup}$, which describes the conversion of P-waves to S-waves for waves coming from above, is given by

$$R_{SP}^{\cup}=-2\frac{\left(\tilde{a}\tilde{b}+\tilde{c}\tilde{d}\hat{V}\dfrac{\cos\left(i_{2}\right)}{1+c_{\alpha}/2}\dfrac{\cos\left(j_{2}\right)}{1+c_{\beta}/2}\right)\cos\left(i_{1}\right)\sin\left(\theta\right)}{\left(1-c_{\beta}/2\right)\left(\tilde{E}\tilde{F}+\tilde{G}\tilde{H}\hat{V}\sin^{2}\left(\theta\right)\right)}. \tag{2.16}$$

Once again, we take the Taylor expansion

$$R_{SP}^{\cup}\left(\sin\left(\theta\right),c_{\alpha},c_{\beta},c_{\rho}\right)\approx\sum_{n,\lambda}\left(\tilde{R}_{SP}^{\cup}\right)_{\lambda}^{n}, \tag{2.17}$$

with

$$\left(\tilde{R}_{SP}^{\cup}\right)_{\lambda}^{n}=\sum_{m=0}^{\lambda}\sum_{k=0}^{\lambda-m}\frac{1}{n!m!k!\left(\lambda-k-m\right)!}\left.\frac{d^{n+\lambda}R_{SP}^{\cup}}{d\left(\sin\left(\theta\right)\right)^{n}dc_{\alpha}^{m}dc_{\beta}^{k}dc_{\rho}^{\left(\lambda-k-m\right)}}\right|_{\left(\mathbf{0}\right)}\sin^{n}\left(\theta\right)c_{\alpha}^{m}c_{\beta}^{k}c_{\rho}^{\left(\lambda-k-m\right)}. \tag{2.18}$$

The first few terms of equation 2.18 are given by

$$\begin{aligned}\left(\tilde{R}_{SP}^{\cup}\right)_{1}^{1}&=-\left(\hat{V}\left(c_{\rho}+2c_{\beta}\right)+\frac{1}{2}c_{\rho}\right)\sin\left(\theta\right),\\ \left(\tilde{R}_{SP}^{\cup}\right)_{2}^{1}&=\left(\frac{1}{4}\left(2\hat{V}-1\right)c_{\rho}^{2}+\frac{1}{4}c_{\rho}\left(\hat{V}\left(4c_{\beta}+2c_{\alpha}\right)-c_{\beta}\right)+\hat{V}c_{\alpha}c_{\beta}\right)\sin\left(\theta\right),\\ \left(\tilde{R}_{SP}^{\cup}\right)_{1}^{3}&=\frac{1}{4}\left(\hat{V}^{2}\left(8c_{\beta}+3c_{\rho}\right)+\hat{V}\left(2c_{\rho}+4c_{\beta}\right)\right)\sin^{3}\left(\theta\right).\end{aligned} \tag{2.19}$$

In a similar way as before for the $R_{PP}^{\cup}$ terms, we note that $\left(\tilde{R}_{SP}^{\cup}\right)_{\lambda}^{n}=0$ for even values of n, as we know that $R_{SP}^{\cup}$ is an odd function with respect to θ.

A thorough analysis of the quality of these extended Shuey approximations are given in sections 2.3.1 and 2.4. In section 2.3.1 we examine how many terms of the Taylor expansion are required to produce an accurate approximation. In section 2.4 we compare the approximation introduced here with well-known approximations from literature, such as the standard Shuey's approximation and the linearized approximation of [3].

2.2.2. ELASTIC FULL WAVEFIELD MODELLING

We now apply these extended Shuey approximations, described in section 2.2.1, to the elastic Full-Wavefield Modelling (FWMod) algorithm [8]. For simplicity's sake we consider a 1.5D medium: a laterally homogeneous, but potentially vertically changing medium, characterised by a P- and S-wave velocity profile $\alpha(z)$ and $\beta(z)$, respectively, and a mass density profile $\rho(z)$. As the medium is laterally homogeneous, we will work in the (k_x,ω)-domain, where k_x is the lateral wave number and ω is the angular frequency. Our goal is to describe the propagation and scattering of the P- and S-wavefields $p_P(k_x,\omega,z)$ and $p_S(k_x,\omega,z)$, respectively.

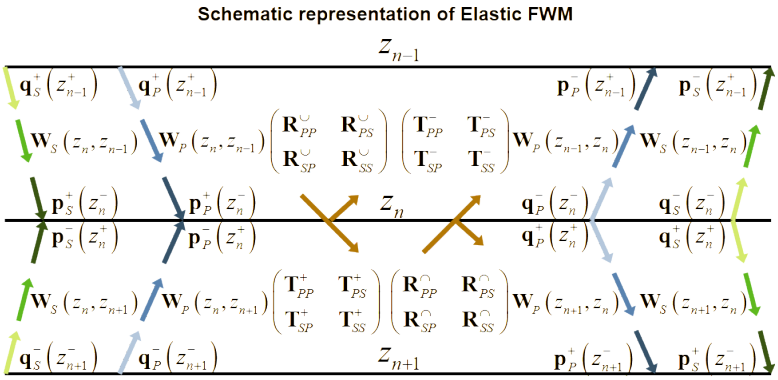

Figure 2.1: Schematic representation of the wavefields and operators at depth level z_n and its neighbouring levels.

Assume the existence of an interface at a depth level z_n, illustrated in figure 2.1. At a depth level z_n^- right above the interface, the P- and S-wavefields are given by

$$p_{P/S}(k_x,\omega,z_n^-) = p_{P/S}^+(k_x,\omega,z_n^-) + q_{P/S}^-(k_x,\omega,z_n^-), \tag{2.20}$$

where we have split the P- and S-wavefields $p_{P/S}(k_x,\omega,z_n^-)$ into downgoing components, $p_{P/S}^+(k_x,\omega,z_n^-)$, travelling towards the interface, and upgoing components, $q_{P/S}^-(k_x,\omega,z_n^-)$, travelling away from the interface. Similarly, at a depth level z_n^+ right below the interface, the $P-$ and $S-$wavefields are given by

$$p_{P/S}(k_x,\omega,z_n^+) = q_{P/S}^+(k_x,\omega,z_n^+) + p_{P/S}^-(k_x,\omega,z_n^+), \tag{2.21}$$

where we have once again split the P- and S-wavefields into upgoing components,

$p^-_{P/S}(k_x,\omega,z_n^+)$, travelling towards the interface, and downgoing components, $q^+_{P/S}(k_x,\omega,z_n^+)$, travelling away from the interface. Note the notation used here. Superscripts above the field quantities p and q are used to indicate the direction of propagation, where + and − denote downwards and upwards propagation, respectively. The characters p and q are used to denote wavefields propagating towards or away from the interface, respectively. Finally, the subscripts P and S are used to differentiate between P- and S-wavefields, respectively.

At the interface at $z = z_n$, the relationships between these wavefields are given by

$$\begin{pmatrix} q_P^+ \\ q_S^+ \end{pmatrix} = \begin{pmatrix} R^{\cap}_{PP} & R^{\cap}_{PS} \\ R^{\cap}_{SP} & R^{\cap}_{SS} \end{pmatrix} \begin{pmatrix} p_P^- \\ p_S^- \end{pmatrix} + \begin{pmatrix} T^+_{PP} & T^+_{PS} \\ T^+_{SP} & T^+_{SS} \end{pmatrix} \begin{pmatrix} p_P^+ \\ p_S^+ \end{pmatrix}, \tag{2.22}$$

$$\begin{pmatrix} q_P^- \\ q_S^- \end{pmatrix} = \begin{pmatrix} R^{\cup}_{PP} & R^{\cup}_{PS} \\ R^{\cup}_{SP} & R^{\cup}_{SS} \end{pmatrix} \begin{pmatrix} p_P^+ \\ p_S^+ \end{pmatrix} + \begin{pmatrix} T^-_{PP} & T^-_{PS} \\ T^-_{SP} & T^-_{SS} \end{pmatrix} \begin{pmatrix} p_P^- \\ p_S^- \end{pmatrix}, \tag{2.23}$$

where, for ease of legibility, we have omitted the dependency on (k_x,ω), as well as the dependency on the depth level z_n. For similar reasons, we also introduce the following shorthand notation for equations 2.22 and 2.23, viz

$$\mathbf{q}^+(z_n) = \mathbf{R}^{\cap}(z_n)\,\mathbf{p}^-(z_n) + \mathbf{T}^+(z_n)\,\mathbf{p}^+(z_n), \tag{2.24}$$

$$\mathbf{q}^-(z_n) = \mathbf{R}^{\cup}(z_n)\,\mathbf{p}^+(z_n) + \mathbf{T}^-(z_n)\,\mathbf{p}^-(z_n), \tag{2.25}$$

which we will use throughout the rest of this paper.

In equations 2.22 and 2.23 the terms $R^{\cup}_{\cdots}$ and $T^+_{\cdots}$ represent the reflection and transmission coefficients for waves coming from above, respectively, while the terms $R^{\cap}_{\cdots}$ and $T^-_{\cdots}$ represent the reflection and transmission coefficients for waves coming from below. In principle, it is possible to use the true Zoeppritz reflection and transmission coefficients for these terms. We will, however, use the extended Shuey approximations detailed in section 2.2.1 instead, to simplify the inverse problem described in section 2.2.3. Applying the extended Shuey approximations to $R^{\cup}_{PP}$, for example, we write

$$R^{\cup}_{PP}(k_x,\omega,z_n) \approx \sum_{n=0}^{N}\sum_{\lambda=0}^{\Lambda}\left(\tilde{R}^{\cup}_{PP}(z_n)\right)^n_{\lambda}\left(\frac{\tilde{\alpha}(z_n)\,k_x}{\omega}\right)^n, \tag{2.26}$$

where we have used the relationship

$$k_x = \frac{\omega \sin(\theta(z_n))}{\tilde{\alpha}(z_n)}. \tag{2.27}$$

In a similar way, we can write the approximations to the other reflection and transmission coefficients.

Next, we write the relationship between wavefields at different depth levels, viz.

$$\begin{pmatrix} p_P^+(z_{n+1}) \\ p_S^+(z_{n+1}) \end{pmatrix} = \begin{pmatrix} W_P(z_{n+1},z_n) & 0 \\ 0 & W_S(z_{n+1},z_n) \end{pmatrix} \begin{pmatrix} q_P^+(z_n) \\ q_S^+(z_n) \end{pmatrix}, \tag{2.28}$$

$$\begin{pmatrix} p_P^-(z_{n-1}) \\ p_S^-(z_{n-1}) \end{pmatrix} = \begin{pmatrix} W_P(z_{n-1}, z_n) & 0 \\ 0 & W_S(z_{n-1}, z_n) \end{pmatrix} \begin{pmatrix} q_P^-(z_n) \\ q_S^-(z_n) \end{pmatrix}, \tag{2.29}$$

where we have introduced the propagation operators W_P and W_S for P- and S-wavefields, respectively. These operators are given by

$$\begin{aligned} W_P(z_{n+1}, z_n) &= \exp\left[-i\Delta z\sqrt{\left(\frac{\omega}{\alpha(z_n^+)}\right)^2 - k_x^2}\right], \quad W_S(z_{n+1}, z_n) = \exp\left[-i\Delta z\sqrt{\left(\frac{\omega}{\beta(z_n^+)}\right)^2 - k_x^2}\right], \\ W_P(z_{n-1}, z_n) &= \exp\left[-i\Delta z\sqrt{\left(\frac{\omega}{\alpha(z_n^-)}\right)^2 - k_x^2}\right], \quad W_S(z_{n-1}, z_n) = \exp\left[-i\Delta z\sqrt{\left(\frac{\omega}{\beta(z_n^-)}\right)^2 - k_x^2}\right], \end{aligned} \tag{2.30}$$

where Δz is the distance between neighbouring depth levels. Note that the quantity $\sqrt{(\omega/\alpha(z_n^-))^2 - k_x^2}$ may become imaginary for certain values of ω, $\alpha(z_n^-)$ and k_x. To avoid problems during modelling and inversion, we make the following substitution

$$\sqrt{(\omega/\alpha(z_n^-))^2 - k_x^2} \rightarrow Re\left[\sqrt{(\omega/\alpha(z_n^-))^2 - k_x^2}\right] - i\left|Im\left[\sqrt{(\omega/\alpha(z_n^-))^2 - k_x^2}\right]\right| \tag{2.31}$$

in practice. Finally, we once again introduce shorthand notations for equations 2.28 and 2.29, viz.

$$\mathbf{p}^+(z_{n+1}) = \mathbf{W}(z_{n+1}, z_n)\,\mathbf{q}^+(z_n), \tag{2.32}$$

$$\mathbf{p}^-(z_{n-1}) = \mathbf{W}(z_{n-1}, z_n)\,\mathbf{q}^-(z_n). \tag{2.33}$$

With the building blocks of equations 2.24, 2.25, 2.32 and 2.33 in place, we now examine the forward modelling algorithm. To initialize the algorithm, we set all upgoing and downgoing wavefields to zero, i.e. $\mathbf{p}^{-,0}(z_n) = \mathbf{p}^{+,0}(z_n) = \mathbf{0}$. Note the notation of $\mathbf{p}^{-,0}$ and $\mathbf{p}^{+,0}$, where we have introduced an extra number in the superscript, which denotes how many so-called 'round-trips' have been modelled. Each round-trip increases the maximum order of multiples which are taken into account by one, up to the chosen number of round-trips to be modelled. Furthermore, for simplicity's sake, we assume that there are no sources within the subsurface, only at the surface. In that case, we set $\mathbf{p}^{+,m}(z_0) = \mathbf{s}_0$ for all m round-trips, where $\mathbf{s}_0$ is a vector containing the source wavefield for one shot at $z = z_0$. Finally, we assume that there are no upgoing waves coming from below the deepest depth level $z_n = z_{N_z}$. Therefore, we write $\mathbf{p}^{-,m}(z_{N_z}) = \mathbf{0}$ for all m round-trips.

We then begin by computing the downgoing wavefields for the first round-trip. Starting at $z_n = z_0$, we use equation 2.24 to write $\mathbf{q}^{+,1}(z_0) = \mathbf{T}^+(z_0)\,\mathbf{p}^{+,1}(z_0) + \mathbf{R}^\cap(z_0)\,\mathbf{p}^{-,0}(z_0)$. Next, we apply the propagation operators, using equation 2.32 to write $\mathbf{p}^{+,1}(z_1) = \mathbf{W}(z_1, z_0)\,\mathbf{q}^{+,1}(z_0)$. At the depth level $z_n = z_1$ we simply repeat this process with the appropriate transmission, reflection and propagation operators. In this way, we model the downgoing wavefield $\mathbf{p}^{+,1}(z_n)$ at all depth levels.

Next, we compute the upgoing wavefield $\mathbf{p}^{-,1}(z_n)$ at all depth levels. We start at the deepest depth level $z_n = z_{N_z}$. We then use equation 2.25 to write $\mathbf{q}^{-,1}(z_{N_z}) = \mathbf{T}^-(z_{N_z})\,\mathbf{p}^{-,1}(z_{N_z}) + \mathbf{R}^\cup(z_{N_z})\,\mathbf{p}^{+,1}(z_{N_z})$ and apply the propagation operators of equation 2.33 to write $\mathbf{p}^{-,1}(z_{N_z-1}) = \mathbf{W}(z_{N_z-1}, z_{N_z})\,\mathbf{q}^{-,1}(z_{N_z})$. Once again, we

Algorithm 1: Elastic Full-Wavefield Modelling (FWMod)

Result: $\mathbf{p}^{+,M}(z_n)$ and $\mathbf{p}^{-,M}(z_n)$ for all z_n.
Input: $\mathbf{s}_0$
Set $\mathbf{p}^{-,0}(z_n) = \mathbf{0}$;
for $m = 1 : M$ **do**
  Set $\mathbf{p}^{+,m}(z_0) = \mathbf{s}_0$;
  for $n = 0 : N_z - 1$ **do**
    $\mathbf{q}^{+,m}(z_n) = \mathbf{T}^{+}(z_n)\,\mathbf{p}^{+,m}(z_n) + \mathbf{R}^{\cap}(z_n)\,\mathbf{p}^{-,m-1}(z_n)$;
    $\mathbf{p}^{+,m}(z_{n+1}) = \mathbf{W}(z_{n+1}, z_n)\,\mathbf{q}^{+,m}(z_n)$;
  end
  Set $\mathbf{p}^{-,m}(z_{N_z}) = \mathbf{0}$;
  for $n = N_z : -1 : 2$ **do**
    $\mathbf{q}^{-,m}(z_n) = \mathbf{T}^{-}(z_n)\,\mathbf{p}^{-,m}(z_n) + \mathbf{R}^{\cup}(z_n)\,\mathbf{p}^{+,m}(z_n)$;
    $\mathbf{p}^{-,m}(z_{n-1}) = \mathbf{W}(z_{n-1}, z_n)\,\mathbf{q}^{-,m}(z_n)$;
  end
end

continue to apply these operators to find the upgoing wavefield $\mathbf{p}^{-,1}(z_n)$ at each depth level.

We now repeat this process as many times as we wish to account for higher-order scattering, where the scattering order is increased by one after each round-trip. The full process for finding the wavefields $\mathbf{p}^{+,M}(z_n)$ and $\mathbf{p}^{-,M}(z_n)$ for up to M scattering orders is illustrated in algorithm 1.

2.2.3. ELASTIC FULL WAVEFIELD MIGRATION

Next, we examine the elastic FWM algorithm [9], which is the inversion process associated with the elastic FWMod algorithm described in section 2.2.2. As in section 2.2.2, we limit our analysis to the 1.5D case.

Consider a situation with known, P- and S-wave measurement data $\mathbf{d}(k_x, \omega)$ at the surface. We also assume the source wavefield $\mathbf{s}_0$ and the propagation operators $\mathbf{W}(z_{n+1}, z_n)$ and $\mathbf{W}(z_{n-1}, z_n)$ to be known. Our goal is to recover the contrast parameters $c_\alpha(z_n)$, $c_\beta(z_n)$ and $c_\rho(z_n)$ at all depth levels z_n.

To achieve this, we first define a cost function J, which measures the mismatch between the measured data $\mathbf{d}(k_x, \omega)$ and the forward modelled data at the surface after M roundtrips, $\mathbf{p}^{-,M}(k_x, \omega, z_0)$, viz.

$$J = \frac{1}{2} \sum_{k_x} \sum_{\omega} \left| \mathbf{d}(k_x, \omega) - \mathbf{p}^{-,M}(k_x, \omega, z_0) \right|^2. \tag{2.34}$$

To retrieve the contrast parameters, we now apply a gradient-descent algorithm with respect to these parameters to minimize J. Taking the gradient of the cost function

Algorithm 2: Elastic Full-Wavefield Migration (FWM)

Result: $c_\alpha(z_n)$, $c_\beta(z_n)$ and $c_\rho(z_n)$ for all z_n.
Input: $\mathbf{d}$, $\mathbf{s}_0$, $\mathbf{W}(z_{n+1}, z_n)$ and $\mathbf{W}(z_{n-1}, z_n)$ for all z_n.

for $m = 1 : M$ **do**
  Use algorithm 1 to calculate $\mathbf{p}^{+,M}(z_n)$ and $\mathbf{p}^{-,M}(z_0)$;
  for $n = 1 : N_z$ **do**
    for $c \in c_\alpha, c_\beta, c_\rho$ **do**
      Construct the matrices $\partial\mathbf{R}^{\cup}_{c(z_n)}$, $\partial\mathbf{R}^{\cap}_{c(z_n)}$, $\partial\mathbf{T}^{+}_{c(z_n)}$ and $\partial\mathbf{T}^{-}_{c(z_n)}$;
      Calculate the gradient $\dfrac{\partial J}{\partial c(z_n)}$;
    end
  end
  Calculate the wavefield perturbation $\Delta\mathbf{p}^{-,M}(z_0)$;
  Calculate γ;
  for $c \in c_\alpha, c_\beta, c_\rho$ **do**
    Update the contrasts using $c_{\text{new}}(z_n) = c_{\text{old}}(z_n) + \gamma \dfrac{\partial J}{\partial c(z_n)}$;
  end
end

with respect to the contrast parameter c_α at depth level z_n, for example, yields

$$\frac{\partial J}{\partial c_\alpha(z_n)} = -\sum_{k_x}\sum_{\omega} \text{Re}\left[\frac{\partial \mathbf{p}^{-,M}(k_x,\omega,z_0)}{\partial c_\alpha(z_n)}^{\mathbf{H}} \mathbf{e}(k_x,\omega)\right], \tag{2.35}$$

where $\mathbf{e}(k_x,\omega) = \mathbf{d}(k_x,\omega) - \mathbf{p}^{-,M}(k_x,\omega,z_0)$.

We now examine the derivative of $\mathbf{p}^{-,M}(k_x,\omega,z_0)$ with respect to $c_\alpha(z_n)$. To evaluate this, we first examine the contribution of a scatterer located at the depth level $z = z_n$ to the forward modelled wavefield $\mathbf{p}^{-,M}(k_x,\omega,z_0)$, viz

$$\begin{aligned}\mathbf{p}^{-,M}(z_0;z_n) = \quad & \bar{\mathbf{W}}^{-}(z_0,z_n)\left[\mathbf{R}^{\cup}(z_n)\mathbf{p}^{+,M}(z_n) + \mathbf{T}^{-}(z_n)\mathbf{p}^{-,M}(z_n)\right] + \\ & \bar{\mathbf{W}}^{\cup}(z_0,z_n)\left[\mathbf{R}^{\cap}(z_n)\mathbf{p}^{-,M}(z_n) + \mathbf{T}^{+}(z_n)\mathbf{p}^{+,M}(z_n)\right],\end{aligned} \tag{2.36}$$

where we have assumed $\mathbf{p}^{-,M-1}(z_n) \approx \mathbf{p}^{-,M}(z_n)$. In equation 2.36 we have also introduced the generalized propagation operators $\bar{\mathbf{W}}^{-}(z_0,z_n)$ and $\bar{\mathbf{W}}^{\cup}(z_0,z_n)$. These operators are constructed by applying sequences of propagation, reflection and transmission operators and are defined as

$$\bar{\mathbf{W}}^{-}(z_j,z_i) = \prod_{m=i-1}^{j+1}[\mathbf{W}(z_{m-1},z_m)\mathbf{T}^{-}(z_m)]\mathbf{W}(z_{i-1},z_i) \;\; \forall\, j < i, \tag{2.37}$$

$$\bar{\mathbf{W}}^{+}(z_j,z_i) = \prod_{m=i+1}^{j-1}[\mathbf{W}(z_{m+1},z_m)\mathbf{T}^{-}(z_m)]\mathbf{W}(z_{i+1},z_i) \;\; \forall\, j > i, \tag{2.38}$$

$$\bar{\mathbf{W}}^{\cup}(z_0, z_n) = \sum_{m=n+1}^{N_z} \bar{\mathbf{W}}^{-}(z_0, z_m)\,\mathbf{R}^{\cup}(z_m)\,\bar{\mathbf{W}}^{+}(z_m, z_n). \tag{2.39}$$

If we assume that the contrast parameters are independent at each depth level, we can write

$$\frac{\partial \mathbf{p}^{-,M}(k_x, \omega, z_0)}{\partial c_\alpha(z_n)} = \frac{\partial \mathbf{p}^{-,M}(z_0; z_n)}{\partial c_\alpha(z_n)}, \tag{2.40}$$

with

$$\begin{aligned}\frac{\partial \mathbf{p}^{-,M}(z_0; z_n)}{\partial c_\alpha(z_n)} = \quad & \bar{\mathbf{W}}^{-}(z_0, z_n)\left[\partial \mathbf{R}^{\cup}_{c_\alpha(z_n)}(z_n)\,\mathbf{p}^{+,M}(z_n) + \partial \mathbf{T}^{-}_{c_\alpha(z_n)}(z_n)\,\mathbf{p}^{-,M}(z_n)\right] + \\ & \bar{\mathbf{W}}^{\cup}(z_0, z_n)\left[\partial \mathbf{R}^{\cap}_{c_\alpha(z_n)}(z_n)\,\mathbf{p}^{-,M}(z_n) + \partial \mathbf{T}^{+}_{c_\alpha(z_n)}(z_n)\,\mathbf{p}^{+,M}(z_n)\right],\end{aligned} \tag{2.41}$$

where $\partial \mathbf{R}^{\cup}_{c_\alpha(z_n)}$, $\partial \mathbf{R}^{\cap}_{c_\alpha(z_n)}$, $\partial \mathbf{T}^{+}_{c_\alpha(z_n)}$ and $\partial \mathbf{T}^{-}_{c_\alpha(z_n)}$ are 2×2 matrices. These matrices are constructed by calculating the derivatives of the approximate reflection and transmission coefficients introduced in section 2.2.1. For example, the PP-component of the matrix $\partial \mathbf{R}^{\cup}_{c_\alpha(z_n)}$ is given by

$$\partial \mathbf{R}^{\cup}_{c_\alpha(z_n)}(z_n)\Big|_{11} = \frac{\partial R^{\cup}_{PP}(k_x, \omega, z_n)}{\partial c_\alpha(z_n)} = \sum_{n=0}^{N}\sum_{\lambda=0}^{\Lambda} \frac{\partial \left(\tilde{R}^{\cup}_{PP}(z_n)\right)^n_\lambda}{\partial c_\alpha(z_n)} \left(\frac{\bar{\alpha}(z_n)\,k_x}{\omega}\right)^n, \tag{2.42}$$

with similar definitions for the other components. Using equations 2.41 and 2.42 we can now evaluate equation 2.35 for all depth levels z_n.

In a similar fashion, we can calculate the gradients with respect to $c_\beta(z_n)$ and $c_\rho(z_n)$. Using the full gradient, we calculate the linearized wavefield perturbation at the surface, viz.

$$\Delta \mathbf{p}^{-,M}(z_0) = \sum_n \sum_{c \in c_\alpha, c_\beta, c_\rho} \frac{\partial J}{\partial c(z_n)} \frac{\partial \mathbf{p}^{-,M}(z_0; z_n)}{\partial c(z_n)}. \tag{2.43}$$

Finally, using equation 2.43, we calculate the update to the contrast parameters using

$$c_{\text{new}}(z_n) = c_{\text{old}}(z_n) + \gamma \frac{\partial J}{\partial c(z_n)}, \tag{2.44}$$

for $c \in c_\alpha, c_\beta, c_\rho$, where the (real) constant γ is given by

$$\gamma = \frac{\sum_{k_x}\sum_{\omega} \mathrm{Re}\left[\Delta \mathbf{p}^{-,M}(k_x, \omega, z_0)^{\mathbf{H}} \mathbf{e}(k_x, \omega)\right]}{\sum_{k_x}\sum_{\omega} \left|\Delta \mathbf{p}^{-,M}(k_x, \omega, z_0)\right|^2}. \tag{2.45}$$

Repeating the process described above for as many iterations as desired, one can retrieve the contrast parameters $c_\alpha(z_n)$, $c_\beta(z_n)$ and $c_\rho(z_n)$ at all depth levels z_n. This process is summarized in algorithm 2

2.3. NUMERICAL RESULTS

This section is, once again, split into three parts. First, in section 2.3.1, we examine how many terms of the extended Shuey's approximation introduced in section 2.2.1 are required to accurately approximate the Zoeppritz equations. Next, in section 2.3.2, we compare the forward modelled wavefields using the FWMod algorithm of 2.2.2 to true, synthetic, data generated using an elastic Kennett algorithm. Finally, in section 2.3.3, we examine the inversion results of the elastic FWM algorithm of section 2.2.3.

2.3.1. EXTENDED SHUEY'S APPROXIMATIONS

We begin by examining the quality of the approximation of equation 2.26 of section 2.2.1. Specifically, we are interested in how many terms $n \leq N$ and $\lambda \leq \Lambda$ of the Taylor expansion are required for a good approximation. The Taylor expansions of $R^{\cup}_{PP}$ and $R^{\cup}_{SP}$ for different values of N and Λ for both a low- and a high-contrast interface are shown in figure 2.2. The associated medium parameters used for the low- and high-contrast interface are displayed in table 2.1.

From the results of figure 2.2 we can draw a number of conclusions. First of all, we see that increasing N and Λ improves the approximation up to the critical angle, as we would expect. If the contrasts at the interface are low, we see that the quality of the approximation is mostly determined by the number of $\sin^n(\theta)$ terms N taken into account. By contrast, if the contrasts are high, we see that the quality is mostly determined by the number of contrast terms Λ taken into account.

In general, we conclude that, in order to obtain a high-quality approximation, one should choose a value of $N > 2$, as well as a value of $\Lambda > 1$, at the very least, especially for interfaces with high contrasts. In this case, the extended Shuey's approximation yields reasonable results for both $R^{\cup}_{PP}$ and $R^{\cup}_{SP}$. Note that, while figure 2.2 only shows the results for $R^{\cup}_{PP}$ and $R^{\cup}_{SP}$, a similar analysis has been performed for the other reflection and transmission coefficients. These results can be found in the appendix.

2.3.2. ELASTIC FWMOD

Next, we examine the results of the elastic FWMod algorithm, as described in section 2.2.2. To benchmark the method, we compare the results to synthetic data generated using an elastic Kennett algorithm [10], which takes the full, Zoeppritz, reflection and transmission coefficients into account. The medium parameters used are equivalent to the high-contrast scenario described in table 2.1. Note that, as we know that the approximation presented in section 2.2.1 only holds up to the critical angle θ_c, data corresponding to angles $\theta > 0.8 \cdot \theta_c$ have been removed from the data.

In figures 2.3 and 2.4 we have displayed the difference between the forward modelled data and the true, synthetic, data at the surface for P- and S-waves, respectively. From these figures, we see similar behaviour as in figure 2.2. The difference between the true data at the surface and the forward modelled data decreases as N and Λ increase. Once again, we see that high-quality results are only achieved for $N > 2$ and $\Lambda > 1$.

Table 2.1: Parameters figure 2.2

Low contrast		**High contrast**	
$\alpha_1 = 1500$ m/s	$\alpha_2 = 1800$ m/s	$\alpha_1 = 1500$ m/s	$\alpha_2 = 3000$ m/s
$\beta_1 = 750$ m/s	$\beta_2 = 1000$ m/s	$\beta_1 = 750$ m/s	$\beta_2 = 1600$ m/s
$\rho_1 = 1000$ m/s	$\rho_2 = 1400$ m/s	$\rho_1 = 1000$ m/s	$\rho_2 = 1700$ m/s

This conclusion is supported by the plots of the cost function J, seen in the top-right corner of figures 2.3 and 2.4. In these plots we see that the cost function sharply decreases up to $N = 4$, after which it remains more or less constant. Also, we see a considerable improvement when comparing the curves for $\Lambda = 1$ (blue lines) to the curves for $\Lambda = 2$ (red lines).

2.3.3. ELASTIC FWM

Finally, we examine the results of the FWM algorithm using the extended Shuey approximations, as described in section 2.2.3. We apply the FWM algorithm to synthetic data, generated using the same elastic Kennett algorithm as we used in section 2.3.2 for the high-contrast case of table 2.1. The results of this process are shown in figure 2.5.

From this figure, we initially conclude that the FWM algorithm recovers the contrasts to a reasonable accuracy, irrespective of the value of N and Λ chosen. Looking closer, however, we notice that increasing the value of N to at least $N = 4$ improves the result somewhat. From the figures of the contrasts, we see a slightly improved recovery of the ground truth for $N = 4$ compared to $N = 2$. Also, examining the cost function (displayed in the top-right corner of figure 2.5), we see that the cost function still decreases between $N = 2$ and $N = 4$.

Also note the case $N = 0, \Lambda = 1$, displayed as blue lines in the plots on the left-hand side of figure 2.5. This case is of special interest, as it represents the result of applying conventional, angle-independent, acoustic FWM to the data. Note that, in this case, the contrasts c_α and c_ρ are impossible to separate. This can be seen in figure 2.5, where the results for c_α and c_ρ are identical for the acoustic result. Also, we see that c_β cannot be recovered in this case. These effects may lead to artefacts, which can be seen in the area between the two reflectors, as well as the area below the lowest reflector. While some artefacts are also visible for the other cases, they are reduced compared to the acoustic result.

Finally, we note that, in this case, taking $\Lambda > 1$ does not appear to improve the results significantly. This is most likely due to the fact that, due to the band-limitation of the source wavefield, it is impossible to recover the sharp interfaces present in the medium. Instead, a spread-out, band-limited approximation of the contrasts is recovered. As this reduces the value of the contrasts, higher-order powers of the contrasts do not noticeably impact the result. In cases where this band-limitation is compensated for, however, taking $\Lambda > 1$ will improve the results.

2.4. DISCUSSION

In this section, we compare the extended Shuey's approximations derived in this paper to two existing sets of approximations in literature. The first set of approximations we consider are the two- and three-term Shuey approximations, given by

$$R^{\cup}_{PP,Shuey2} \approx \frac{1}{2}\left(c_\alpha + c_\rho\right) + \left(\frac{1}{2}c_\alpha - 2\hat{V}^2\left(c_\rho + 2c_\beta\right)\right)\sin^2(\theta), \tag{2.46}$$

$$R^{\cup}_{PP,Shuey3} \approx \frac{1}{2}\left(c_\alpha + c_\rho\right) + \left(\frac{1}{2}c_\alpha - 2\hat{V}^2\left(c_\rho + 2c_\beta\right)\right)\sin^2(\theta) + \frac{1}{2}c_\alpha\left(\tan^2(\theta) - \sin^2(\theta)\right). \tag{2.47}$$

Secondly, we also consider the linearized approximations of Aki and Richards [3], which are given by

$$R^{\cup}_{PP,Aki} \approx \frac{1}{2}\left(1 - 4\hat{V}^2\sin^2(\theta)\right)c_\rho + \frac{1}{2\cos^2(i)}c_\alpha - 4\hat{V}^2\sin^2(\theta)\,c_\beta, \tag{2.48}$$

$$R^{\cup}_{SP,Aki} \approx -\frac{\sin(\theta)}{2\cos(j)}\left[c_\rho - 2\left(\hat{V}^2\sin^2(\theta) - \hat{V}\cos(i)\cos(j)\right)\left(c_\rho + 2c_\beta\right)\right], \tag{2.49}$$

where we have introduced the average P-wave angle $i = (i_1 + i_2)/2$ and the average S-wave angle $j = (j_1 + j_2)/2$, following the notation of section 2.2.1.

The reflection coefficients for the approximations under consideration at different angles are shown in figure 2.6. From this figure, we can draw a number of conclusions. First of all, we notice that for high contrasts, both the 2- and 3-term Shuey's approximations, shown in blue, as well as the linearized Aki-Richards approximations, shown in red, fail for angles up to the critical angle. In this case, one requires non-linear terms with respect to the contrasts to properly approximate the reflection coefficients, which are absent in these approximations. This can be seen most clearly in the bottom right figure of figure 2.6, where we see that one requires third-order terms with respect to the contrasts to accurately approximate the reflection coefficient up to the critical angle.

Secondly, we see that the standard, 2-term Shuey approximation (solid blue line), as well as the equivalent approximation for $R^{\cup}_{SP}$ using $N = 1, \Lambda = 1$, only holds for small contrasts and angles far from the critical angle. While this behaviour is expected, one should note the very small range of angles for which this approximation holds, especially for the $R^{\cup}_{SP}$ term. This limits the applicability of this approximation for forward and inverse modelling, where good performance of the approximation over a range of angles is required.

Finally, we note that the linearised Aki-Richards approximation (solid red line) performs very well for low-contrast scenarios, showing a very good approximation for all angles. This is due to the $1/\cos^2(i)$ and $1/\cos(j)$ terms in equations 2.48 and 2.49. While these terms lead to a high-quality approximation, they also introduce critical points in the approximations, making them difficult to invert for directly. The extended Shuey's approximations of this paper avoid this problem, while showing similar behaviour up to the cutoff angle θ_c for $N \geq 4$ and $\Lambda \geq 2$.

2.5. CONCLUSION

In this paper, we present an alternative set of approximations to the Zoeppritz equations for the elastic reflection and transmission coefficients, which we call the extended Shuey approximations. We show that these approximations can be applied to the elastic FWMod forward modelling algorithm as well as the elastic FWM migration algorithm, where we have shown that using the extended Shuey approximations improves the forward and inverse modelling results compared to using the standard Shuey approximations. Finally, we have compared the extended Shuey approximations to the conventional approximations in literature, where we have shown that the extended Shuey approximations achieve comparable performance in cases where the contrasts are low, up to the critical angle, and achieve better results in cases with large contrasts. Based on these results, we conclude that the extended Shuey approximations presented in this paper are a useful addition to the existing approximations to the Zoeppritz equations, specifically in their application in forward and inverse modelling.

2.6. ACKNOWLEDGMENTS

The authors thank the sponsoring companies from the Delphi Consortium at Delft University of Technology for their support to this research.

2.7. APPENDIX

In this section we show the approximations to the full set of reflection and transmission coefficients. Figure 2.7 shows the four terms of $\mathbf{R}^{\cup}$, figure 2.8 shows the four terms of $\mathbf{R}^{\cap}$, figure 2.9 shows the four terms of $\mathbf{T}^{+}$ and figure 2.10 shows the four terms of $\mathbf{T}^{-}$.

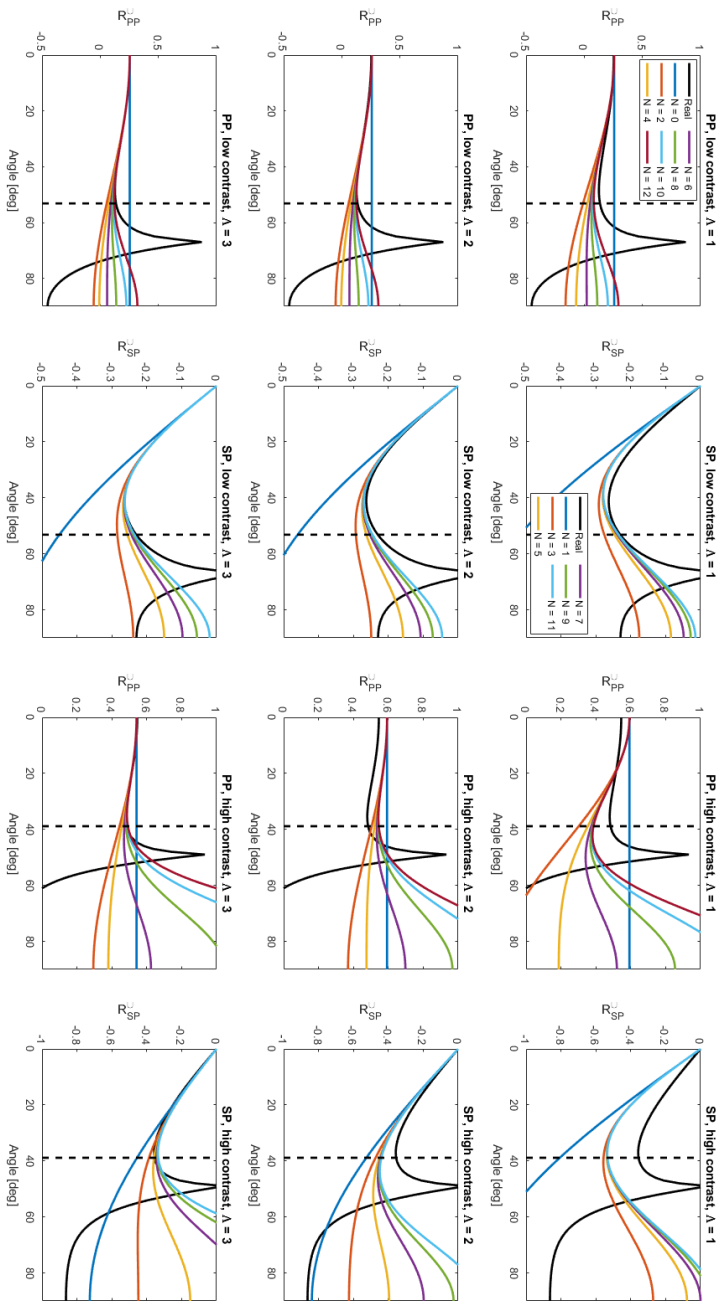

Figure 2.2: A comparison of the extended Shuey approximation to the exact Zoeppritz equations. On the left-hand side, results for a low-contrast interface are shown, while the right-hand side shows the results for a high-contrast interface. The medium parameters used for both interfaces are displayed in table 2.1. Within each figure, the number of contrast terms Λ taken into account is constant, while the different colored lines represent the results for different values of N. These results are compared to the true, Zoeppritz, equations, which are represented by the solid black lines. Also note the dashed vertical lines, which indicate the maximum angle $\theta_{max} = 0.8 \cdot \theta_c$ up to which the approximation holds.

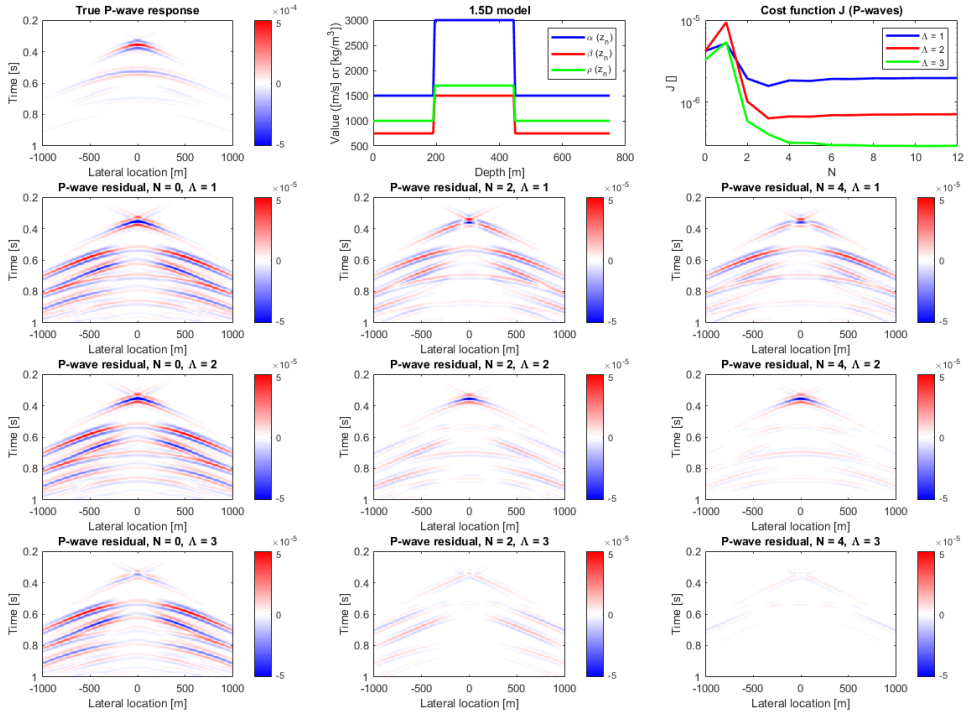

Figure 2.3: Comparison of the FWMod results to true, synthetic, data for P-waves. In the top-left corner the synthetic data, generated using an elastic Kennett algorithm, is displayed. The top-centre image shows the underlying model parameters used. In the top-right corner the cost function J for the P-waves is displayed for different values of N and Λ after 5 iterations. The remaining figures show the data misfit between the synthetic data and the forward modelled data at the surface for different values of N and Λ after 5 iterations. Note that these figures have been clipped to a value of 10% of the maximum value of the data.

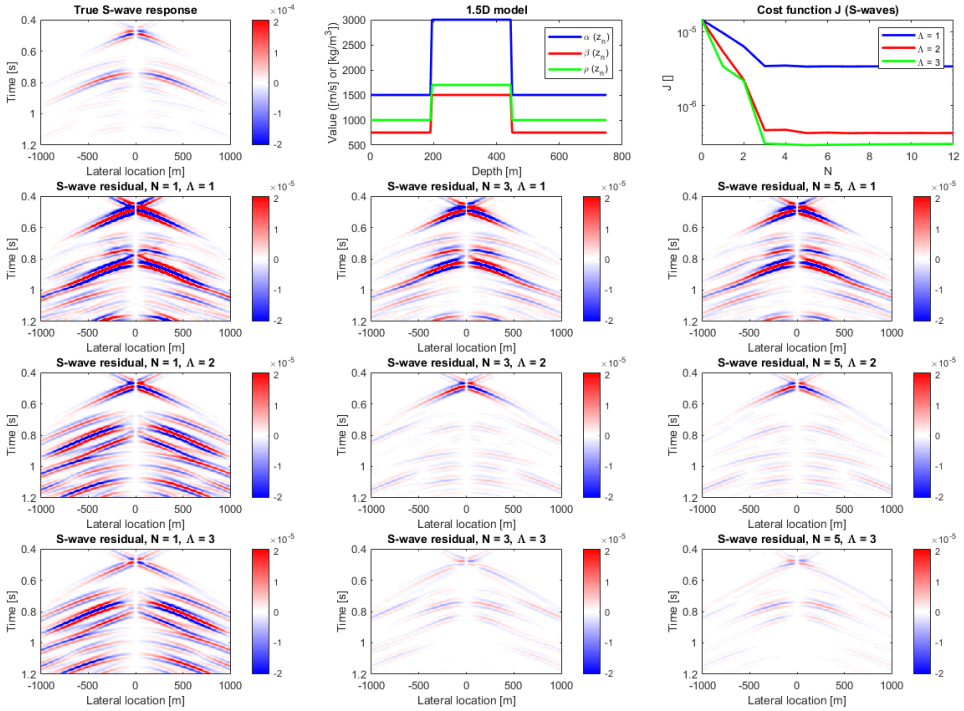

Figure 2.4: Comparison of the FWMod results to true, synthetic, data for S-waves. In the top-left corner the synthetic data, generated using an elastic Kennett algorithm, is displayed. The top-centre image shows the underlying model parameters used. In the top-right corner the cost function J for the S-waves is displayed for different values of N and Λ after 5 iterations. The remaining figures show the data misfit between the synthetic data and the forward modelled data at the surface for different values of N and Λ after 5 iterations. Note that these figures have been clipped to a value of 10% of the maximum value of the data.

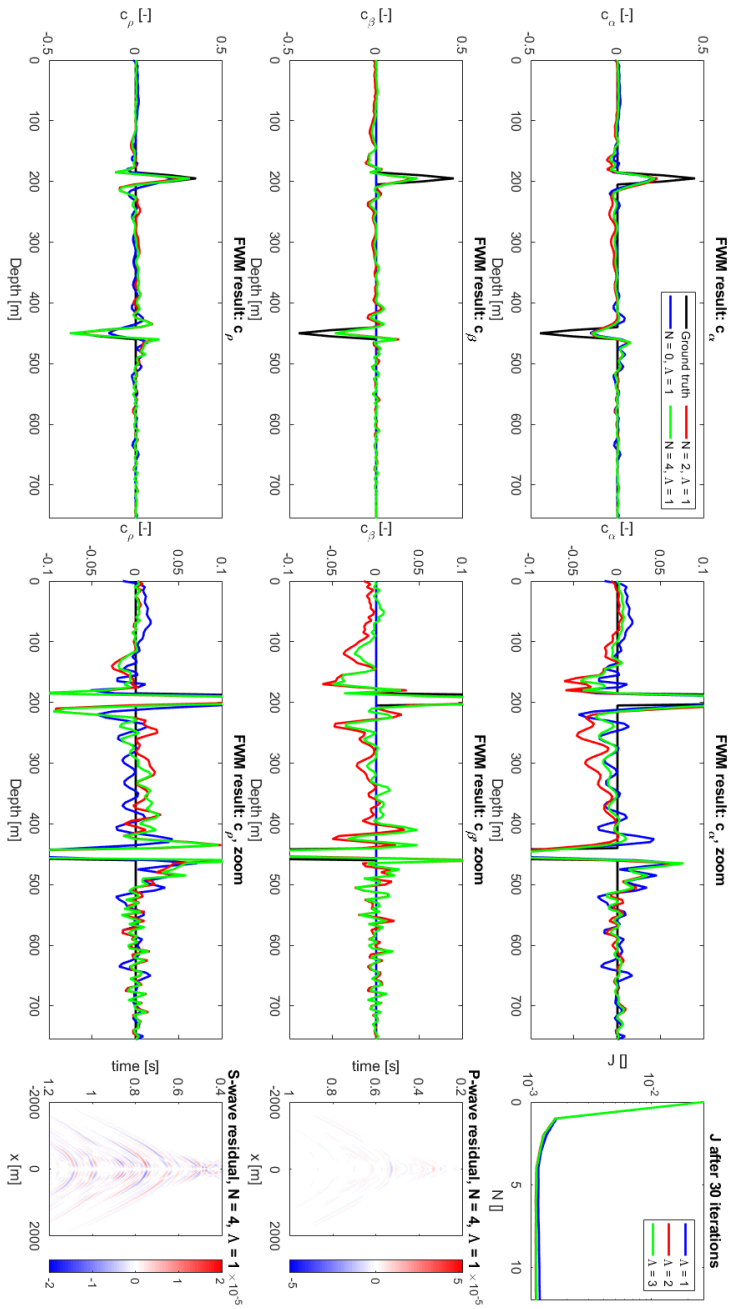

Figure 2.5: Results of the FWM method after 30 iterations, applied to synthetic data generated using an elastic Kennett algorithm. The underlying medium parameters are displayed in table 2.1. On the left-hand side, the results for c_α, c_β and c_ρ are displayed. The band-limited, ground truth contrasts are displayed in black, with the results for different values of N and Λ displayed in different colors. In the top-right corner, the cost function J after 30 iterations is displayed for different values of N and Λ. Finally, the data residual for both $P-$ and $S-$waves after 30 iterations is displayed in the centre-right and bottom-right figures, respectively, for $N = 4$ and $\Lambda = 1$.

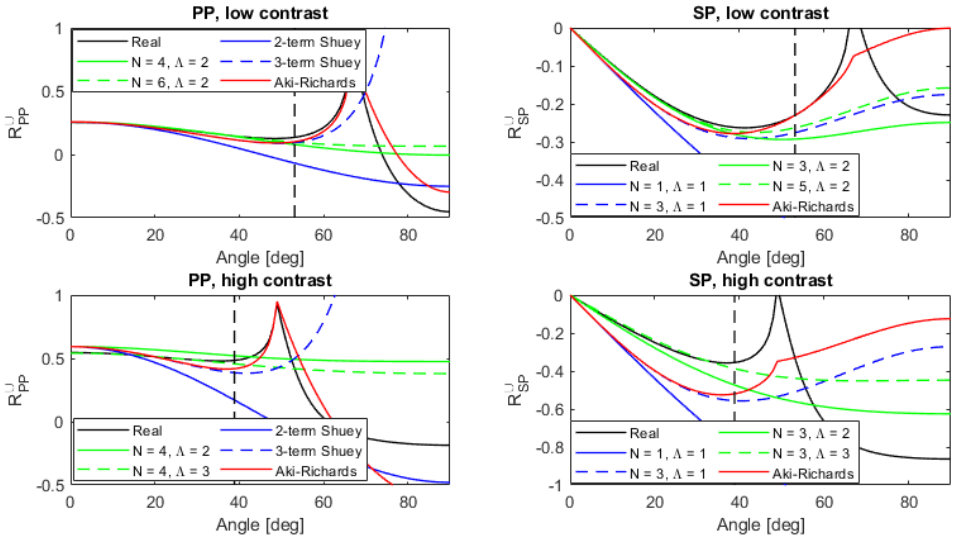

Figure 2.6: Comparison of the extended Shuey approximations with the standard two- and three-term Shuey approximations and the linearised Aki-Richards approximations. On the left-hand side the PP-reflection coefficients are shown for a low and high contrast case. The parameters used are given in table 2.1. On the right-hand side, the SP-reclection coefficients are shown.

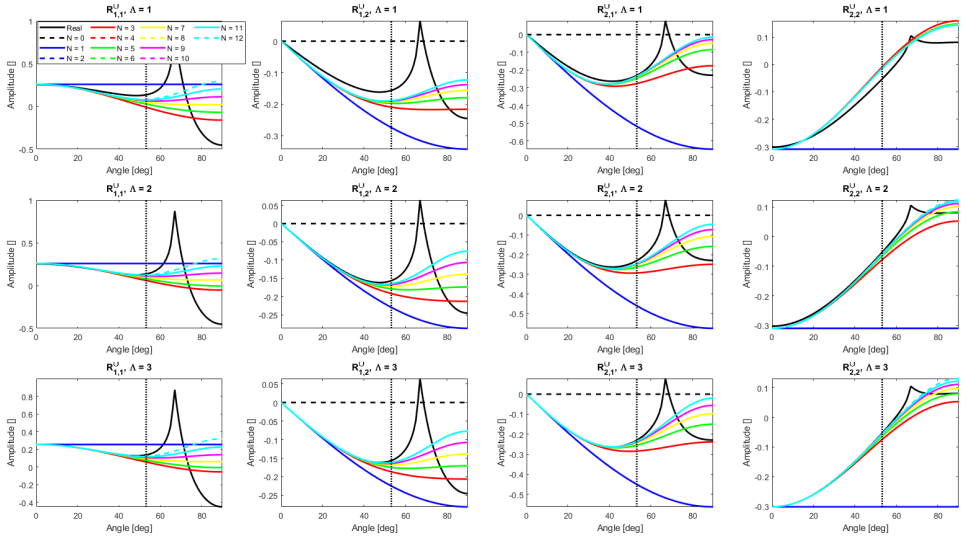

Figure 2.7: A comparison of the extended Shuey approximation to the exact Zoeppritz equations for $\mathbf{R}^{\cup}$. The left-most column shows the 1,1-element, which corresponds to the PP-term. The centre-left column shows the 1,2-element, which corresponds to the PS-term. The centre-right column shows the 2,1-element, which corresponds to the SP-term. Finally, the right-most column shows the 2,2-element, which corresponds to the SS-term. The medium parameters used for the interface correspond to the low-contrast parameters displayed in table 2.1. Within each figure, the number of contrast terms Λ taken into account is constant, while the different colored lines represent the results for different values of N. These results are compared to the true, Zoeppritz, equations, which are represented by the solid black lines. Also note the dashed vertical lines, which indicate the maximum angle $\theta_{max} = 0.8 \cdot \theta_c$ up to which the approximation holds.

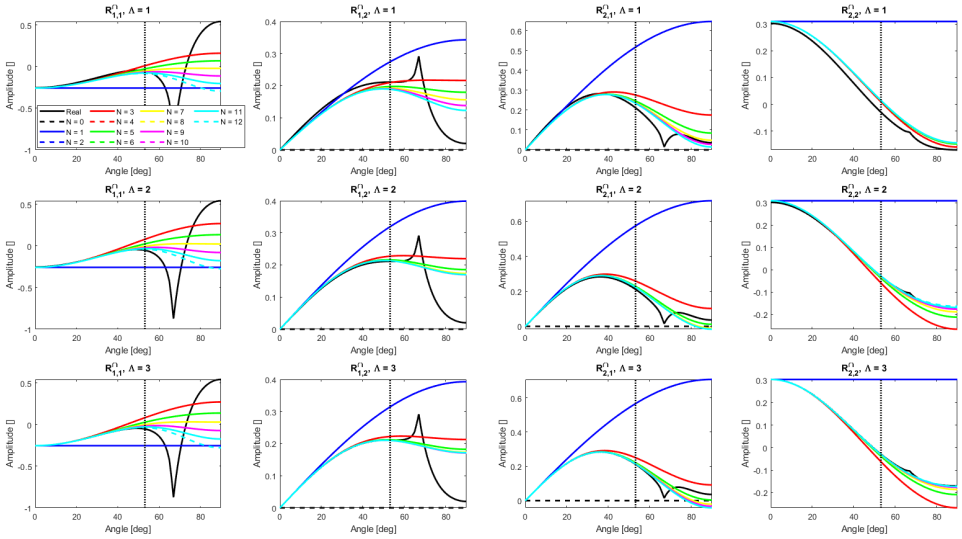

Figure 2.8: Same as figure 2.7, but for the $\mathbf{R}^{\cap}$ terms.

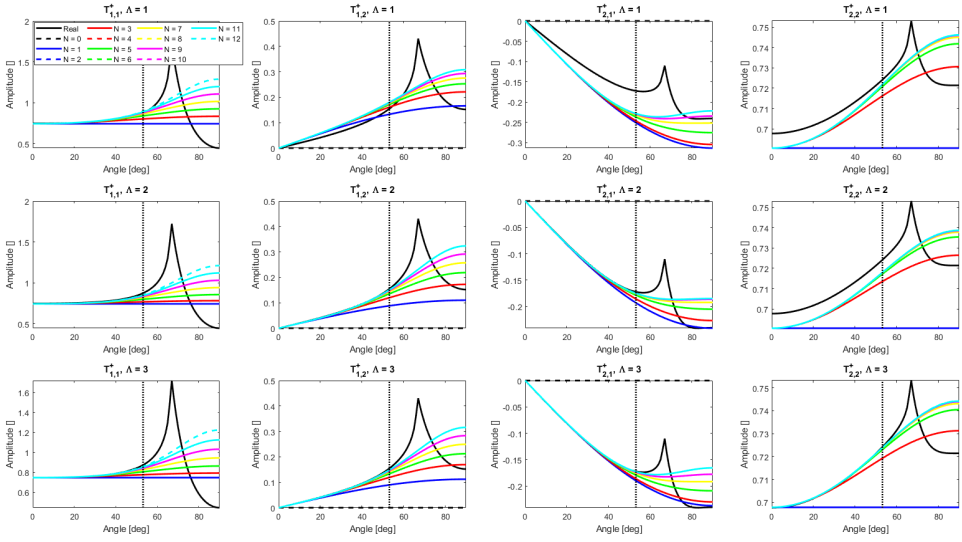

Figure 2.9: Same as figure 2.7, but for the $\mathbf{T}^{+}$ terms.

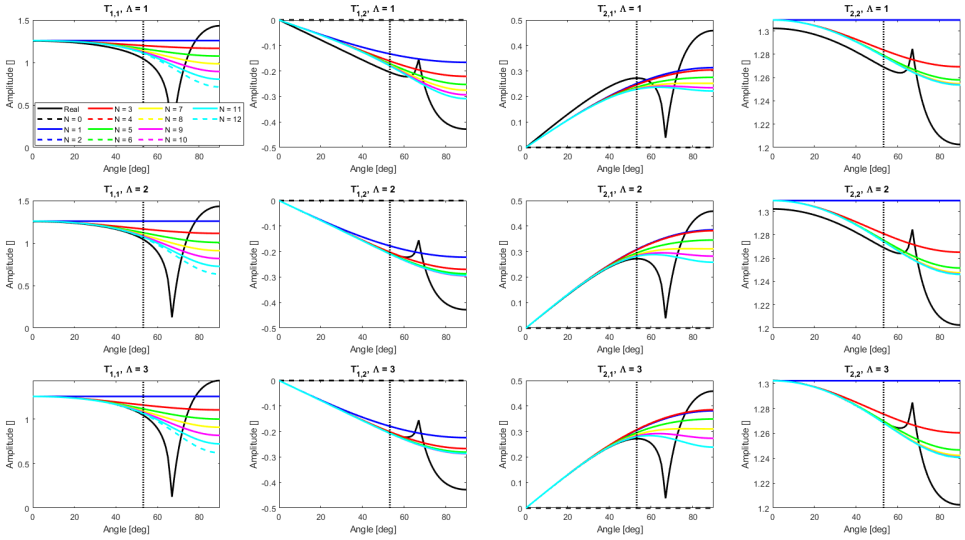

Figure 2.10: Same as figure 2.7, but for the $\mathbf{T}^{-}$ terms.

REFERENCES

[1] R. R. Stewart, J. E. Gaiser, R. J. Brown, and D. C. Lawton. “Converted-wave seismic exploration: Applications”. In: *GEOPHYSICS* 68.1 (Jan. 2003), pp. 40–57. ISSN: 1942-2156. DOI: 10.1190/1.1543193. URL: http://dx.doi.org/10.1190/1.1543193.

[2] K. Zoeppritz. “VII b. Über Reflexion und Durchgang seismischer Wellen durch Unstetigkeitsflächen”. In: *Nachrichten von der Gesellschaft der Wissenschaften zu Göttingen, Mathematisch-Physikalische Klasse* 1919 (1919), pp. 66–84. URL: http://eudml.org/doc/59042.

[3] K. Aki and P. Richards. *Quantitative Seismology, 2nd edition*. 2nd ed. Sausalito, CA: University Science Books, Sept. 2002.

[4] R. T. Shuey. “A simplification of the Zoeppritz equations”. In: *GEOPHYSICS* 50.4 (Apr. 1985), pp. 609–614. ISSN: 1942-2156. DOI: 10.1190/1.1441936. URL: http://dx.doi.org/10.1190/1.1441936.

[5] Y. Wang. “Approximations to the Zoeppritz equations and their use in AVO analysis”. In: *GEOPHYSICS* 64.6 (Nov. 1999), pp. 1920–1927. ISSN: 1942-2156. DOI: 10.1190/1.1444698. URL: http://dx.doi.org/10.1190/1.1444698.

[6] I. F. Jones and I. Davison. “Seismic imaging in and around salt bodies: Problems and pitfalls”. In: *SEG Technical Program Expanded Abstracts 2014*. Society of Exploration Geophysicists, Aug. 2014, pp. 3684–3688. DOI: 10.1190/segam2014-0047.1. URL: http://dx.doi.org/10.1190/segam2014-0047.1.

[7] V. Prieux, R. Brossier, S. Operto, and J. Virieux. “Multiparameter full waveform inversion of multicomponent ocean-bottom-cable data from the Valhall field. Part 2: imaging compressive-wave and shear-wave velocities”. In: *Geophysical Journal International* 194.3 (June 2013), pp. 1665–1681. ISSN: 0956-540X. DOI: 10.1093/gji/ggt178. URL: http://dx.doi.org/10.1093/gji/ggt178.

[8] A. J. Berkhout. “Review Paper: An outlook on the future of seismic imaging, Part I: forward and reverse modelling”. In: *Geophysical Prospecting* 62.5 (Aug. 2014a), pp. 911–930. ISSN: 1365-2478. DOI: 10.1111/1365-2478.12161. URL: http://dx.doi.org/10.1111/1365-2478.12161.

[9] A. J. Berkhout. “Review Paper: An outlook on the future of seismic imaging, Part II: Full-Wavefield Migration”. In: *Geophysical Prospecting* 62.5 (Aug. 2014b), pp. 931–949. ISSN: 1365-2478. DOI: 10.1111/1365-2478.12154. URL: http://dx.doi.org/10.1111/1365-2478.12154.

[10] B. L. N. Kennett. “AN OPERATOR APPROACH TO FORWARD MODELING, DATA PROCESSING AND MIGRATION”. In: *Geophysical Prospecting* 32.6 (Dec. 1984), pp. 1074–1090. ISSN: 1365-2478. DOI: 10.1111/j.1365-2478.1984.tb00755.x. URL: http://dx.doi.org/10.1111/j.1365-2478.1984.tb00755.x.

3

INCLUDING CONVERTED WAVES USING EXTENDED SHUEY'S APPROXIMATIONS IN ELASTIC FULL-WAVEFIELD MIGRATION

The phenomenon of elastic wave conversions, where acoustic, pressure (P-) waves are converted to elastic, shear (S-) waves, and vice-versa, is commonly disregarded in seismic imaging. This can lead to lower-quality images in regions with strong contrasts in elastic parameters. While a number of methods exist that do take wave conversions into account, they either deal with P- and S-waves separately, or are computationally expensive, as is the case for elastic Full-Waveform Inversion. In this paper an alternative approach to taking converted waves into account is presented by extending Full Wavefield Migration (FWM) to account for wave conversions. FWM is a full-wavefield inversion method based on the so-called WRW model in the context of seismic imaging. This WRW model describes wave propagation and scattering in heterogeneous media in terms of convolutional propagation and reflection operators in the space-frequency domain. By applying these operators recursively, multi-scattering data can be modelled. The WRW model is used by the FWM algorithm to reconstruct the reflection properties of the subsurface (i.e. the 'image'). In this paper, the FWM method is extended by accounting for wave conversions due to angle-dependent reflections and transmissions using an extended version of Shuey's approximation. The resulting algorithm is tested on two synthetic models to give a proof of concept. The results of these tests show that the proposed extension can model wave conversions accurately and yields better inversion results than applying conventional, acoustic FWM.

This chapter is based on the manuscript: L. Hoogerbugge, J. van der Neut, K.W.A. van Dongen and D.J. Verschuur. "Including converted waves using Shuey's approximation in elastic Full-Wavefield Migration". Submitted to: Geophysical Journal International

3.1. INTRODUCTION

Although the earth is an elastic medium in reality, most of the time seismic imaging methods have treated it as an acoustic medium, due to the challenges in true elastic modelling. In doing so, many significant results have been achieved. However, certain wave propagation effects in the earth are neglected by treating it as an acoustic medium. Specifically, acoustic methods disregard wave conversions, where pressure (P-) waves are converted to shear (S-) waves and vice versa, as well as the propagation of S-waves through the medium.

Two areas in seismic imaging where these aforementioned effects play a particular role are areas with large contrasts and areas below so-called 'gas clouds'. In the presence of large contrasts, such as around salt structures, the amplitudes of the converted waves may become large, which necessitates a method that takes these conversions into account [1]. Gas clouds, by contrast, block the propagation of P-waves, but not S-waves [2]. Therefore, by incorporating the propagation of S-waves in the imaging process, higher quality images of structures below these areas may be obtained.

At time of writing, there are two main strategies to take wave conversions into account. The first strategy is to perform migration for P- and S-waves separately [3, 4], by changing the velocity profile used. The advantage of these techniques is that they are computationally inexpensive and relatively easy to implement. However, these techniques examine each mode separately, where ideally one would like to examine all modes in an integrated framework. The second strategy is to use a full wavefield technique such as elastic Full-Waveform Inversion (FWI) [5, 6], which takes all elastic effects into account at once. Although these techniques are very powerful, they are very computationally expensive, and run the risk of getting trapped in local minima if the starting model is far from the ground truth.

In this paper, we present a third approach based on an extension of acoustic Full-Wavefield Migration (FWM) to include wave conversions. This can be seen as an approach in-between the two aforementioned strategies. Acoustic FWM is a migration technique introduced by Berkhout [7] and expanded on by others [8–10]. It is based on recursively applying one-way propagation and reflection operators to describe the propagation and scattering of the full wavefield, including all multiples, within the subsurface. It is closely related to the WRW method [11], which can be seen as the primaries-only version of FWM.

The potential for extending acoustic FWM to include converted waves has been recognized from the start [12], as the technique has two main properties which makes it a good candidate for dealing with wave conversions. First, as FWM is an integral-based migration technique, in contrast to the finite-difference-based techniques of FWI, its requirements for the grid size used when describing S-wave propagation are less stringent. Secondly, as the framework has been developed specifically to deal with multiple scattering effects, it can naturally describe multiple wave conversions.

The main challenge in extending acoustic FWM to include wave conversion effects is the angle-dependent nature of the elastic transmission and reflection coefficients. Traditionally, angle-dependent reflection and transmission effects are taken into

account in FWM by inverting for each angle separately [9]. However, when taking wave conversion effects into account, this approach leads to a significant over-parametrisation of the reflection and transmission coefficients, as it would require inverting each of the 16 possible reflection and transmission coefficients separately for every angle.

Therefore, to avoid this over-parametrisation, an extended version of Shuey's approximation, described in chapter 2, is used to link the different reflection and transmission coefficients at all angles. As an additional important benefit, these extended Shuey's approximations reduce the non-linearity present in the full elastic reflection and transmission coefficients, making the resulting problem easier to invert. By combining these approximations with the extension of the framework of FWM to the elastic case [12], we introduce a robust, elastic FWM algorithm which accounts for wave conversions and *S*-wave propagation in a controlled manner.

The remaining part of this paper consists of four sections. First, the elastic FWM algorithm is described in detail in the Theory section. Next, some preliminary results using this method are presented in the Results section. Some general remarks on the presented method are then discussed in the Discussion section. Finally, the conclusions of this paper are presented in the Conclusions section.

3.2. THEORY

In this section, which consists of four parts, we present the theoretical framework for the extension of two-dimensional FWM to account for converted waves. First, we examine the extension of the acoustic FWM forward modelling scheme to include converted waves. Next, we examine the propagation operators for *P*- and *S*-waves in detail. Then, we do the same for the reflection and transmission operators. Finally, we examine the inversion process.

3.2.1. FORWARD MODELLING

To include converted waves in the forward modelling algorithm, we follow the structure used by Berkhout [12] and begin by examining the wavefields at an interface located at a depth level z_n. A schematic representation of this situation is shown in figure 3.1.

At a location right above the interface, which we denote by $\left(x_i, z_n^-\right)$, the *P*-wavefield is given by

$$p_P\left(x_i, z_n^-\right) = p_P^+\left(x_i, z_n^-\right) + q_P^-\left(x_i, z_n^-\right), \tag{3.1}$$

where we have split the *P*-wavefield $p_P\left(x_i, z_n^-\right)$ into a downgoing component, $p_P^+\left(x_i, z_n^-\right)$, travelling towards the interface, and an upgoing component, $q_P^-\left(x_i, z_n^-\right)$, travelling away from the interface. Note that we will work in the temporal Fourier domain throughout this paper, so for example $p_P\left(x_i, z_n^-\right) = p_P\left(x_i, z_n^-, \omega\right)$, with ω the (angular) frequency.

In a similar way, at a location $\left(x_i, z_n^+\right)$ right below the interface, the *P*-wavefield is given by

$$p_P\left(x_i, z_n^+\right) = p_P^-\left(x_i, z_n^+\right) + q_P^+\left(x_i, z_n^+\right), \tag{3.2}$$

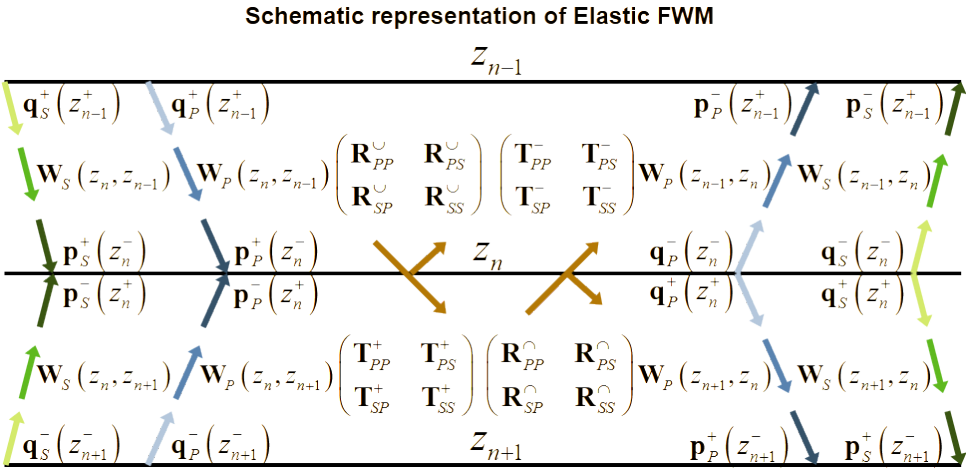

Figure 3.1: Schematic representation of the wavefields and operators at the depth level z_n and the neighbouring levels.

where we have once again split the P-wavefield into an upgoing component, $p_P^-(x_i, z_n^+)$, travelling towards the interface, and a downgoing component, $q_P^+(x_i, z_n^+)$, travelling away from the interface.

Repeating the aforementioned process for the S-wavefield, we write

$$p_S(x_i, z_n^-) = p_S^+(x_i, z_n^-) + q_S^-(x_i, z_n^-), \tag{3.3}$$

$$p_S(x_i, z_n^+) = p_S^-(x_i, z_n^+) + q_S^+(x_i, z_n^+). \tag{3.4}$$

Note the notation used. Superscripts are used to indicate the direction of propagation, where $+$ and $-$ denote downwards and upwards propagation, respectively. The letters p and q are used to denote propagation towards or away from the interface, respectively. Finally, the subscripts P and S are used to differentiate between P- and S-wavefields, respectively.

We are now interested in the relationship between these different wavefields. As a first step, we assume that our modelling takes place on a rectangular grid, meaning that there are N_z equally-spaced depth levels with a spacing of Δz, and each depth level consists of N_x equally-spaced grid points with a spacing of Δx. We then define a vector $\mathbf{p}_P^+(z_n^-)$ of length N_x, with elements $\mathbf{p}_P^+(z_n^-)\big|_i = p_P^+(x_i, z_n^-)$, where the x_i's are the lateral grid points at the depth level z_n. In the same way, we define the corresponding vectors for the other wavefield components introduced in equations 3.1-3.4.

We now define the relationship between the different wavefield components at a depth level z_n. Once again following the formulation used by Berkhout [12], we use convolutional reflection and transmission operators, denoted as $\mathbf{R}^{\cdots}_{\cdots}$ and $\mathbf{T}^{\cdots}_{\cdots}$,

respectively, to write

$$\begin{pmatrix} \mathbf{q}_P^+(z_n^+) \\ \mathbf{q}_S^+(z_n^+) \end{pmatrix} = \begin{pmatrix} \mathbf{R}_{PP}^{\cap} & \mathbf{R}_{PS}^{\cap} \\ \mathbf{R}_{SP}^{\cap} & \mathbf{R}_{SS}^{\cap} \end{pmatrix} \begin{pmatrix} \mathbf{p}_P^-(z_n^+) \\ \mathbf{p}_S^-(z_n^+) \end{pmatrix} + \begin{pmatrix} \mathbf{T}_{PP}^+ & \mathbf{T}_{PS}^+ \\ \mathbf{T}_{SP}^+ & \mathbf{T}_{SS}^+ \end{pmatrix} \begin{pmatrix} \mathbf{p}_P^+(z_n^-) \\ \mathbf{p}_S^+(z_n^-) \end{pmatrix}, \tag{3.5}$$

$$\begin{pmatrix} \mathbf{q}_P^-(z_n^-) \\ \mathbf{q}_S^-(z_n^-) \end{pmatrix} = \begin{pmatrix} \mathbf{R}_{PP}^{\cup} & \mathbf{R}_{PS}^{\cup} \\ \mathbf{R}_{SP}^{\cup} & \mathbf{R}_{SS}^{\cup} \end{pmatrix} \begin{pmatrix} \mathbf{p}_P^+(z_n^-) \\ \mathbf{p}_S^+(z_n^-) \end{pmatrix} + \begin{pmatrix} \mathbf{T}_{PP}^- & \mathbf{T}_{PS}^- \\ \mathbf{T}_{SP}^- & \mathbf{T}_{SS}^- \end{pmatrix} \begin{pmatrix} \mathbf{p}_P^-(z_n^+) \\ \mathbf{p}_S^-(z_n^+) \end{pmatrix}, \tag{3.6}$$

where $\mathbf{R}_{\cdots}^{\cdots}$ and $\mathbf{T}_{\cdots}^{\cdots}$ are matrices of size $N_x \times N_x$ which relate the wavefields above and below the interface. Note that we have dropped the z_n-dependence of these matrices for ease of legibility. These operators are described in more detail in section 3.2.3. For simplicity, we introduce the following shorthand notation for equations 3.5 and 3.6, viz.

$$\mathbf{q}^+(z_n) = \mathbf{R}^{\cap}(z_n)\,\mathbf{p}^-(z_n) + \mathbf{T}^+(z_n)\,\mathbf{p}^+(z_n), \tag{3.7}$$

$$\mathbf{q}^-(z_n) = \mathbf{R}^{\cup}(z_n)\,\mathbf{p}^+(z_n) + \mathbf{T}^-(z_n)\,\mathbf{p}^-(z_n), \tag{3.8}$$

which we will use throughout the rest of this paper.

Next, we examine the relationship between the wavefields at different depth levels z_n. To do this, we introduce a set of propagation operators $\mathbf{W}_{P/S}(z_{n\pm1}, z_n)$ such that

$$\begin{pmatrix} \mathbf{p}_P^+(z_{n+1}^-) \\ \mathbf{p}_S^+(z_{n+1}^-) \end{pmatrix} = \begin{pmatrix} \mathbf{W}_P(z_{n+1}, z_n) & \mathbf{0} \\ \mathbf{0} & \mathbf{W}_S(z_{n+1}, z_n) \end{pmatrix} \begin{pmatrix} \mathbf{q}_P^+(z_n^+) \\ \mathbf{q}_S^+(z_n^+) \end{pmatrix}, \tag{3.9}$$

$$\begin{pmatrix} \mathbf{p}_P^-(z_{n-1}^+) \\ \mathbf{p}_S^-(z_{n-1}^+) \end{pmatrix} = \begin{pmatrix} \mathbf{W}_P(z_{n-1}, z_n) & \mathbf{0} \\ \mathbf{0} & \mathbf{W}_S(z_{n-1}, z_n) \end{pmatrix} \begin{pmatrix} \mathbf{q}_P^-(z_n^-) \\ \mathbf{q}_S^-(z_n^-) \end{pmatrix}, \tag{3.10}$$

with $\mathbf{W}_{P/S}(z_{n\pm1}, z_n)$ matrices of size $N_x \times N_x$ which describe the propagation of waves between the depth levels z_n and $z_{n\pm1}$, and $\mathbf{0}$ the zero matrix of size $N_x \times N_x$. Note that we assume that there is no difference between the propagation of upgoing and downgoing waves between two adjacent depth levels, i.e. $\mathbf{W}_{P/S}(z_{n+1}, z_n) = \mathbf{W}_{P/S}(z_n, z_{n+1})$. These operators are described in more detail in section 3.2.2. We once again introduce shorthand notation for equations 3.9 and 3.10, viz.

$$\mathbf{p}^+(z_{n+1}) = \mathbf{W}(z_{n+1}, z_n)\,\mathbf{q}^+(z_n), \tag{3.11}$$

$$\mathbf{p}^-(z_{n-1}) = \mathbf{W}(z_{n-1}, z_n)\,\mathbf{q}^-(z_n). \tag{3.12}$$

With the building blocks of equations 3.7, 3.8, 3.11 and 3.12 in place, we now examine the forward modelling algorithm. To initialize the algorithm, we set all upgoing and downgoing wavefields to zero, i.e. $\mathbf{p}^{-,0}(z_n) = \mathbf{p}^{+,0}(z_n) = \mathbf{0}$. Note the notation of $\mathbf{p}^{-,0}$ and $\mathbf{p}^{+,0}$, where we have introduced an extra number in the superscript, which denotes how many so-called 'round-trips' have been modelled. Each round-trip increases the maximum order of multiples that are taken into account by one, up to the chosen number of round-trips to be modelled. Furthermore, for simplicity's sake, we assume that there are no sources within the subsurface, only at the surface. Consequently, we set $\mathbf{p}^{+,m}(z_0) = \mathbf{s}_0$ for all m round-trips, where $\mathbf{s}_0$ is a vector containing the source wavefield for one shot at $z = z_0$. Finally, we assume that there are no upgoing waves coming from below the

deepest depth level $z_n = z_{N_z}$. Therefore, we write $\mathbf{p}^{-,m}\left(z_{N_z}\right) = \mathbf{0}$ for all m round-trips.

We then begin by computing the downgoing wavefields for the first round-trip. Starting at $z_n = z_0$, we use equation 3.7 to write

$$\mathbf{q}^{+,1}(z_0) = \mathbf{T}^{+}(z_0)\,\mathbf{p}^{+,1}(z_0) + \mathbf{R}^{\cap}(z_0)\,\mathbf{p}^{-,0}(z_0). \tag{3.13}$$

Next, we apply the propagation operators, using equation 3.11 to write

$$\mathbf{p}^{+,1}(z_1) = \mathbf{W}(z_1, z_0)\,\mathbf{q}^{+,1}(z_0). \tag{3.14}$$

At the depth level $z_n = z_1$ we simply repeat this process with the appropriate transmission, reflection and propagation operators. In this way, we model the downgoing wavefield $\mathbf{p}^{+,1}(z_n)$ at all depth levels.

Next, we compute the upgoing wavefield $\mathbf{p}^{-,1}(z_n)$ at all depth levels. We start at the deepest depth level $z_n = z_{N_z}$. We then use equation 3.8 to write

$$\mathbf{q}^{-,1}\left(z_{N_z}\right) = \mathbf{T}^{-}\left(z_{N_z}\right)\mathbf{p}^{-,1}\left(z_{N_z}\right) + \mathbf{R}^{\cup}\left(z_{N_z}\right)\mathbf{p}^{+,1}\left(z_{N_z}\right), \tag{3.15}$$

and apply the propagation operators of equation 3.12 to write

$$\mathbf{p}^{-,1}\left(z_{N_z-1}\right) = \mathbf{W}\left(z_{N_z-1}, z_{N_z}\right)\mathbf{q}^{-,1}\left(z_{N_z}\right). \tag{3.16}$$

Once again, we continue to apply these operators to find the upgoing wavefield $\mathbf{p}^{-,1}(z_n)$ at each depth level.

We now repeat this process as many times as we wish to account for higher-order scattering, where the scattering order is increased by one after each round-trip. The full process for finding the wavefields $\mathbf{p}^{+,M}(z_n)$ and $\mathbf{p}^{-,M}(z_n)$ for up to M scattering orders is illustrated in algorithm 3.

3.2.2. PROPAGATION OPERATORS

We now examine the propagation operators introduced in equations 3.9 and 3.10 in more detail. To begin, we examine the propagation operators between a depth level z_n and z_{n+1}. We initially assume that the P-wave velocity $\alpha(z_{n+1/2})$ and S-wave velocity $\beta(z_{n+1/2})$ are laterally homogeneous between z_n and z_{n+1} and only vary between depth levels. In that case, the propagation of the P-wavefield between these depth levels is described in the spatial Fourier domain by [13]

$$\hat{p}_P^{+}\left(k_x, z_{n+1}^{-}\right) = e^{-jk_{z,P}(z_{n+1/2})\Delta z}\,\hat{q}_P^{+}\left(k_x, z_n^{+}\right), \tag{3.17}$$

where $j^2 = -1$ and $k_{z,P}(z_{n+1/2})$ is given by

$$k_{z,P}^2(z_{n+1/2}) = \omega^2\alpha^{-2}(z_{n+1/2}) - k_x^2, \tag{3.18}$$

Algorithm 3: Modeling wavefields

Result: $\mathbf{p}^{+,M}(z_n)$ and $\mathbf{p}^{-,M}(z_n)$ for all z_n.
Input: $\mathbf{s}_0$

Set $\mathbf{p}^{-,0}(z_n) = \mathbf{0}$;
for $m = 1 : M$ **do**
  Set $\mathbf{p}^{+,m}(z_0) = \mathbf{s}_0$;
  for $n = 0 : N_z - 1$ **do**
    $\mathbf{q}^{+,m}(z_n) = \mathbf{T}^{+}(z_n)\,\mathbf{p}^{+,m}(z_n) + \mathbf{R}^{\cap}(z_n)\,\mathbf{p}^{-,m-1}(z_n)$;
    $\mathbf{p}^{+,m}(z_{n+1}) = \mathbf{W}(z_{n+1}, z_n)\,\mathbf{q}^{+,m}(z_n)$;
  end
  Set $\mathbf{p}^{-,m}(z_{N_z}) = \mathbf{0}$;
  for $n = N_z{:}1$ **do**
    $\mathbf{q}^{-,m}(z_n) = \mathbf{T}^{-}(z_n)\,\mathbf{p}^{-,m}(z_n) + \mathbf{R}^{\cup}(z_n)\,\mathbf{p}^{+,m}(z_n)$;
    $\mathbf{p}^{-,m}(z_{n-1}) = \mathbf{W}(z_{n-1}, z_n)\,\mathbf{q}^{-,m}(z_n)$;
  end
end

where k_x is the spatial frequency. Note that $\hat{q}_P^+(k_x, z_n^+)$ is obtained by taking the spatial Fourier transform of the wavefield, i.e.

$$\hat{q}_P^+(k_x, z_n^+) = \mathscr{F}\{q_P^+(x, z_n^+)\} = \int_{-\infty}^{+\infty} q_P^+(x, z_n^+)\, e^{jk_x x} dx. \tag{3.19}$$

We now wish to write equation 3.17 in the spatial domain. Using the inverse Fourier transform and the convolution property of the Fourier transform [14], we obtain

$$p_P^+(x_i, z_{n+1}^-) = \int_{-\infty}^{\infty} W_P(x_i - x, z_{n+1}, z_n)\, q_P^+(x, z_n^+)\, dx, \tag{3.20}$$

with $W_P(x, z_{n+1}, z_n)$ defined as

$$W_P(x, z_{n+1}, z_n) = \mathscr{F}^{-1}\left\{e^{-jk_{z,P}(z_{n+1/2})\Delta z}\right\}. \tag{3.21}$$

Note that $W_P(x, z_{n+1}, z_n)$ is an even function with respect to x, as $e^{-jk_{z,P}(z_{n+1/2})\Delta z}$ is an even function with respect to k_x. Therefore, we write

$$W_P(x_i - x, z_{n+1}, z_n) = W_P(x - x_i, z_{n+1}, z_n) = \mathscr{F}^{-1}\left\{e^{-jk_{z,P}(z_{n+1/2})\Delta z} e^{jk_x x_i}\right\}. \tag{3.22}$$

We now discretize equation 3.20 as follows

$$p_P^+(x_i, z_{n+1}^-) = \sum_{j=1}^{N_x} W_P(x_j - x_i, z_{n+1}, z_n)\, q_P^+(x_j, z_n^+)\, \Delta x, \tag{3.23}$$

where we have used equation 3.22. Rewriting equation 3.23 using the notation of equation 3.9 yields

$$\mathbf{p}_P^+\left(z_{n+1}^-\right) = \mathbf{W}_P\left(z_{n+1}, z_n\right)\mathbf{q}_P^+\left(z_n^+\right), \tag{3.24}$$

where $\mathbf{W}_P\left(z_{n+1}, z_n\right)$ is a matrix of size $N_x \times N_x$. Combining equations 3.23 and 3.24, we see that the elements of the propagation operator $\mathbf{W}_P\left(z_{n+1}, z_n\right)$ are given by

$$\mathbf{W}_P\left(z_{n+1}, z_n\right)|_{ij} = W_P\left(x_j - x_i, z_{n+1}, z_n\right)\Delta x, \tag{3.25}$$

with $W_P\left(x_j - x_i, z_{n+1}, z_n\right)$ defined according to equation 3.22.

In a similar way, one can construct the S-wave propagation operator $\mathbf{W}_S\left(z_{n+1}, z_n\right)$ by replacing the P-wave velocity $\alpha\left(z_{n+1/2}\right)$ in equation 3.18 with the S-wave velocity $\beta\left(z_{n+1/2}\right)$, viz.

$$k_{z,S}^2\left(z_{n+1/2}\right) = \omega^2\beta^{-2}\left(z_{n+1/2}\right) - k_x^2, \tag{3.26}$$

and following the same steps as above.

In situations where the P- or S-wave velocities are not laterally homogeneous, we approximate the propagation operators by using the local velocity $\alpha\left(x_i, z_{n+1/2}\right)$ or $\beta\left(x_i, z_{n+1/2}\right)$. In this case, $k_{z,P/S}\left(z_{n+1/2}\right)$ becomes laterally heterogeneous, i.e. $k_{z,P}^2\left(x_i, z_{n+1/2}\right) = \omega^2\alpha^{-2}\left(x_i, z_{n+1/2}\right) - k_x^2$. Using this heterogeneous $k_{z,P/S}\left(x_i, z_{n+1/2}\right)$, we approximate the laterally heterogeneous propagation operator by extending equation 3.22, i.e.

$$W_{P/S}\left(x - x_i, z_{n+1}, z_n\right) = \mathscr{F}^{-1}\left\{e^{-jk_{z,P/S}\left(x_i, z_{n+1/2}\right)\Delta z}e^{jk_x x_i}\right\}. \tag{3.27}$$

This approximation is reasonable under the condition that the lateral variations in the velocity profile are smooth. In situations where this is not the case, alternative forms of the propagation operator can be used [15–17].

Finally, we note that evanescent waves cannot be handled within this framework. In order to prevent these waves from creating problems within the inversion, we add a spatial filter to remove them. This gives us the final form of equation 3.22, viz.

$$W_{P/S}\left(x - x_i, z_{n+1}, z_n\right) = \mathscr{F}^{-1}\left\{e^{-jk_{z,P/S}\left(x_i, z_{n+1/2}\right)\Delta z}e^{jk_x x_i}F_{P/S}\left(k_x, x_i, z_{n+1/2}\right)\right\}, \tag{3.28}$$

where the spatial filter $F_P\left(k_x, x_i, z_{n+1/2}\right)$ is defined as

$$F_P\left(k_x, x_i, z_{n+1/2}\right) = \begin{cases} 1 & \forall\,|k_x| < \omega\alpha^{-1}\left(x_i, z_{n+1/2}\right), \\ 0 & \text{else.} \end{cases}, \tag{3.29}$$

with a similar definition for $F_S\left(k_x, x_i, z_{n+1/2}\right)$.

3.2.3. REFLECTION AND TRANSMISSION OPERATORS

In a similar way to the previous section, we now examine the reflection and transmission operators introduced in equations 3.5 and 3.6. As discussed in the introduction, we use an extended version of Shuey's approximation [18], described in chapter 2, to couple the reflection and transmission coefficients and to reduce the amount of non-linearity present in the full (Zoeppritz) elastic transmission and

reflection coefficients. To start, we assume a flat reflector at the depth level z_n, and assume the incident P-wavefield to be a plane wave, striking the interface at an angle θ. In this case, we can approximate the true PP-reflection coefficient by taking a Taylor expansion with respect to the angle $\sin(\theta)$ and the contrasts c_α, c_β and c_ρ. Grouping the terms of this Taylor expansion with respect to the order of the angle κ and the total order of the contrasts λ we write

$$R^{\cup}_{PP}\left(\sin(\theta), c_\alpha, c_\beta, c_\rho\right) \approx \sum_{\kappa=0}^{K}\sum_{\lambda=0}^{\Lambda}\left(\tilde{R}^{\cup}_{PP}\right)^{\kappa}_{\lambda}\sin^{\kappa}(\theta), \tag{3.30}$$

with

$$\left(\tilde{R}^{\cup}_{PP}\right)^{\kappa}_{\lambda} = \sum_{m=0}^{\lambda}\sum_{k=0}^{\lambda-m}\frac{1}{\kappa!m!k!(\lambda-k-m)!}\left.\frac{d^{\kappa+\lambda}R^{\cup}_{PP}}{d(\sin(\theta))^{\kappa}dc_\alpha^m dc_\beta^k dc_\rho^{(\lambda-k-m)}}\right|_{(\mathbf{0})} c_\alpha^m c_\beta^k c_\rho^{(\lambda-k-m)}, \tag{3.31}$$

where $R^{\cup}_{PP}$ is the full, Zoeppritz PP-reflection coefficient for waves from above [19] and with the dimensionless contrast parameters c_α, c_β and c_ρ defined as

$$c_\alpha = \frac{\alpha\left(z_n^+\right)-\alpha\left(z_n^-\right)}{\frac{1}{2}\left[\alpha\left(z_n^+\right)+\alpha\left(z_n^-\right)\right]},\ c_\beta = \frac{\beta\left(z_n^+\right)-\beta\left(z_n^-\right)}{\frac{1}{2}\left[\beta\left(z_n^+\right)+\beta\left(z_n^-\right)\right]},\ c_\rho = \frac{\rho\left(z_n^+\right)-\rho\left(z_n^-\right)}{\frac{1}{2}\left[\rho\left(z_n^+\right)+\rho\left(z_n^-\right)\right]}, \tag{3.32}$$

where z_n^+ and z_n^- denote depth levels just below and above the interface, respectively. While equation 3.31 is difficult to evaluate by hand, it can be straightforwardly evaluated using mathematical software such as Maple. Evaluating the above expression for $N=2$ and $\Lambda=1$, for example, we find

$$R^{\cup}_{PP}\left(\sin(\theta), c_\alpha, c_\beta, c_\rho\right) \approx \frac{1}{2}\left(c_\alpha + c_\rho\right) + \left(\frac{1}{2}c_\alpha - 2\hat{V}^2\left(c_\rho + 2c_\beta\right)\right)\sin^2(\theta), \tag{3.33}$$

which is just the conventional, 2-term Shuey approximation, written in the notation used in this paper.

If the incoming P-wavefield is not a pure plane wave, we use the spatial Fourier transform to decompose the wavefield into plane-wave components. In this domain, the angle of incidence θ_n is given by

$$\sin(\theta_n) = \frac{\bar{\alpha}(z_n)\,k_x}{\omega}, \tag{3.34}$$

where $\bar{\alpha}(z_n) = \frac{1}{2}\left[\alpha\left(z_n^+\right)+\alpha\left(z_n^-\right)\right]$. Note that the angle of incidence depends on the depth level at which the reflector is located, as indicated by the notation θ_n. Using equations 3.30 and 3.34, we approximate the action of the PP-reflection coefficient $R^{\cup}_{PP}$ on the downgoing P-wavefield at $z=z_n$ in the k_x domain as

$$R^{\cup}_{PP}(k_x, z_n)\,\hat{p}^+_P(k_x, z_n) \approx \sum_{\kappa=0}^{K}\sum_{\lambda=0}^{\Lambda}\left(\tilde{R}^{\cup}_{PP}\right)^{\kappa}_{\lambda}\left(\frac{\bar{\alpha}(z_n)}{\omega}\right)^{\kappa} k_x^{\kappa}\,\hat{p}^+_P(k_x, z_n). \tag{3.35}$$

We now take the inverse Fourier transform of equation 3.35 to find the action of the reflection operator in the space domain. Using the convolution property of the Fourier transform [14] we write

$$\mathscr{F}^{-1}\left\{R^{\cup}_{PP}(k_x,z_n)\,\hat{p}^{+}_{P}(k_x,z_n)\right\} \approx \sum_{\kappa=0}^{K}\sum_{\lambda=0}^{\Lambda}\left(\tilde{R}^{\cup}_{PP}\right)^{\kappa}_{\lambda} S^{\kappa}_{\theta}(x,z_n) * p^{+}_{P}(x,z_n), \tag{3.36}$$

where $*$ represents a convolution with respect to the spatial coordinate x, and where

$$S^{\kappa}_{\theta}(x,z_n) = \mathscr{F}^{-1}\left\{\left(\frac{\bar{\alpha}(z_n)}{\omega}\right)^{\kappa} k_x^{\kappa}\right\}. \tag{3.37}$$

Following the approach of section 3.2.2, we now discretize equation 3.36 to find the discretized reflection operator

$$\mathbf{R}^{\cup}_{PP}(z_n)\,\mathbf{p}^{+}_{P}(z_n) \approx \sum_{\kappa=0}^{K}\sum_{\lambda=0}^{\Lambda}\left(\tilde{\mathbf{R}}^{\cup}_{PP}\right)^{\kappa}_{\lambda}(z_n)\,\mathbf{S}^{\kappa}_{\theta}(z_n)\,\mathbf{p}^{+}_{P}(x,z_n), \tag{3.38}$$

where the matrices $\mathbf{R}^{\cup}_{PP}(z_n)$, $\left(\tilde{\mathbf{R}}^{\cup}_{PP}\right)^{\kappa}_{\lambda}(z_n)$ and $\mathbf{S}^{\kappa}_{\theta}(z_n)$ are matrices of size $N_x \times N_x$. Using the definition of the convolution, we see that the elements of $\mathbf{S}^{\kappa}_{\theta}(z_n)$ are given by

$$\mathbf{S}^{\kappa}_{\theta}(z_n)\big|_{ij} = (-1)^{\kappa} S^{\kappa}_{\theta}\left(x_j - x_i, z_n\right)\Delta x, \tag{3.39}$$

where we have used that $S^{\kappa}_{\theta}\left(x_j - x_i, z_n\right)$ is an even function for even values of κ and an odd function for odd values of κ. Using equation 3.31 we write the matrices $\left(\tilde{\mathbf{R}}^{\cup}_{PP}\right)^{\kappa}_{\lambda}$ as

$$\left(\tilde{\mathbf{R}}^{\cup}_{PP}\right)^{\kappa}_{\lambda}(z_n) = \sum_{m=0}^{\lambda}\sum_{k=0}^{\lambda-m}\frac{1}{\kappa!m!k!(\lambda-k-m)!}\left.\frac{d^{\kappa+\lambda}R^{\cup}_{PP}}{d(\sin(\theta))^{\kappa}dc_{\alpha}^{m}dc_{\beta}^{k}dc_{\rho}^{(\lambda-k-m)}}\right|_{(\mathbf{0})}\mathbf{C}^{m}_{\alpha}(z_n)\,\mathbf{C}^{k}_{\beta}(z_n)\,\mathbf{C}^{(\lambda-k-m)}_{\rho}(z_n), \tag{3.40}$$

where the matrices $\mathbf{C}_{\alpha}(z_n)$, $\mathbf{C}_{\beta}(z_n)$ and $\mathbf{C}_{\rho}(z_n)$ are diagonal matrices of size $N_x \times N_x$ with elements

$$\mathbf{C}_{\ldots}(z_n)|_{ij} = c_{\ldots}(x_i,z_n)\,\delta_{ij}. \tag{3.41}$$

We now expand the approach used above to construct the remaining parts of the reflection and transmission operators. We write the full reflection operator $\mathbf{R}^{\cup}(z_n)$ as

$$\mathbf{R}^{\cup}(z_n) = \begin{pmatrix} \mathbf{R}^{\cup}_{PP} & \mathbf{R}^{\cup}_{PS} \\ \mathbf{R}^{\cup}_{SP} & \mathbf{R}^{\cup}_{SS} \end{pmatrix} \approx \sum_{\kappa=0}^{K}\sum_{\lambda=0}^{\Lambda}\begin{pmatrix} \left(\tilde{\mathbf{R}}^{\cup}_{PP}\right)^{\kappa}_{\lambda}\mathbf{S}^{\kappa}_{\theta} & \left(\tilde{\mathbf{R}}^{\cup}_{PS}\right)^{\kappa}_{\lambda}\mathbf{S}^{\kappa}_{\theta} \\ \left(\tilde{\mathbf{R}}^{\cup}_{SP}\right)^{\kappa}_{\lambda}\mathbf{S}^{\kappa}_{\theta} & \left(\tilde{\mathbf{R}}^{\cup}_{SS}\right)^{\kappa}_{\lambda}\mathbf{S}^{\kappa}_{\theta} \end{pmatrix}, \tag{3.42}$$

where we have omitted the z_n dependency for ease of legibility. In equation 3.42 $\left(\tilde{\mathbf{R}}^{\cup}_{PS}\right)^{\kappa}_{\lambda}$, $\left(\tilde{\mathbf{R}}^{\cup}_{SP}\right)^{\kappa}_{\lambda}$ and $\left(\tilde{\mathbf{R}}^{\cup}_{SS}\right)^{\kappa}_{\lambda}$ are matrices of size $N_x \times N_x$ defined in a similar way as

$\left(\tilde{\mathbf{R}}^{\cup}_{PP}\right)^{\kappa}_{\lambda}$, i.e.

$$\left(\tilde{\mathbf{R}}^{\cup}_{SP}\right)^{\kappa}_{\lambda}(z_n) = \sum_{m=0}^{\lambda}\sum_{k=0}^{\lambda-m}\frac{1}{\kappa!m!k!(\lambda-k-m)!}\left.\frac{d^{\kappa+\lambda}R^{\cup}_{SP}}{d(\sin(\theta))^{\kappa}dc_{\alpha}^{m}dc_{\beta}^{k}dc_{\rho}^{(\lambda-k-m)}}\right|_{(\mathbf{0})}\mathbf{C}_{\alpha}^{m}(z_n)\mathbf{C}_{\beta}^{k}(z_n)\mathbf{C}_{\rho}^{(\lambda-k-m)}(z_n). \tag{3.43}$$

The remaining reflection operator $\mathbf{R}^{\cap}(z_n)$ and the transmission operators $\mathbf{T}^{+}(z_n)$ and $\mathbf{T}^{-}(z_n)$ are defined in an analogous way.

Finally, we consider the case where the reflector is not a flat layer. In this case, we must adjust the angle of incidence θ to account for the local dip. We assume that the interface can be locally approximated to be a flat plane under an angle θ_0. In that case, we use the trigonometric identities $\sin(\theta+\theta_0) = \sin(\theta)\cos(\theta_0) + \cos(\theta)\sin(\theta_0)$ and $\cos(\theta) = \sqrt{1-\sin^2(\theta)}$ to write

$$\sin^{\kappa'}(\theta+\theta_0) = \left[\sin(\theta)\cos(\theta_0) + \sqrt{1-\sin^2(\theta)}\sin(\theta_0)\right]^{\kappa'}. \tag{3.44}$$

Taking a Taylor expansion with respect to $\sin(\theta)$ gives

$$\sin^{\kappa'}(\theta+\theta_0) \approx \sum_{\kappa=0}^{K} s_{\kappa}^{\kappa'}(\theta_0)\sin^{\kappa}(\theta), \tag{3.45}$$

with

$$s_{\kappa}^{\kappa'}(\theta_0) = \frac{1}{\kappa!}\left.\frac{d^{\kappa}\sin^{\kappa'}(\theta+\theta_0)}{d(\sin(\theta))^{\kappa}}\right|_{0}. \tag{3.46}$$

Combining equations 3.45 and 3.30 we can approximate the true PP-reflection coefficient for a dipping reflector by

$$R^{\cup}_{PP}\left(\sin(\theta+\theta_0), c_{\alpha}, c_{\beta}, c_{\rho}\right) \approx \sum_{\kappa'=0}^{K}\sum_{\lambda=0}^{\Lambda}\left(\tilde{R}^{\cup}_{PP}\right)^{\kappa'}_{\lambda}\sin^{\kappa'}(\theta+\theta_0) \approx \sum_{\kappa=0}^{K}\sum_{\kappa'=0}^{K}\sum_{\lambda=0}^{\Lambda}\left(\tilde{R}^{\cup}_{PP}\right)^{\kappa'}_{\lambda}s_{\kappa}^{\kappa'}(\theta_0)\sin^{\kappa}(\theta). \tag{3.47}$$

Using equation 3.47, we can write the PP-reflection operator for a dipping reflector as

$$\mathbf{R}^{\cup}_{PP}(z_n) \approx \sum_{\kappa=0}^{K}\sum_{\kappa'=0}^{K}\sum_{\lambda=0}^{\Lambda}\left(\tilde{\mathbf{R}}^{\cup}_{PP}\right)^{\kappa'}_{\lambda}(z_n)\mathbf{S}_{\kappa}^{\kappa'}(\theta_0)\mathbf{S}_{\theta}^{\kappa}(z_n), \tag{3.48}$$

where $\mathbf{S}_{\kappa}^{\kappa'}(\theta_0)$ is a diagonal matrix of size $N_x \times N_x$ with elements

$$\left.\mathbf{S}_{\kappa}^{\kappa'}(\theta_0)\right|_{ij} = s_{\kappa}^{\kappa'}(\theta_0(x_i, z_n))\,\delta_{ij}. \tag{3.49}$$

Note that we assume the local dip of the reflector to be known in equation 3.45. In practice, this can be computed by first using a conventional imaging technique, or performing a single iteration of elastic FWM using $\theta_0 = 0$, followed by a local dip estimation scheme, such as the one developed by Fomel [20].

3.2.4. INVERSION PROCESS

In this section, we examine the inversion process associated with the forward modelling scheme described earlier. We consider a seismic experiment with N_S sources with a known source wavefield $\mathbf{s}_0(z_0)$, N_x receivers located at the surface and N_ω measured frequencies. In this case, we define the mismatch between the measured data and the forward modelled wavefields at the surface after M round trips as

$$J = \frac{1}{2}\sum_{i=1}^{N_\omega}\sum_{j=1}^{N_S}\left\|\mathbf{e}\left(z_0, s_j, \omega_i, c_\alpha, c_\beta, c_\rho\right)\right\|^2, \tag{3.50}$$

where we have defined the residual $\mathbf{e}$ as

$$\mathbf{e}\left(z_0, s_j, \omega_i, c_\alpha, c_\beta, c_\rho\right) = \mathbf{d}\left(z_0, s_j, \omega_i\right) - \mathbf{p}^{-,M}\left(z_0, s_j, \omega_i, c_\alpha, c_\beta, c_\rho\right), \tag{3.51}$$

with $\mathbf{d}\left(z_0, s_j, \omega_i\right)$ the known data recorded at the surface and the $L2$-norm $\|\cdot\|^2$ defined as

$$\left\|\mathbf{p}\right\|^2 = \sum_{i=1}^{N_x}\left(\left|p_P(x_i)\right|^2 + \left|p_S(x_i)\right|^2\right). \tag{3.52}$$

Note that in equation 3.50 we have explicitly written the dependence of the forward modelled wavefields $\mathbf{p}^{-,M}$ on the contrasts c_α, c_β and c_ρ, the source s_j and the frequency ω_i.

We now apply a gradient descent scheme with respect to the contrasts c_α, c_β and c_ρ to minimize the objective function J. To do this, we must first compute the gradient with respect to the contrast parameters. Using algorithm 1, we write the contribution to the forward modelled wavefields at the surface due to the contrasts at a depth level z_n as

$$\begin{aligned}\mathbf{p}^{-,M}(z_0; z_n) =& \bar{\mathbf{W}}^{-}(z_0, z_n)\left[\mathbf{R}^{\cup}(z_n)\,\mathbf{p}^{+,M}(z_n) + \mathbf{T}^{-}(z_n)\,\mathbf{p}^{-,M}(z_n)\right] + \\ & \bar{\mathbf{W}}^{\cup}(z_0, z_n)\left[\mathbf{R}^{\cap}(z_n)\,\mathbf{p}^{-,M}(z_n) + \mathbf{T}^{+}(z_n)\,\mathbf{p}^{+,M}(z_n)\right],\end{aligned} \tag{3.53}$$

where we have introduced the operators $\bar{\mathbf{W}}^{-}(z_0, z_n)$ and $\bar{\mathbf{W}}^{\cup}(z_0, z_n)$. These operators are constructed by applying sequences of propagation, reflection and transmission operators and are defined as

$$\bar{\mathbf{W}}^{-}\left(z_j, z_i\right) = \prod_{m=i-1}^{j+1}\left[\mathbf{W}(z_{m-1}, z_m)\,\mathbf{T}^{-}(z_m)\right]\mathbf{W}(z_{i-1}, z_i)\ \ \forall\, j < i, \tag{3.54}$$

$$\bar{\mathbf{W}}^{+}\left(z_j, z_i\right) = \prod_{m=i+1}^{j-1}\left[\mathbf{W}(z_{m+1}, z_m)\,\mathbf{T}^{-}(z_m)\right]\mathbf{W}(z_{i+1}, z_i)\ \ \forall\, j > i, \tag{3.55}$$

$$\bar{\mathbf{W}}^{\cup}(z_0, z_n) = \sum_{m=n+1}^{N_z} \bar{\mathbf{W}}^{-}(z_0, z_m)\,\mathbf{R}^{\cup}(z_m)\,\bar{\mathbf{W}}^{+}(z_m, z_n). \tag{3.56}$$

For simplicities' sake, we will focus on the first term of equation 3.53, viz.

$$\mathbf{p}^{-,M}\left(z_0; z_n, R^{\cup}\right) = \bar{\mathbf{W}}^{-}(z_0, z_n)\,\mathbf{R}^{\cup}(z_n)\,\mathbf{p}^{+,M}(z_n). \tag{3.57}$$

Taking the derivative of $\mathbf{p}^{-,M}$ with respect to the contrast $c_\alpha(x_i, z_n)$ gives

$$\begin{aligned}\frac{\partial p_P^{-,M}\left(x_j, z_0; z_n, R^{\cup}\right)}{\partial c_\alpha(x_i, z_n)} = &\bar{\mathbf{W}}_{PP}^{-}(z_0, z_n)\big|_{ji}\frac{\partial \tilde{q}_P^{-,M}(x_i, z_n)}{\partial c_\alpha(x_i, z_n)} + \\ &\bar{\mathbf{W}}_{PS}^{-}(z_0, z_n)\big|_{ji}\frac{\partial \tilde{q}_S^{-,M}(x_i, z_n)}{\partial c_\alpha(x_i, z_n)},\end{aligned} \tag{3.58}$$

$$\begin{aligned}\frac{\partial p_S^{-,M}\left(x_j, z_0; z_n, R^{\cup}\right)}{\partial c_\alpha(x_i, z_n)} = &\bar{\mathbf{W}}_{SP}^{-}(z_0, z_n)\big|_{ji}\frac{\partial \tilde{q}_P^{-,M}(x_i, z_n)}{\partial c_\alpha(x_i, z_n)} + \\ &\bar{\mathbf{W}}_{SS}^{-}(z_0, z_n)\big|_{ji}\frac{\partial \tilde{q}_S^{-,M}(x_i, z_n)}{\partial c_\alpha(x_i, z_n)},\end{aligned} \tag{3.59}$$

where we have introduced the wavefields $\tilde{\mathbf{q}}^{-,M}(z_n)$, which, based on equation 2.25, are defined as $\tilde{\mathbf{q}}^{-,M}(z_n) = \mathbf{R}^{\cup}(z_n)\,\mathbf{p}^{+,M}(z_n)$. Taking the derivative of these wavefields with respect to $c_\alpha(x_i, z_n)$ yields

$$\frac{\partial \tilde{q}_P^{-,M}(x_i, z_n)}{\partial c_\alpha(x_i, z_n)} = \sum_{j=1}^{N_x}\frac{\partial \mathbf{R}_{PP}^{\cup}(z_n)\big|_{ij}}{\partial c_\alpha(x_i, z_n)}p_P^{+,M}(x_j, z_n) + \sum_{j=1}^{N_x}\frac{\partial \mathbf{R}_{PS}^{\cup}(z_n)\big|_{ij}}{\partial c_\alpha(x_i, z_n)}p_S^{+,M}(x_j, z_n), \tag{3.60}$$

$$\frac{\partial \tilde{q}_S^{-,M}(x_i, z_n)}{\partial c_\alpha(x_i, z_n)} = \sum_{j=1}^{N_x}\frac{\partial \mathbf{R}_{SP}^{\cup}(z_n)\big|_{ij}}{\partial c_\alpha(x_i, z_n)}p_P^{+,M}(x_j, z_n) + \sum_{j=1}^{N_x}\frac{\partial \mathbf{R}_{SS}^{\cup}(z_n)\big|_{ij}}{\partial c_\alpha(x_i, z_n)}p_S^{+,M}(x_j, z_n), \tag{3.61}$$

where we have used the fact that the contrasts $c_\alpha(x_i, z_n)$ at different locations are independent variables. Finally, note the use of the partial extended propagation operators $\bar{\mathbf{W}}_{PP}^{-}$, $\bar{\mathbf{W}}_{PS}^{-}$, $\bar{\mathbf{W}}_{SP}^{-}$ and $\bar{\mathbf{W}}_{SS}^{-}$ in equation 3.58. These are matrices of size $N_x \times N_x$, which are related to the full operator $\bar{\mathbf{W}}^{-}$ in the same way as the partial reflection and transmission operators of equation 3.6. We now examine these derivatives in more detail. Using equation 3.38, we expand $\frac{\partial \mathbf{R}_{PP}^{\cup}(z_n)\big|_{ij}}{\partial c_\alpha(x_i, z_n)}$ as

$$\frac{\partial \mathbf{R}_{PP}^{\cup}(z_n)\big|_{ij}}{\partial c_\alpha(x_i, z_n)} \approx \sum_{\kappa=0}^{K}\sum_{\lambda=0}^{\Lambda}\frac{\partial\left(\tilde{\mathbf{R}}_{PP}^{\cup}\right)_\lambda^\kappa(z_n)\big|_{ii}}{\partial c_\alpha(x_i, z_n)}\delta_{ij}\,\mathbf{S}_\theta^\kappa(z_n)\big|_{ij}, \tag{3.62}$$

with

$$\frac{\partial \left(\tilde{\mathbf{R}}^{\cup}_{PP}\right)^{\kappa}_{\lambda}(z_n)\big|_{ii}}{\partial c_\alpha(x_i,z_n)} = \sum_{m=1}^{\lambda}\sum_{k=0}^{\lambda-m}\frac{m}{\kappa!m!k!(\lambda-k-m)!}\frac{d^{\kappa+\lambda}R^{\cup}_{PP}}{d(\sin(\theta))^{\kappa}dc_\alpha^m dc_\beta^k dc_\rho^{(\lambda-k-m)}}\bigg|_{(\mathbf{0})} c_\alpha^{m-1}c_\beta^k c_\rho^{(\lambda-k-m)}, \quad (3.63)$$

3

where we have omitted the (x_i,z_n) dependency for ease of legibility. In a similar way, we can find the derivatives of the other reflection and transmission operators.

We now examine the derivative of the full objective function with respect to the contrast $c_\alpha(x_i,z_n)$. Combining equations 3.50, 3.53, 3.58 and 3.59, and once again limiting our analysis to the first term of equation 3.53, yields

$$\begin{aligned}\frac{\partial J\left(R^{\cup}\right)}{\partial c_\alpha(x_i,z_n)} = -\mathrm{Re}\Bigg(&\sum_{j=1}^{N_x}\bar{\mathbf{W}}^{-}_{PP}(z_0,z_n)\big|^{*}_{ji}\,e_P(x_j)\frac{\partial \tilde{q}_P^{-,M}(x_i,z_n)^*}{\partial c_\alpha(x_i,z_n)}\\ &+\bar{\mathbf{W}}^{-}_{PS}(z_0,z_n)\big|^{*}_{ji}\,e_P(x_j)\frac{\partial \tilde{q}_S^{-,M}(x_i,z_n)^*}{\partial c_\alpha(x_i,z_n)}\\ &+\bar{\mathbf{W}}^{-}_{SP}(z_0,z_n)\big|^{*}_{ji}\,e_S(x_j)\frac{\partial \tilde{q}_P^{-,M}(x_i,z_n)^*}{\partial c_\alpha(x_i,z_n)}\\ &+\bar{\mathbf{W}}^{-}_{SS}(z_0,z_n)\big|^{*}_{ji}\,e_S(x_j)\frac{\partial \tilde{q}_S^{-,M}(x_i,z_n)^*}{\partial c_\alpha(x_i,z_n)}\Bigg),\end{aligned} \quad (3.64)$$

where we have used the superscript * to indicate complex conjugation. Note the structure of equation 3.64: the terms $\bar{\mathbf{W}}^{-}_{\dots}(z_0,z_n)\big|^{*}_{ji}e_{P/S}(x_j)$ represent the back-propagation of the data residual at the surface, while the multiplication with $\frac{\partial \tilde{q}^{-,M}_{S/P}(x_i,z_n)^*}{\partial c_\alpha(x_i,z_n)}$ represents the application of the imaging condition at the location (x_i,z_n).

We now consider the update direction for all points x_i at depth level z_n. We first define a vector $\Delta\mathbf{c}^{R^{\cup}}_{\alpha}(z_n)$, with elements

$$\Delta\mathbf{c}^{R^{\cup}}_{\alpha}(z_n)\Big|_i = -\frac{\partial J\left(R^{\cup}\right)}{\partial c_\alpha(x_i,z_n)}. \quad (3.65)$$

Using equation 3.64, we write the vector $\Delta\mathbf{c}^{R^{\cup}}_{\alpha}(z_n)$ as

$$\begin{aligned}\Delta\mathbf{c}^{R^{\cup}}_{\alpha}(z_n) = \mathrm{Re}\Big[&\left(\bar{\mathbf{W}}^{-}_{PP}{}^{H}\mathbf{e}_P+\bar{\mathbf{W}}^{-}_{SP}{}^{H}\mathbf{e}_S\right)\circ\left(\left(\partial_{c_\alpha}\mathbf{R}^{\cup}_{PP}\right)\mathbf{p}_P^{+,M}+\left(\partial_{c_\alpha}\mathbf{R}^{\cup}_{PS}\right)\mathbf{p}_S^{+,M}\right)^*\\ &+\left(\bar{\mathbf{W}}^{-}_{PS}{}^{H}\mathbf{e}_P+\bar{\mathbf{W}}^{-}_{SS}{}^{H}\mathbf{e}_S\right)\circ\left(\left(\partial_{c_\alpha}\mathbf{R}^{\cup}_{SP}\right)\mathbf{p}_P^{+,M}+\left(\partial_{c_\alpha}\mathbf{R}^{\cup}_{SS}\right)\mathbf{p}_S^{+,M}\right)^*\Big],\end{aligned} \quad (3.66)$$

where we have used the symbol $\circ$ to denote element wise multiplication and H to denote the conjugate transpose. Note that we have dropped the dependence on the depth level z_n for ease of legibility. Also note the notation ∂_{c_α} to indicate

differentiation with respect to c_α, where $\partial_{c_\alpha}\mathbf{R}^{\cup}_{PP}$ is a matrix of size $N_x \times N_x$ with elements

$$\partial_{c_\alpha}\mathbf{R}^{\cup}_{PP}\big|_{ij} = \frac{\partial \mathbf{R}^{\cup}_{PP}(z_n)\big|_{ij}}{\partial c_\alpha(x_i, z_n)}. \tag{3.67}$$

Extending the approach described above to the other terms of equation 3.53, we write the full update direction of the contrast c_α as a vector $\Delta\mathbf{c}_\alpha(z_n)$, viz.

$$\Delta\mathbf{c}_\alpha(z_n) = \sum_\omega \sum_s \left[\Delta\mathbf{c}_\alpha^{R^{\cup}}(z_n) + \Delta\mathbf{c}_\alpha^{R^{\cap}}(z_n) + \Delta\mathbf{c}_\alpha^{T^{+}}(z_n) + \Delta\mathbf{c}_\alpha^{T^{-}}(z_n)\right]. \tag{3.68}$$

Given the update direction of equation 3.68, we now examine the amplitude of the update. We again limit our analysis to the first term of equation 3.53. Using the fact that $\mathbf{R}^{\cup}$ depends linearly on the contrasts gives

$$\Delta\mathbf{p}^{-,M}\left(R^{\cup}\right) = \bar{\mathbf{W}}^{-}\left(\Delta\mathbf{c}_\alpha \circ \partial_{c_\alpha}\mathbf{R}^{\cup} + \Delta\mathbf{c}_\beta \circ \partial_{c_\beta}\mathbf{R}^{\cup} + \Delta\mathbf{c}_\rho \circ \partial_{c_\rho}\mathbf{R}^{\cup}\right)\mathbf{p}^{+,M}, \tag{3.69}$$

where we have not written the z_n dependence explicitly for ease of legibility.

Extending equation 3.69 to include the other terms of equation 3.53, we find

$$\begin{aligned}\Delta\mathbf{p}^{-,M}(z_0) = \sum_{n=1}^{N_z} &\Delta\mathbf{p}^{-,M}\left(z_0; z_n, R^{\cup}\right) + \Delta\mathbf{p}^{-,M}\left(z_0; z_n, R^{\cap}\right) \\ &+ \Delta\mathbf{p}^{-,M}\left(z_0; z_n, T^{+}\right) + \Delta\mathbf{p}^{-,M}\left(z_0; z_n, T^{-}\right),\end{aligned} \tag{3.70}$$

with $\Delta\mathbf{p}^{-,M}(z_0)$ the total change in the wavefields at the surface due to the change in the contrast parameters at all depth levels. We now take the size of the update as

$$\gamma = \frac{\sum_\omega \sum_s \mathrm{Re}\left(\Delta\mathbf{p}^{-,M}(z_0)^* \cdot \mathbf{e}\right)}{\sum_\omega \sum_s \left\|\Delta\mathbf{p}^{-,M}(z_0)\right\|^2}, \tag{3.71}$$

where $\cdot$ denotes the vector inner product. Finally, we update the contrast parameters

$$c_\alpha^{new}(x_i, z_n) = c_\alpha^{old}(x_i, z_n) + \gamma\Delta c_\alpha(x_i, z_n), \tag{3.72}$$

with similar definitions for the c_β and c_ρ terms.

The full procedure used to find the gradient can be implemented in a straightforward manner, shown in algorithm 4, analogous to the procedure for wavefield modelling illustrated in algorithm 3.

3.3. RESULTS

In this section, we show the results of applying algorithm 4 on two synthetic models. First, we examine a flat, layered model, which will serve as a proof-of-concept and allows us to explore the properties of the inversion results generated by the method. Second, we examine a model featuring a lens-shaped inclusion with a large contrast with respect to the surroundings. This model represents a simplified version of a salt

Algorithm 4: Calculating gradients

Result: $\Delta\mathbf{c}_\alpha(z_n)$, $\Delta\mathbf{c}_\beta(z_n)$ and $\Delta\mathbf{c}_\rho(z_n)$ for all z_n.
Input: $\mathbf{p}^{+,M}(z_n)$ and $\mathbf{p}^{-,M}(z_n)$ for all z_n.

Set $\bar{\mathbf{W}}^{-}(z_0, z_1) = \mathbf{W}(z_0, z_1)$;
for $n = 1 : N_z - 1$ **do**
  for $\mathbf{c} \in \{\mathbf{c}_\alpha, \mathbf{c}_\beta, \mathbf{c}_\rho\}$ **do**
    Calculate $\Delta\mathbf{c}^{R^{\cup}}(z_n)$ and $\Delta\mathbf{c}^{T^{-}}(z_n)$;
    $\Delta\mathbf{c}(z_n) = \Delta\mathbf{c}^{R^{\cup}}(z_n) + \Delta\mathbf{c}^{T^{-}}(z_n)$;
  end
  $\bar{\mathbf{W}}^{-}(z_0, z_{n+1}) = \bar{\mathbf{W}}^{-}(z_0, z_n)\,\mathbf{T}^{-}(z_n)\,\mathbf{W}(z_n, z_{n+1})$;
end
Set $\bar{\mathbf{W}}^{\cup}(z_0, z_{N_z}) = \mathbf{0}$;
for $n = N_z - 1{:}1$ **do**
  $\bar{\mathbf{W}}^{\cup}(z_0, z_n) =$
  $\bar{\mathbf{W}}^{\cup}(z_0, z_{n+1})\,\mathbf{T}^{+}(z_{n+1})\,\mathbf{W}(z_{n+1}, z_n) + \bar{\mathbf{W}}^{-}(z_0, z_{n+1})\,\mathbf{R}^{\cup}(z_{n+1})\,\mathbf{W}(z_{n+1}, z_n)$;
  for $\mathbf{c} \in \{\mathbf{c}_\alpha, \mathbf{c}_\beta, \mathbf{c}_\rho\}$ **do**
    Calculate $\Delta\mathbf{c}^{R^{\cap}}(z_n)$ and $\Delta\mathbf{c}^{T^{+}}(z_n)$;
    $\Delta\mathbf{c}(z_n) = \Delta\mathbf{c}(z_n) + \Delta\mathbf{c}^{R^{\cap}}(z_n) + \Delta\mathbf{c}^{T^{+}}(z_n)$;
  end
end

body in the subsurface, which is a situation which is difficult to image properly if converted waves are not taken into account.

3.3.1. FLAT LAYERED MODEL

We begin our analysis with a simple, flat, layered model, based on the model used by Wu et al. [21]. This model will serve as a toy model, which is used to benchmark the proposed method. It has been constructed such that the S-wave velocity β in the middle layer is close to the P-wave velocity α in the surrounding layers, as shown in figures 3.2a)-3.2c), which represents the case of a salt body within the subsurface.

Synthetic data was generated for the aforementioned model using 61 P-wave sources evenly spaced along the surface. The source wavelet used was a Ricker wavelet with a peak frequency of 17 Hz. Both P- and S-wave data was recorded with 301 receivers with a receiver spacing of 10 metres. To avoid an inverse crime scenario, elastic Kennett modelling [22] was used to generate the synthetic data. This data was then filtered in the spatial Fourier domain to remove post-critical effects, as we know that the extended Shuey approximations used for the reflection and transmission operators only hold up to the critical angle. Migration was then performed on the synthetic data using algorithm 4, with a smoothed version of the true velocity models used for the propagation velocities. Forward and inverse modelling was performed on a grid of 301 by 151 points, with a lateral spacing of 10 metres and a vertical spacing of 5 metres. For the extended Shuey approximations,

Taylor expansions up to $K = 6$ and $\Lambda = 2$ were used. The results of this process are shown in figures 3.2 and 3.3.

We now analyze these results, starting with figure 3.2, which show the true P-wave velocity contrast c_α, S-wave velocity contrast c_β and density contrast c_ρ, along with the inverted contrasts after 10 iterations. We begin our analysis with the reconstructed S-wave velocity contrast c_β, shown in figure 3.2e), which we see matches the ground truth quite closely, with both reflectors clearly identifiable. The reconstructed density contrast c_ρ, shown in figure 3.2f), also clearly shows both reflectors, but contains some smearing above the top reflector. Finally, the reconstructed P-wave velocity contrast c_α, shown in figure 3.2d), struggles in this case, with the two reflectors not being clearly visible.

For a more detailed analysis, we examine vertical profiles taken through the centre of figures 3.2d) - 3.2f), which are shown in figures 3.2g) - 3.2i). From these figures, we see a similar pattern. Once again, we see that the results for c_β match the (band-limited) ground truth quite well. The result for c_ρ introduces additional smearing, and also clearly overestimates the strength of the contrast. Finally, the result for c_α does not accurately reproduce the two reflectors.

To explore the reasons behind the lack of accuracy in the results for c_ρ and c_α, we examine the cross-talk between the different parameters. We begin by investigating $\left(\tilde{R}^{\cup}_{PP}\right)^0_1$, the lowest-order component of the PP-reflectivity, which is given by

$$\left(\tilde{R}^{\cup}_{PP}\right)^0_1 = \frac{1}{2}\left(c_\alpha + c_\rho\right). \tag{3.73}$$

From this expression, we see that there is strong cross-talk between the c_α and c_ρ terms for near-zero angles of incidence. In the same vein, we examine $\left(\tilde{R}^{\cup}_{SP}\right)^1_1$, the lowest-order component of the SP-reflectivity, which is given by

$$\left(\tilde{R}^{\cup}_{SP}\right)^1_1 = -\left(\hat{V}\left(c_\rho + 2c_\beta\right) + \frac{1}{2}c_\rho\right), \tag{3.74}$$

where $\hat{V} = \beta/\alpha$. From this expression, we see that there is also cross-talk between the c_β and c_ρ terms. This cross-talk between separate contrasts may explain why the density contrast c_ρ is overestimated, while the P-wave velocity contrast c_α is simultaneously underestimated. A possible approach to reduce this cross-talk is to apply some form of preconditioning, such as preconditioning the gradient with the inverse of the Hessian [23].

To complete our analysis of the flat, layered example we examine a shot record, seen in figure 3.3. Note the strong converted wave response in the P-wave data shown in figure 3.3a), visible below the primary PP-reflection from the 'base-salt'. From figure 3.3d) we see that this converted wave response is due to $PPSP$ and $PSPP$ wave paths in the medium, as the $PSSS$ response is very small. Examining figures 3.3b) and 3.3e), we see that the method has generally been able to capture much of the converted wave response. This is confirmed by the residuals, shown in figures 3.3c) and 3.3f).

3.3.2. LENS-SHAPED INCLUSION MODEL

In this section we will examine a so-called lens-shaped inclusion model, with a lens with a large contrast in the centre of the model and a number of flat layers beneath it. In the same way as for the flat, layered model, the parameters of the lens have been chosen such that the S-wave velocity inside the lens matches the P-wave velocity outside the lens, representing a high-contrast salt body.

To generate data for the aforementioned model, finite-difference time-domain modelling was used [24]. In total, 61 sources were used with a source spacing of 50 metres, together with 301 receivers with a receiver spacing of 10 metres. The source wavelet employed was a Ricker wavelet with a peak frequency of 17 Hz. Once again, post-critical effects were filtered from the data in the spatial Fourier domain. Next, elastic FWM was applied on the synthetic data, using a grid of 301 by 381 points, with a grid spacing of 10 metres in the lateral direction and 5 metres in the vertical direction. For the extended Shuey approximations, Taylor expansions up to $K = 8$ and $\Lambda = 2$ were used. The ground-truth contrasts, as well as the inversion results after 5 iterations, are shown in figure 3.4.

Examining the inverted contrasts, we see many of the same effects as those we observed for the flat, layered model in the previous section. Once again starting with the S-wave velocity contrast c_β, shown in figure 3.4e), we see that the lens has been recovered well in this case. However, the deeper reflectors are not well resolved. This is probably due to the fact that these deeper reflectors are only illuminated by small angles of incidence, which are not sensitive to the S-wave velocity contrast c_β, making it difficult to reconstruct properly.

Continuing our analysis, we examine the density contrast c_ρ, shown in figure 3.4f). Once again, we notice that the density contrast has been overestimated in this case, similar to the results of the flat model, shown in 3.2f). We also notice additional smearing above the top reflector in this case. The P-wave velocity contrast c_α, shown in figure 3.4d), also shows similar results. Most noticeably, the top part of the lens is not reconstructed well in this case, while the deeper layers are recovered accurately. These observations are further confirmed by examining slices through the centre of figures 3.4d) - 3.4f), shown in figures 3.4g) - 3.4i). Once again, it appears that cross-talk between the different contrasts has made it difficult to accurately recover the separate contrasts in this case.

Finally, we examine a shot record for the lens inclusion model, shown in figure 3.5. Comparing the forward modelled wavefields, shown in figures 3.5b) and 3.5e), to the finite-difference data shown in figures 3.5a) and 3.5d), we see that the method explains the data reasonably well. However, the residuals, shown in figures 3.5c) and 3.5f), are clearly larger than those achieved for the flat model, shown in figures 3.3c) and 3.3f). This increased residual is probably caused by inaccuracies in the modelling of the dipping reflectors, which are difficult to model accurately when using one-way operators.

3.4. DISCUSSION

In this section we will discuss some additional aspects regarding the elastic FWM method presented in this paper. First, we compare the results shown in section 3.3 to the results of the conventional, acoustic FWM method for the same models. Next, we examine the case where no S-wave data is available, such as in a marine setting. Finally, we discuss a number of potential extensions of the elastic FWM method.

3.4.1. COMPARISON TO ACOUSTIC FWM

We begin by comparing the results for the elastic FWM algorithm with the conventional, angle-independent, acoustic FWM algorithm. In the acoustic FWM algorithm, the quantity of interest for inversion is the impedance contrast c_Z, which is defined as

$$c_Z = \frac{1}{2}\left(c_\alpha + c_\rho\right). \tag{3.75}$$

Therefore, in order to compare the reconstructions of the acoustic and elastic FWM methods fairly, we will compare the acoustic FWM image to the average of the reconstructed P-wave velocity and density contrasts. Note that this comparison does not take into account the fact that the elastic FWM algorithm provides additional information by separating the contrasts, thus giving more insight into the underlying medium properties.

We begin by comparing the elastic and acoustic FWM results for the flat model described in section 3.3.1. The reconstructed impedance contrasts are shown in figure 3.6. Comparing figures 3.6a) and 3.6b), we immediately notice that the acoustic FWM algorithm is not able to reconstruct the reflectors properly in this case. Most noticeably, the acoustic FWM image has flipped the sign of the reflectors. This is easily explained by examining the shot records, shown in figure 3.7. Examining the true P-wave data, shown in figure 3.7a), we notice that the reflectivity goes from positive to negative at offsets away from zero incidence. As the acoustic FWM algorithm assumes the reflectivity to be angle-independent, it is unable to account for this effect, leading to it estimating the reflectivity with the wrong sign. Note that this is a rather extreme case, as the change in reflectivity at different angles is usually less strong.

Examining a slice through the middle of figures 3.6a) and 3.6b), shown in figure 3.6d), we see this effect more clearly. From this figure, we also see that, while the elastic FWM result introduces some smearing for depths above the first reflector, the overall result for elastic FWM is more consistent. Specifically, the two reflectors are clearly recovered, with no spurious reflectors introduced below the bottom reflector. The acoustic FWM image, on the other hand, does not recover the two reflectors well, and is less consistent for areas below the top reflector. Note that the smearing present in the elastic FWM result can be easily removed by filtering out the lowest spatial frequencies present in the image.

Next, we compare the modelled P-wave data for elastic FWM, shown in figure 3.7b), and acoustic FWM, shown in figure 3.7e). Comparing these figures, we see that the modelled wavefield for elastic FWM is more consistent than that of acoustic FWM. Most noticeably, the wavefield recovered by elastic FWM captures

wave-conversion effects accurately, while the acoustic method is unable to take these effects into account. This leads to a significantly larger data residual when using acoustic FWM, as is shown in figure 3.7f).

Finally, we compare the elastic and acoustic FWM results for the lens-shaped inclusion model, described in section 3.3.2. The results for this comparison are shown in figure 3.8. Comparing figures 3.8a) and 3.8b), we notice that the acoustic FWM algorithm is unable to reconstruct the top of the lens-shaped inclusion properly, which the elastic FWM algorithm is able to do. This is confirmed by figure 3.8d), which shows that the top of the lens is recovered well in elastic FWM while being absent in the acoustic result. While the elastic FWM method does introduce additional smearing above the top reflector, this can once again be removed by filtering the final result.

3.4.2. MISSING *S*-WAVE DATA

In this section, we examine the results of the elastic FWM algorithm in cases where only *P*-wave data is available. This situation corresponds to a marine acquisition scenario, for example, where no *S*-waves can be recorded.

We begin by examining the results for the flat model of section 3.3.1, which are shown in figure 3.9. Examining the reconstructed contrasts, shown in figures 3.9d) - 3.9f), we notice a number of differences compared to the reconstructed contrasts when *S*-wave data is available, shown in figures 3.2d) - 3.2f). Most noticeably, we see that the *S*-wave velocity contrast c_β is significantly less well recovered when no *S*-wave data is available. This is to be expected, as the *SP*-reflection coefficient depends much more strongly on c_β than the *PP*-reflection coefficient. In cases where there is no *S*-wave data available, therefore, the objective function J does not depend as strongly on c_β. This makes it more difficult to recover accurately. The other contrasts, however, are comparable with the results when *S*-wave data is available.

Next, we examine the results for the lens-shaped inclusion model of section 3.3.2, which are shown in figure 3.10. Once again, we compare figures 3.10d) - 3.10f) with figures 3.4d) - 3.4f). In this case, we once again notice that the *S*-wave velocity contrast is significantly less well recovered when no *S*-wave data is available. However, once again we notice that the results for the density contrast and the *P*-wave velocity contrast are comparable to the case where *S*-wave data is available. This indicates that the elastic FWM algorithm can be used successfully in marine cases, where no direct *S*-wave data is available.

3.4.3. POSSIBLE EXTENSIONS

Finally, in this section, we examine a number of possible extensions to the elastic FWM algorithm presented in this paper. We begin by examining the local dip θ_0, which we have assumed to be known in section 3.2.3. In cases where the local dip is not known a priori, one can begin by using a conventional, acoustic imaging technique, such as angle-independent acoustic FWM, to generate an initial model of the reflectivity. By applying a local dip estimation scheme on this preliminary image,

one can find an estimate of the local dip, which can be used as an input for the method presented here. In the case of the lens model presented in section 3.3.2, the local dip was estimated by applying a dip estimation scheme on the ground-truth reflectors, capping the maximal dip angle at 30 degrees.

Alternatively, one can estimate the local dip directly from the reflection operators, by extending the inversion process described in section 3.2.4 to include the local dip angle. To do this, one requires the derivative of the objective function J with respect to $\theta_0(x_i, z_n)$. Summarizing the analysis of section 3.2.4, we find that this derivative is proportional to the derivative of the reflection and transmission operators. Examining the PP-reflection operator, we find

$$\frac{\partial \mathbf{R}^{\cup}_{PP}(z_n)\big|_{ij}}{\partial \theta_0(x_i, z_n)} \approx \sum_{\kappa=0}^{K} \sum_{\kappa'=0}^{K} \sum_{\lambda=0}^{\Lambda} \left(\tilde{\mathbf{R}}^{\cup}_{PP}\right)^{\kappa'}_{\lambda}(z_n)\Big|_{ij} \frac{\partial \mathbf{S}^{\kappa'}_{\kappa}(\theta_0)\Big|_{ii}}{\partial \theta_0(x_i, z_n)} \delta_{ij} \mathbf{S}^{\kappa}_{\theta}(z_n)\big|_{ij}, \tag{3.76}$$

which can be straightforwardly evaluated using mathematical software. Using these derivatives, the local dip can be updated at each iteration in a similar way to the contrasts. In this manner, the estimation of the local dip can be integrated into the elastic FWM framework with little additional effort.

Secondly, while the results presented in this paper have been achieved in the 2D case, the method can also be extended to 3D applications, in a similar way as the conventional, acoustic FWM method [9]. In the 3D case, the one-dimensional convolutions of the 2D method need to be replaced with two-dimensional convolutions to account for the propagation and scattering in three dimensions. An additional challenge for elastic FWM is that it is necessary to take S_H waves into account as well as the S_V waves that we have discussed in this paper. In principle, these waves can be taken into account using the same framework as presented here. However this will introduce additional complexity into the presented algorithm, and is outside the scope of this paper.

Finally, the elastic FWM algorithm presented here can be incorporated into a joint reflectivity and velocity estimation algorithm, such as Joint Migration Inversion (JMI) [8, 25] or one-way Reflection Waveform Inversion (ORWI) [26]. In conventional, acoustic JMI it is difficult to incorporate angle-dependent reflectivity, as estimating both the angle-dependent reflectivity and the velocity model simultaneously leads to overparametrisation [27]. However, by using the extended Shuey's approximations of section 3.2.3, the number of parameters required to estimate the angle-dependent reflectivity is significantly reduced. This could potentially allow one to estimate both angle-dependent reflectivity along with velocity simultaneously. By further extending the acoustic JMI algorithm to also include S-wave velocity estimation, an elastic JMI algorithm, which takes converted waves into account, could finally be developed.

3.5. CONCLUSIONS

In conventional, acoustic Full Wavefield Migration, we neglect wave conversions from P- to S-waves, as well as the propagation of S-waves throughout the medium. In this paper, we have presented an extension to the acoustic FWM algorithm which

takes these effects into account using an extended version of Shuey's approximation.

Our main conclusion, based on the results we have presented, is that elastic FWM outperforms acoustic FWM in cases with large contrasts, where strong AVO and wave-conversion effects are present. While the reconstructed contrasts are not perfect, they are an improvement compared to the acoustic FWM results for the same areas. Therefore, we conclude that elastic FWM serves as an effective extension of acoustic FWM for these situations and can serve to improve the resulting images in areas with strong converted waves.

Furthermore, we show that the method can still produce accurate results in cases where *S*-wave data is not available, such as in marine settings. This makes the method more widely applicable. We also present several possible areas where the method can be extended, which can serve to further increase the potential of the method.

3.6. ACKNOWLEDGMENTS

The authors thank the sponsoring companies from the Delphi Consortium at Delft University of Technology for their support to this research.

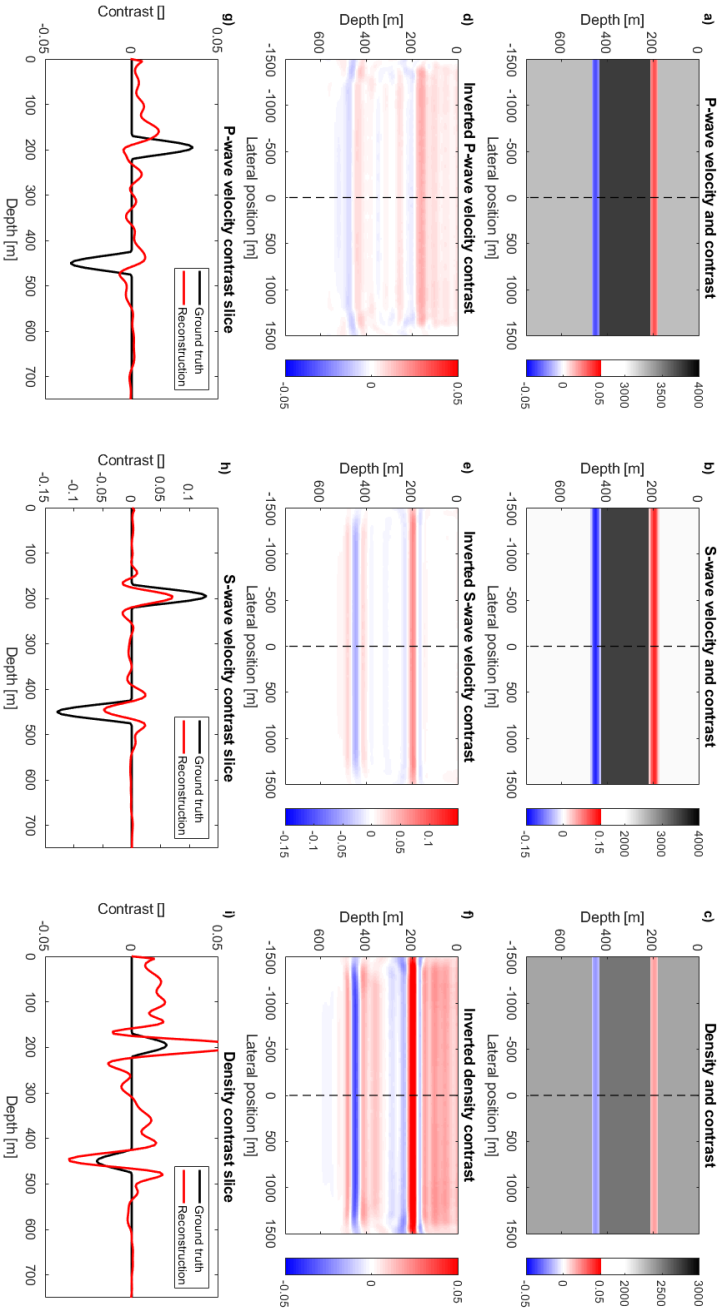

Figure 3.2: Results of elastic FWM for the flat, layered model. The ground-truth P-wave velocity, S-wave velocity and density, along with their contrasts, are shown in figure (a), (b) and (c), respectively. The reconstructed P-wave velocity, S-wave velocity and density contrasts after 10 iterations are shown in figure (d), (e) and (f), respectively. Finally, the ground-truth P-wave velocity, S-wave velocity and density contrasts at $x = 0$ (black lines), as well as the reconstructed contrasts (red lines), are shown in figure (g), (h) and (i), respectively.

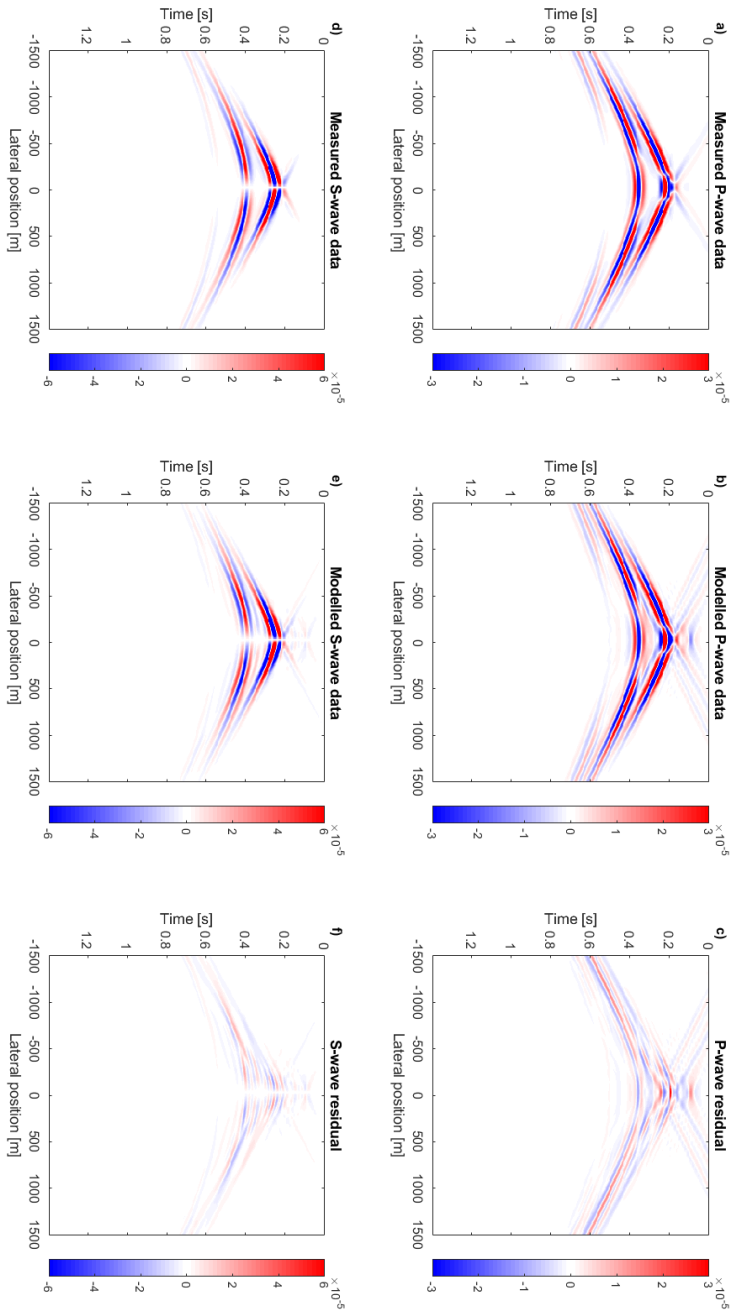

Figure 3.3: Shot records for the flat, layered model. The synthetic *P*- and *S*-wave data, generated by elastic Kennett modelling, are shown in figure (a) and (d), respectively. The forward modelled *P*- and *S*-wave data after 10 iterations is shown in figure (b) and (e), respectively. Finally, the difference between the synthetic *P*- and *S*-wave data and the forward modelled data is shown in figure (c) and (f), respectively. Note that all values have been clipped at 30% of the maximum value.

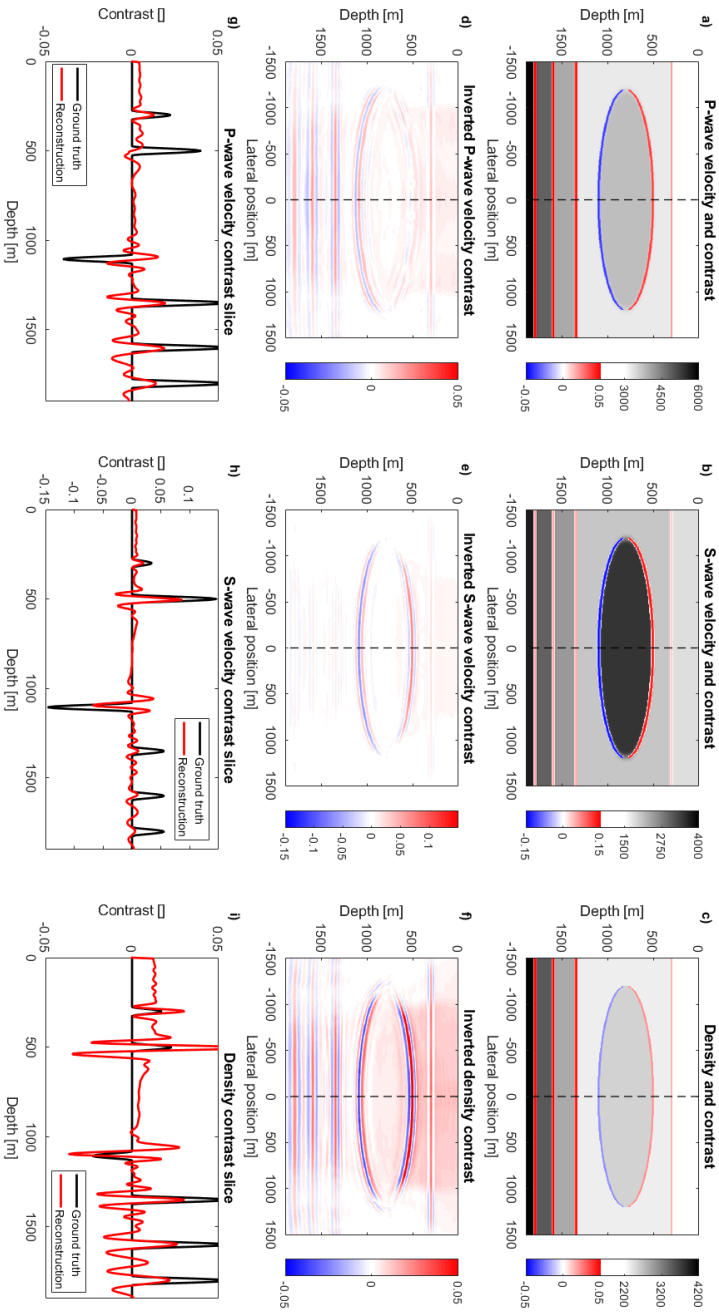

Figure 3.4: Results of elastic FWM for the lens-shaped inclusion model. The ground-truth P-wave velocity, S-wave velocity and density, along with their contrasts, are shown in figure (a), (b) and (c), respectively. The reconstructed P-wave velocity, S-wave velocity and density contrasts after 5 iterations are shown in figure (d), (e) and (f), respectively. Finally, the ground-truth P-wave velocity, S-wave velocity and density contrasts at $x = 0$ (black lines), as well as the reconstructed contrasts (red lines), are shown in figure (g), (h) and (i), respectively.

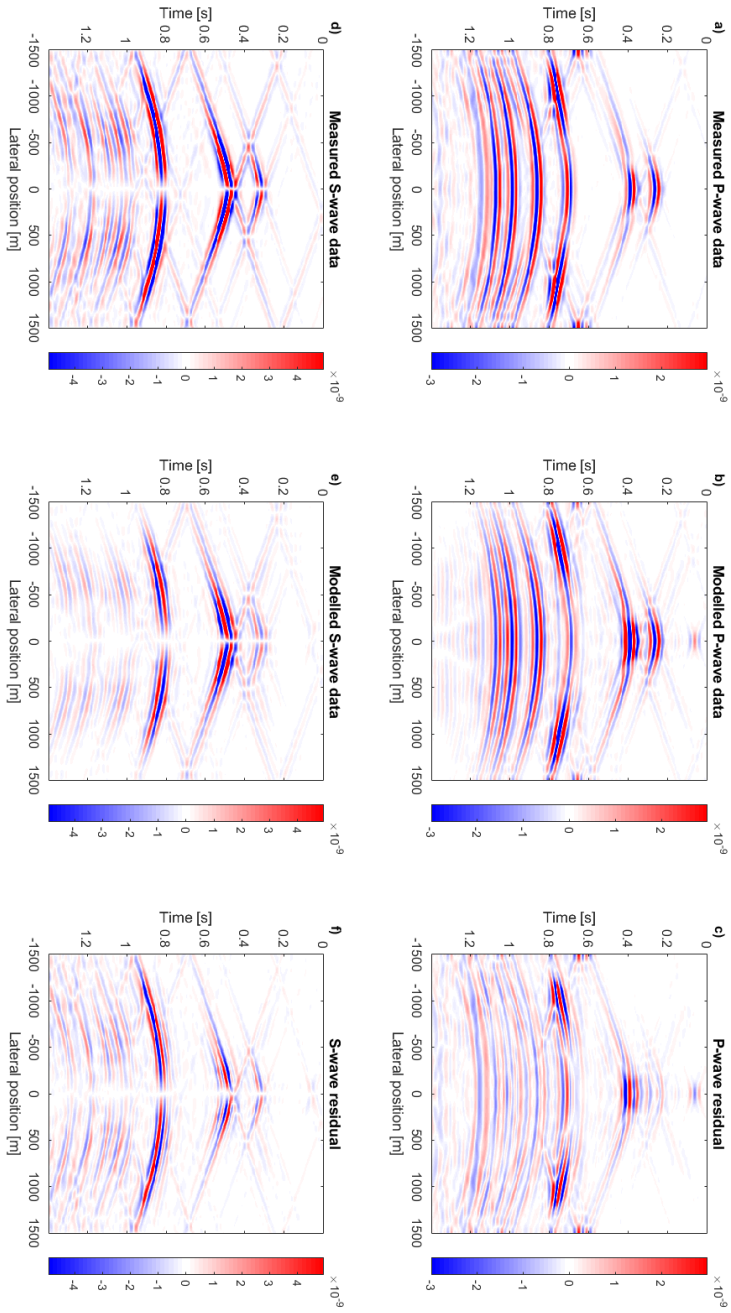

Figure 3.5: Shot records for the lens-shaped inclusion model. The synthetic *P*- and *S*-wave data, generated by elastic, time-domain finite-difference modelling, are shown in figure (a) and (d), respectively. The forward modelled *P*- and *S*-wave data after 5 iterations is shown in figure (b) and (e), respectively. Finally, the difference between the synthetic *P*- and *S*-wave data and the forward modelled data is shown in figure (c) and (f), respectively. Note that all values have been clipped at 30% of the maximum value.

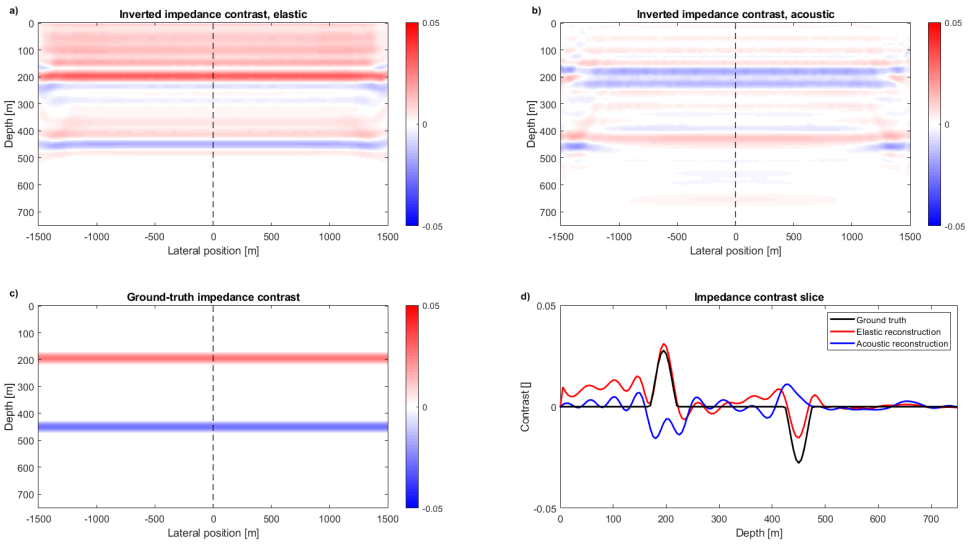

Figure 3.6: Comparison of elastic FWM and acoustic FWM for the flat, layered model. The reconstructed impedance contrast generated by elastic FWM and acoustic FWM after 10 iterations are shown in figure (a) and (b), respectively. The ground-truth impedance contrast is shown in figure (c). Finally, a slice through figures (a) - (c) is shown in figure (d), showing the ground-truth impedance contrast (black line), the elastic FWM result (red line) and the acoustic FWM result (blue line).

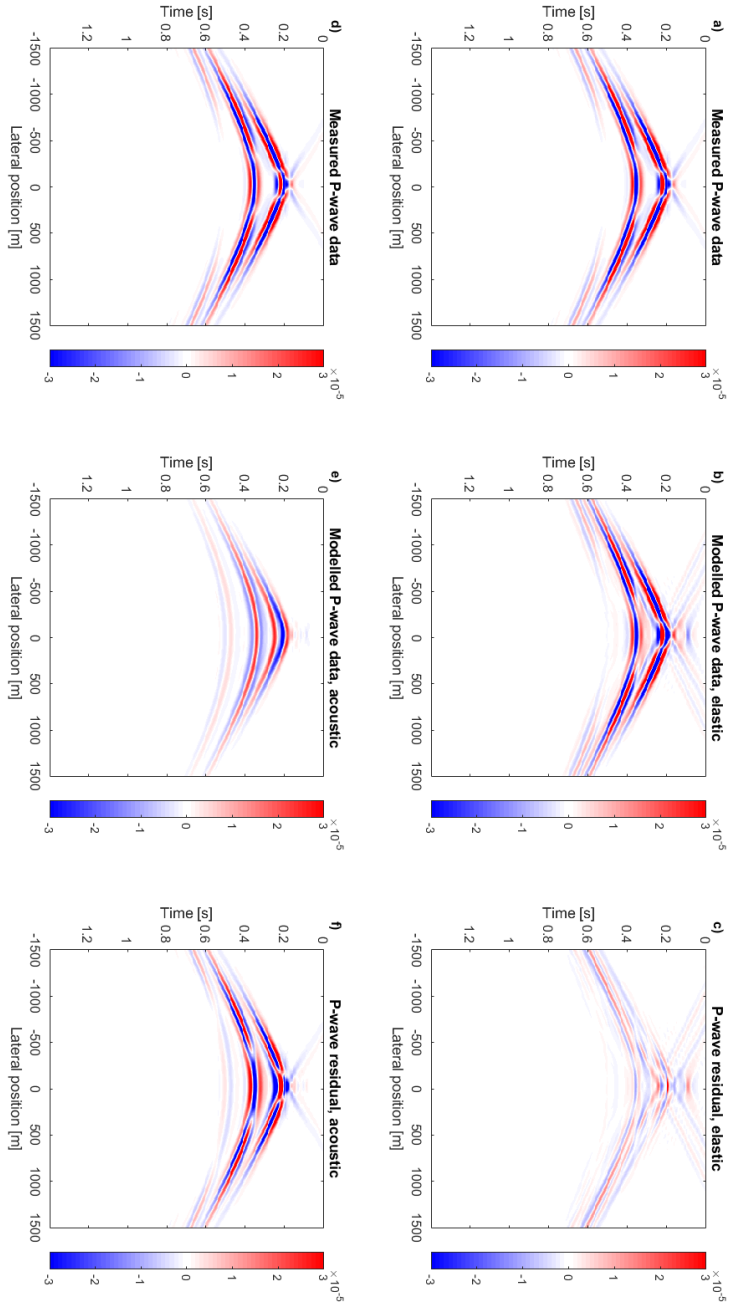

Figure 3.7: Shot records for the flat, layered model. The synthetic *P*-wave data, generated by elastic Kennett modelling, is shown in figure (a) and (d). The forward modelled *P*-wave data for elastic FWM and acoustic FWM after 10 iterations is shown in figure (b) and (e), respectively. Finally, the difference between the synthetic *P*-wave data and the forward modelled data for elastic FWM and acoustic FWM is shown in figure (c) and (f), respectively. Note that all values have been clipped at 30% of the maximum value.

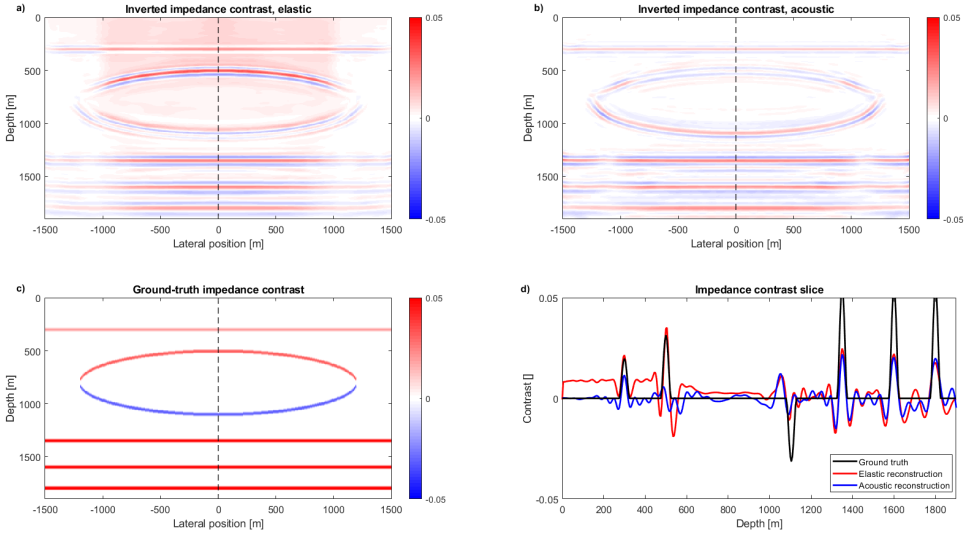

Figure 3.8: Comparison of elastic FWM and acoustic FWM for the lens-shaped inclusion model. The reconstructed impedance contrast generated by elastic FWM and acoustic FWM after 5 iterations are shown in figure (a) and (b), respectively. The ground-truth impedance contrast is shown in figure (c). Finally, a slice through figures (a) - (c) is shown in figure (d), showing the ground-truth impedance contrast (black line), the elastic FWM result (red line) and the acoustic FWM result (blue line).

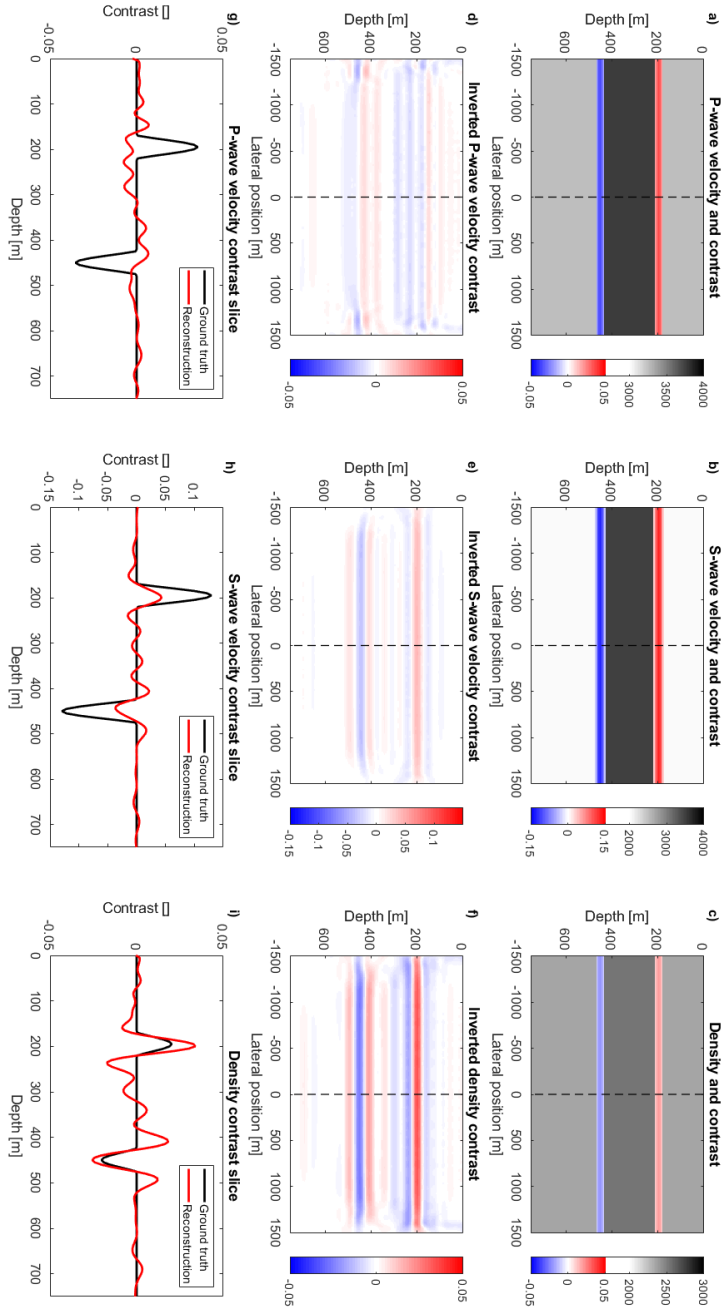

Figure 3.9: Results of elastic FWM for the flat, layered model when no S-wave data is available. The ground-truth P-wave velocity, S-wave velocity and density, along with their contrasts, are shown in figure (a), (b) and (c), respectively. The reconstructed P-wave velocity, S-wave velocity and density contrasts after 10 iterations are shown in figure (d), (e) and (f), respectively. Finally, the ground-truth P-wave velocity, S-wave velocity and density contrasts at $x = 0$ (black lines), as well as the reconstructed contrasts (red lines), are shown in figure (g), (h) and (i), respectively.

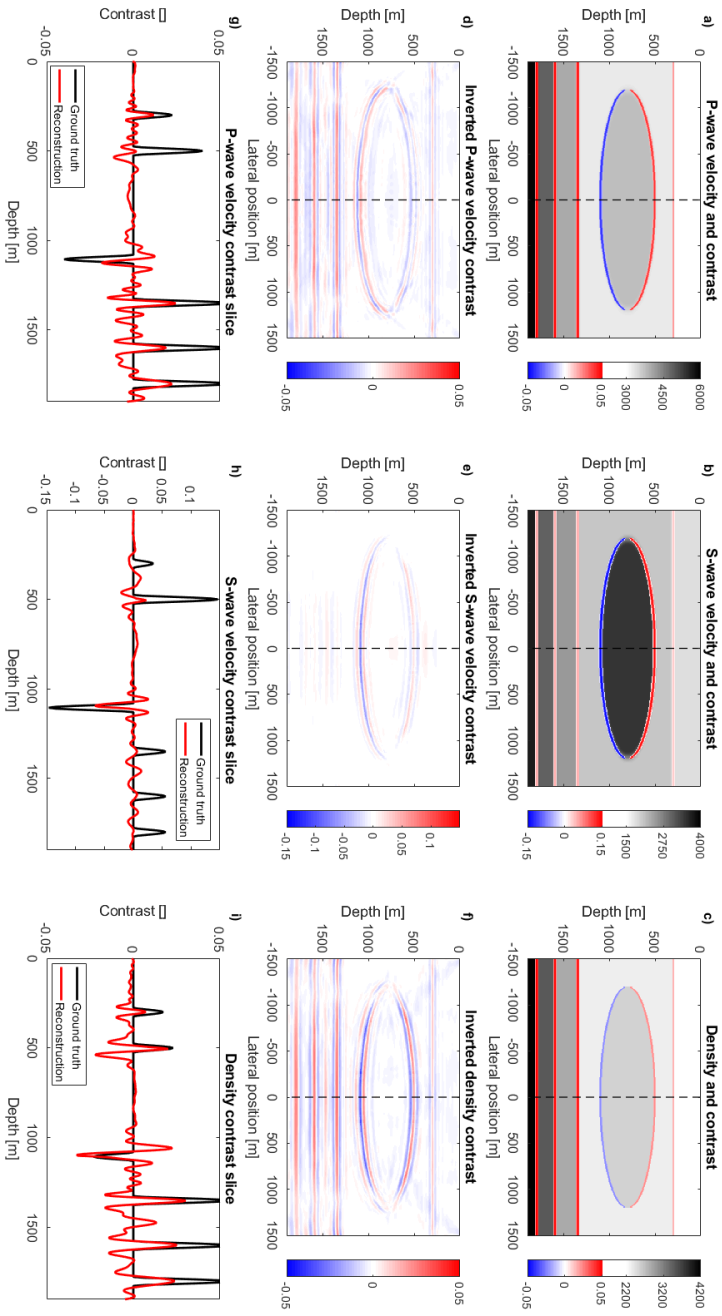

Figure 3.10: Results of elastic FWM for the lens-shaped inclusion model when no S-wave data is available. The ground-truth P-wave velocity, S-wave velocity and density, along with their contrasts, are shown in figure (a), (b) and (c), respectively. The reconstructed P-wave velocity, S-wave velocity and density contrasts after 10 iterations are shown in figure (d), (e) and (f), respectively. Finally, the ground-truth P-wave velocity, S-wave velocity and density contrasts at $x = 0$ (black lines), as well as the reconstructed contrasts (red lines), are shown in figure (g), (h) and (i), respectively.

REFERENCES

[1] R. Alai, F. Liu, E. Verschuur, J. Thorbecke, G. Coskun, S. Dong, C. Macesanu, B. Wang, C. L. Slind, and E. Andersen. “Enhancing subsalt imaging through advanced identification and suppression of interbed multiples and mode-converted reflections — Gulf of Mexico and Brazil case studies”. In: *The Leading Edge* 40.12 (Dec. 2021), pp. 905–913. ISSN: 1938-3789. DOI: 10.1190/tle40120905.1. URL: http://dx.doi.org/10.1190/tle40120905.1.

[2] R. A. Ensley. “Comparison of P- and S-wave seismic data: A new method for detecting gas reservoirs”. In: *GEOPHYSICS* 49.9 (Sept. 1984), pp. 1420–1431. ISSN: 1942-2156. DOI: 10.1190/1.1441771. URL: http://dx.doi.org/10.1190/1.1441771.

[3] I. F. Jones and I. Davison. “Seismic imaging in and around salt bodies: Problems and pitfalls”. In: *SEG Technical Program Expanded Abstracts 2014*. Society of Exploration Geophysicists, Aug. 2014, pp. 3684–3688. DOI: 10.1190/segam2014-0047.1. URL: http://dx.doi.org/10.1190/segam2014-0047.1.

[4] R. Alai, F. Liu, D. Armentrout, D. Brookes, T. Johnson, M. Cvetkovic, G. Coskun, S. Sulaiman, K. K. Lee, A. Mokhtar, C. L. Slind, H. Wahab, W. C. Low, and A. A. B. Hashim. “Improved subsalt imaging in Brazil Campos basin — Cascaded application of hybrid interbed demultiple, P- and S-salt velocity joint migration, and subsalt converted wave suppression”. In: *Second International Meeting for Applied Geoscience & Energy*. Society of Exploration Geophysicists and American Association of Petroleum Geologists, Aug. 2022, pp. 2680–2684. DOI: 10.1190/image2022-3740399.1. URL: http://dx.doi.org/10.1190/image2022-3740399.1.

[5] J. Virieux and S. Operto. “An overview of full-waveform inversion in exploration geophysics”. In: *GEOPHYSICS* 74.6 (Nov. 2009), WCC1–WCC26. ISSN: 1942-2156. DOI: 10.1190/1.3238367. URL: http://dx.doi.org/10.1190/1.3238367.

[6] V. Prieux, R. Brossier, S. Operto, and J. Virieux. “Multiparameter full waveform inversion of multicomponent ocean-bottom-cable data from the Valhall field. Part 2: imaging compressive-wave and shear-wave velocities”. In: *Geophysical Journal International* 194.3 (June 2013), pp. 1665–1681. ISSN: 0956-540X. DOI: 10.1093/gji/ggt178. URL: http://dx.doi.org/10.1093/gji/ggt178.

[7] A. J. Berkhout. “Review Paper: An outlook on the future of seismic imaging, Part II: Full-Wavefield Migration”. In: *Geophysical Prospecting* 62.5 (Aug. 2014b), pp. 931–949. ISSN: 1365-2478. DOI: 10.1111/1365-2478.12154. URL: http://dx.doi.org/10.1111/1365-2478.12154.

[8] X. Staal. “Combined imaging and velocity estimation by Joint Migration Inversion”. PhD thesis. Delft University of Technology, 2015. DOI: 10.4233/UUID:F9CFA765-DAC4-4954-9B6B-01B8C7345018. URL: http://resolver.tudelft.nl/uuid:f9cfa765-dac4-4954-9b6b-01b8c7345018.

[9] M. Davydenko and D. J. Verschuur. “Full-wavefield migration: using surface and internal multiples in imaging”. In: *Geophysical Prospecting* 65.1 (Feb. 2016), pp. 7–21. ISSN: 1365-2478. DOI: 10.1111/1365-2478.12360. URL: http://dx.doi.org/10.1111/1365-2478.12360.

[10] Y. Sun, Y. S. Kim, S. Qu, E. Verschuur, A. Almomin, and R. van Borselen. “Angle-dependent full-wavefield migration based upon full-waveform inversion and joint-migration inversion”. In: *SEG Technical Program Expanded Abstracts 2018*. Society of Exploration Geophysicists, Aug. 2018, pp. 4357–4361. DOI: 10.1190/segam2018-2987449.1. URL: http://dx.doi.org/10.1190/segam2018-2987449.1.

[11] A. J. Berkhout. *Seismic migration: Imaging of Acoustic Energy by Wave Field Extrapolation*. Elsevier, 1984.

[12] A. J. Berkhout. “Review Paper: An outlook on the future of seismic imaging, Part I: forward and reverse modelling”. In: *Geophysical Prospecting* 62.5 (Aug. 2014a), pp. 911–930. ISSN: 1365-2478. DOI: 10.1111/1365-2478.12161. URL: http://dx.doi.org/10.1111/1365-2478.12161.

[13] D. Gisolf and E. Verschuur. *The Principles of Quantitative Acoustical Imaging*. European Association of Geoscientists & Engineers, 2010. URL: https://www.earthdoc.org/content/books/9789462820135.

[14] O. A. V., W. A. S., and N. S. H. *Signals and Systems*. Pearson, 1996.

[15] C. P. A. Wapenaar and J. L. T. Grimbergen. “Reciprocity theorems for one-way wavefields”. In: *Geophysical Journal International* 127.1 (Oct. 1996), pp. 169–177. ISSN: 1365-246X. DOI: 10.1111/j.1365-246x.1996.tb01542.x. URL: http://dx.doi.org/10.1111/j.1365-246X.1996.tb01542.x.

[16] H. Hammad and D. Verschuur. “Generalized Full Wavefield Modeling: Beyond Neumann”. In: *80th EAGE Conference and Exhibition 2018*. Copenhagen2018. EAGE Publications BV, June 2018. DOI: 10.3997/2214-4609.201801102. URL: http://dx.doi.org/10.3997/2214-4609.201801102.

[17] A. Li and X. Liu. “An optimised one-way wave migration method for complex media with arbitrarily varying velocity based on eigen-decomposition”. In: *Journal of Geophysics and Engineering* 18.5 (Oct. 2021), pp. 776–787. ISSN: 1742-2140. DOI: 10.1093/jge/gxab051. URL: http://dx.doi.org/10.1093/jge/gxab051.

[18] R. T. Shuey. “A simplification of the Zoeppritz equations”. In: *GEOPHYSICS* 50.4 (Apr. 1985), pp. 609–614. ISSN: 1942-2156. DOI: 10.1190/1.1441936. URL: http://dx.doi.org/10.1190/1.1441936.

[19] K. Aki and P. Richards. *Quantitative Seismology, 2nd edition*. 2nd ed. Sausalito, CA: University Science Books, Sept. 2002.

[20] S. Fomel. “Applications of plane-wave destruction filters”. In: *GEOPHYSICS* 67.6 (Nov. 2002), pp. 1946–1960. ISSN: 1942-2156. DOI: 10.1190/1.1527095. URL: http://dx.doi.org/10.1190/1.1527095.

[21] Z. Wu, Z. Wei, Z. Zhang, J. Mei, R. Huang, and P. Wang. “Elastic FWI for large impedance contrasts”. In: *Second International Meeting for Applied Geoscience & Energy*. Society of Exploration Geophysicists and American Association of Petroleum Geologists, Aug. 2022, pp. 3686–3690. DOI: 10.1190/image2022-w17-02.1. URL: http://dx.doi.org/10.1190/image2022-w17-02.1.

[22] B. L. N. Kennett. “AN OPERATOR APPROACH TO FORWARD MODELING, DATA PROCESSING AND MIGRATION”. In: *Geophysical Prospecting* 32.6 (Dec. 1984), pp. 1074–1090. ISSN: 1365-2478. DOI: 10.1111/j.1365-2478.1984.tb00755.x. URL: http://dx.doi.org/10.1111/j.1365-2478.1984.tb00755.x.

[23] S. Abolhassani and D. J. Verschuur. “Efficient preconditioned least-squares wave-equation migration”. In: *GEOPHYSICS* 89.3 (Apr. 2024), S275–S288. ISSN: 1942-2156. DOI: 10.1190/geo2023-0048.1. URL: http://dx.doi.org/10.1190/geo2023-0048.1.

[24] J. W. Thorbecke and D. Draganov. “Finite-difference modeling experiments for seismic interferometry”. In: *GEOPHYSICS* 76.6 (Nov. 2011), H1–H18. ISSN: 1942-2156. DOI: 10.1190/geo2010-0039.1. URL: http://dx.doi.org/10.1190/geo2010-0039.1.

[25] A. J. Berkhout. “Review Paper: An outlook on the future of seismic imaging, Part III: Joint Migration Inversion”. In: *Geophysical Prospecting* 62.5 (Aug. 2014c), pp. 950–971. ISSN: 1365-2478. DOI: 10.1111/1365-2478.12158. URL: http://dx.doi.org/10.1111/1365-2478.12158.

[26] S. Abolhassani and E. Verschuur. “High-Resolution One-Way Reflection Waveform Inversion”. In: *84th EAGE Annual Conference & Exhibition*. European Association of Geoscientists & Engineers, 2023, pp. 1–5. DOI: 10.3997/2214-4609.202310517. URL: http://dx.doi.org/10.3997/2214-4609.202310517.

[27] S. Qu. “Simultaneous joint migration inversion as a high-resolution time-lapse imaging method for reservoir monitoring”. PhD thesis. Delft University of Technology, 2020. DOI: 10.4233/UUID:F22C0DA3-9D85-4C3A-9C07-949E242869D6. URL: http://resolver.tudelft.nl/uuid:f22c0da3-9d85-4c3a-9c07-949e242869d6.

4

MODEL-ORDER REDUCED FULL-WAVEFIELD MIGRATION USING PROPER ORTHOGONAL DECOMPOSITION

As seismic migration is increasingly applied to more and more complex media, more sophisticated imaging techniques are required to generate accurate images of the subsurface. Currently, the best results for imaging are achieved by Least-Squares Migration (LSM) methods, such as Least-Squares Reverse Time Migration (LS-RTM) and Full-Wavefield Migration (FWM). These methods iteratively update the image to minimize the misfit between the forward modelled wavefield and the recorded data at the surface. However, a key challenge for these techniques is the speed of convergence. To accelerate the speed of convergence, pre-conditioning is commonly applied. The most common preconditioner is the reciprocal of the Hessian operator. However, this operator is computationally expensive to calculate, making it difficult to apply directly. In this paper, we present a novel, alternative, preconditioner for FWM. This preconditioner is based on applying Galerkin projections to a linear system, which projects the system onto a set of known basis vectors. To find an appropriate set of basis vectors for this approach we apply Proper Orthogonal Decomposition (POD) to a set of partial solutions of the linear system. The resulting method gives an approximation to the pseudo-inverse based on these basis vectors. To test this technique, which we name Model-Order Reduced FWM (MOR-FWM), we apply it to the synthetic Marmousi model as well as to field data from the Vøring basin in Norway. For these examples, we show that MOR-FWM yields an improved data-misfit compared to the standard FWM approach. In addition, we show that the result for the field data case can be improved by normalizing the partial solutions before applying POD.

This chapter has been submitted for publication in ...

4.1. INTRODUCTION

Seismic migration is an important tool for subsurface characterization, which is of vital importance in many different areas. Examples include the study of the Earth's geological structures, the location of subsurface resources and the characterization of potential sites for off-shore wind farms [1], to name a few.

While many different approaches for seismic migration exist [2], the general approach commonly consists of three steps. First, the source wavefield at the surface is propagated forward into the medium through a numerical forward modelling scheme, where an estimate of the, generally unknown, speed-of-sound model is used to ensure accurate propagation. Second, using a similar approach, the measured data at the subsurface is propagated backwards in time into the medium. Finally, the forward and backward propagated wavefields are correlated using an imaging condition, leading to an estimate of the reflectivity model of the subsurface.

To improve upon the standard migration approach, Least-Squares Migration (LSM) methods have been introduced [3, 4]. LSM methods aim to minimize the misfit between the recorded data and forward modelled wavefield at the surface by iteratively updating the reflectivity model of the subsurface. While these methods come with an increase in computational costs due to their iterative nature, the resolution of the final reflectivity image can be drastically improved, as LSM techniques can suppress artifacts due to irregular acquisition geometries, band-limited source functions, and geometric spreading, among others [5].

The current state-of-the-art of LSM is Least-Squares Reverse-Time Migration (LS-RTM) [6], as it can achieve high-resolution reflectivity models due to its sophisticated forward and backward propagation operators. However, conventional LS-RTM suffers from two key limitations, namely a high computational cost and an inability to deal with multiple scattering effects. An alternative approach is given by Full-Wavefield Migration (FWM) [7, 8], which is based on one-way operators and iterative Neumann modelling. While this method also has limitations, most noticeably an inability to accurately model diving waves, its computational complexity is significantly reduced due to the use of one-way operators, while being able to accurately deal with multiple scattering effects.

A key challenge for all LSM techniques is the speed of convergence of the iterative method. In most cases, some form of gradient descent is used to iteratively update the reflectivity model. However, standard gradient descent algorithms typically suffer from slow convergence [9]. To accelerate their convergence, preconditioning can be applied. The most common preconditioner used in the context of LSM is the reciprocal of the Hessian operator [9]. As this operator is computationally expensive to calculate, approximations of the Hessian are commonly applied to reduce the computational complexity [10, 11]. In recent years, alternative approaches for constructing preconditioners have also been introduced, based on finding approximations of the pseudo-inverse operator, [12, 13].

In this paper, we extend FWM with a novel preconditioner, based on approximating the pseudo-inverse using Proper Orthogonal Decomposition (POD) [14]. To explore this new method, which we name Model-Order Reduced FWM (MOR-FWM), we first give a general description of the FWM method. Next, we discuss the POD method

and illustrate how this can be used as a preconditioner for FWM. Note that this approach can easily be extended to other least-squares migration techniques, which makes the method of broader interest. The preconditioned FWM algorithm is then tested on both the synthetic Marmousi model as well as on a field dataset from the Vøring basin. Finally, we end with a discussion of these results as well as our final conclusions.

4.2. THEORY

This section is split into two parts. In the first section we give a concise overview of the Full-Wavefield Modelling (FWMod) and FWM methods. Interested readers are encouraged to examine earlier work for a more comprehensive description of these methods [7, 8, 15, 16]. In the second section, we describe the MOR-FWM method, which uses Galerkin projections and POD to create a pre-conditioner.

4.2.1. FULL-WAVEFIELD MODELLING AND MIGRATION

We begin by examining a 2D version of the forward modelling algorithm FWMod. FWMod is based on splitting the full, acoustic, wavefield into up- and down-going wavefields. Following [15] and [8], we give the relationship between the up- and down-going wavefields at an interface located at $z = z_n$ for angular frequency ω, hence

$$\mathbf{q}^+(z_n) = \mathbf{R}^\cap(z_n)\,\mathbf{p}^-(z_n) + \mathbf{T}^+(z_n)\,\mathbf{p}^+(z_n), \tag{4.1}$$

$$\mathbf{q}^-(z_n) = \mathbf{R}^\cup(z_n)\,\mathbf{p}^+(z_n) + \mathbf{T}^-(z_n)\,\mathbf{p}^-(z_n), \tag{4.2}$$

where $\mathbf{q}^+(z_n)$, $\mathbf{q}^-(z_n)$, $\mathbf{p}^+(z_n)$ and $\mathbf{p}^-(z_n)$ are complex vectors of length N_x, with N_x the number of gridpoints in the lateral (x) direction, with $(\mathbf{q}/\mathbf{p})^\pm(z_n)\Big|_i = (q/p)^\pm(x_i, z_n)$. The symbols q and p denote waves traveling away from and towards the interface, respectively, while the superscripts $^+$ and $^-$ denote down- and up-going wavefields, respectively. The matrices $\mathbf{R}^\cup(z_n)$, $\mathbf{R}^\cap(z_n)$, $\mathbf{T}^+(z_n)$ and $\mathbf{T}^-(z_n)$ are real and of size $N_x \times N_x$, where $\mathbf{R}^\cup(z_n)$ and $\mathbf{R}^\cap(z_n)$ are the reflectivity operators for waves striking the interface from above and below, respectively, while $\mathbf{T}^+(z_n)$ and $\mathbf{T}^-(z_n)$ are the transmission operators for waves striking the interface from above and below, respectively. In a similar way, we give the relationship between wavefields at different depth levels, viz.

$$\mathbf{p}^+(z_{n+1}) = \mathbf{W}(z_{n+1}, z_n)\,\mathbf{q}^+(z_n), \tag{4.3}$$

$$\mathbf{p}^-(z_{n-1}) = \mathbf{W}(z_{n-1}, z_n)\,\mathbf{q}^-(z_n), \tag{4.4}$$

where the propagation operators $\mathbf{W}(z_{n+1}, z_n)$ and $\mathbf{W}(z_{n-1}, z_n)$ are complex matrices of size $N_x \times N_x$ describing the propagation between neighbouring depth levels. By recursively applying equations 4.1 - 4.4 we can model the wavefield at every depth level. This process is described in algorithm 5. Note the introduction of the vector $\boldsymbol{\sigma}(z_0)$ and scalar K in algorithm 5, where $\boldsymbol{\sigma}(z_0)$ is a complex vector of length N_x which describes the source wavefield at the surface z_0, while K denotes the number

of round-trips modelled. For each round-trip, the order of (internal) multiples modelled increases by one.

The procedure described in algorithm 5 can also be represented by the following forward modelling equations

$$\mathbf{p}_k^+(z_n) = \overline{\mathbf{W}}^+(z_n, z_0)\,\boldsymbol{\sigma}(z_0) + \sum_{m=0}^{n-1} \overline{\mathbf{W}}^+(z_n, z_m)\,\mathbf{R}^\cap(z_m)\,\mathbf{p}_{k-1}^-(z_m), \tag{4.5}$$

$$\mathbf{p}_k^-(z_n) = \sum_{m=n+1}^{N_z} \overline{\mathbf{W}}^-(z_n, z_m)\,\mathbf{R}^\cup(z_m)\,\mathbf{p}_k^+(z_m), \tag{4.6}$$

where, following [16], we have introduced the generalised propagation operators

$$\overline{\mathbf{W}}^+(z_n, z_m) = \left[\prod_{i=n-1}^{m+1} \mathbf{W}(z_{i+1}, z_i)\,\mathbf{T}^+(z_i)\right]\mathbf{W}(z_{m+1}, z_m), \tag{4.7}$$

$$\overline{\mathbf{W}}^-(z_n, z_m) = \left[\prod_{i=n+1}^{m-1} \mathbf{W}(z_{i-1}, z_i)\,\mathbf{T}^-(z_i)\right]\mathbf{W}(z_{m-1}, z_m). \tag{4.8}$$

We start examining the FWM inversion method using equations 4.5 - 4.8. Consider a small perturbation $\hat{\mathbf{R}}(z_n)$ to the background reflectivity operator $\mathbf{R}_0^\cup(z_n)$, viz. $\mathbf{R}^\cup(z_n) = \mathbf{R}_0^\cup(z_n) + \hat{\mathbf{R}}(z_n)$. Using continuity of the wavefields at an interface, we find $\mathbf{R}^\cap = -\mathbf{R}^\cup$, $\mathbf{T}^+ = \mathbf{I} + \mathbf{R}^\cup$ and $\mathbf{T}^- = \mathbf{I} + \mathbf{R}^\cap$, which gives

$$\mathbf{R}^{\cup/\cap}(z_n) = \mathbf{R}_0^{\cup/\cap}(z_n) \pm \hat{\mathbf{R}}(z_n), \tag{4.9}$$

$$\mathbf{T}^\pm(z_n) = \mathbf{T}_0^\pm(z_n) \pm \hat{\mathbf{R}}(z_n). \tag{4.10}$$

We now substitute equations 4.9 and 4.10 into equations 4.5 and 4.6 and model the background wavefields $\mathbf{p}_{0,k}^\pm$ propagating in the unperturbed, heterogeneous medium described by $\mathbf{R}_0^{\cup/\cap}(z_n)$ and $\mathbf{W}(z_{n\pm1}, z_n)$, hence

$$\mathbf{p}_{0,k}^+(z_n) = \overline{\mathbf{W}}_0^+(z_n, z_0)\,\boldsymbol{\sigma}(z_0) + \sum_{m=0}^{n-1} \overline{\mathbf{W}}_0^+(z_n, z_m)\,\mathbf{R}_0^\cap(z_m)\,\mathbf{p}_{0,k-1}^-(z_m), \tag{4.11}$$

$$\mathbf{p}_{0,k}^-(z_n) = \sum_{m=n+1}^{N_z} \overline{\mathbf{W}}_0^-(z_n, z_m)\,\mathbf{R}_0^\cup(z_m)\,\mathbf{p}_{0,k}^+(z_m). \tag{4.12}$$

Next, we model the additional wavefields $\hat{\mathbf{p}}_k^\pm$ arising from the perturbations $\hat{\mathbf{R}}(z_n)$. Ignoring second-order scattering due to these perturbations, we find

$$\hat{\mathbf{p}}_k^+(z_n) = \sum_{m=1}^{n-1} \overline{\mathbf{W}}_0^+(z_n, z_m)\,\hat{\mathbf{R}}(z_m)\left(\mathbf{p}_{0,k}^+(z_m) - \mathbf{p}_{0,k-1}^-(z_m)\right), \tag{4.13}$$

$$\hat{\mathbf{p}}_k^-(z_n) = \sum_{m=n+1}^{N_z} \overline{\mathbf{W}}_0^-(z_n, z_m)\left[\mathbf{R}_0^\cup(z_m)\,\hat{\mathbf{p}}_i^+(z_m) + \hat{\mathbf{R}}(z_m)\left(\mathbf{p}_{0,k}^+(z_m) - \mathbf{p}_{0,k}^-(z_m)\right)\right]. \tag{4.14}$$

Algorithm 5: Full Wavefield Modelling (FWMod)

Result: $\mathbf{p}_K^+(z_n)$ and $\mathbf{p}_K^-(z_n)$ for all z_n
Input: $\boldsymbol{\sigma}(z_0)$
Set $\mathbf{p}_0^-(z_n) = \mathbf{0}$ for all z_n;
for $k = 1 : K$ **do**
  Set $\mathbf{p}_k^+(z_0) = \boldsymbol{\sigma}(z_0)$;
  for $n = 0 : N_z - 1$ **do**
    $\mathbf{q}_k^+(z_n) = \mathbf{R}^{\cap}(z_n)\,\mathbf{p}_{k-1}^-(z_n) + \mathbf{T}^+(z_n)\,\mathbf{p}_k^+(z_n)$;
    $\mathbf{p}_k^+(z_{n+1}) = \mathbf{W}(z_{n+1}, z_n)\,\mathbf{q}_k^+(z_n)$;
  end
  Set $\mathbf{p}_k^-(z_{N_z}) = \mathbf{0}$;
  for $n = N_z : -1 : 2$ **do**
    $\mathbf{q}_k^-(z_n) = \mathbf{R}^{\cup}(z_n)\,\mathbf{p}_k^+(z_n) + \mathbf{T}^-(z_n)\,\mathbf{p}_k^-(z_n)$;
    $\mathbf{p}_k^-(z_{n-1}) = \mathbf{W}(z_{n-1}, z_n)\,\mathbf{q}_k^-(z_n)$;
  end
end

Note the use of the subscript $_0$ to denote wavefields and operators in the unperturbed background medium, and the use of the caret symbol $\hat{}$ to denote wavefields and operators due to the perturbation $\hat{\mathbf{R}}(z_n)$.

We now assume the reflectivity operator to be angle-independent, as we aim to reconstruct a structural image of the subsurface, in which case $\mathbf{R}_0^{\cup}(z_n)$ and $\hat{\mathbf{R}}(z_n)$ are diagonal matrices. Assuming $\mathbf{p}_{0,k-1}^-(z_n) \approx \mathbf{p}_{0,k}^-(z_n)$, the upgoing wavefield at the surface is then given by

$$\hat{\mathbf{p}}_k^-(z_0) = \sum_{m=0}^{N_z} \left(\overline{\mathbf{W}}_0^{\cup}(z_0, z_m) + \overline{\mathbf{W}}_0^-(z_0, z_m)\right) \hat{\mathbf{r}}(z_m) \circ \left(\mathbf{p}_{0,k}^+(z_m) - \mathbf{p}_{0,k}^-(z_m)\right), \tag{4.15}$$

where $\circ$ represents the Hadamard product, and we have introduced $\hat{\mathbf{r}}(z_m)$, a real vector of length N_x with elements $\hat{\mathbf{r}}(z_m)|_i = \hat{\mathbf{R}}(z_m)\big|_{ii}$, and

$$\overline{\mathbf{W}}_0^{\cup}(z_0, z_n) = \sum_{m=n+1}^{N_z} \overline{\mathbf{W}}_0^-(z_0, z_m)\,\mathbf{R}_0^{\cup}(z_m)\,\overline{\mathbf{W}}_0^+(z_m, z_n). \tag{4.16}$$

As the Hadamard product is commutative, we can write

$$\hat{\mathbf{p}}_k^-(z_0) = \sum_{m=0}^{N_z} \left(\overline{\mathbf{W}}_0^{\cup}(z_0, z_m) + \overline{\mathbf{W}}_0^-(z_0, z_m)\right) \left(\mathbf{P}_{0,k}^+(z_m) - \mathbf{P}_{0,k}^-(z_m)\right) \hat{\mathbf{r}}(z_m), \tag{4.17}$$

where $\mathbf{P}_{0,k}^{\pm}(z_m) = \mathrm{diag}\left(\mathbf{p}_{0,k}^{\pm}(z_m)\right)$. As equation 4.17 is linear with respect to $\hat{\mathbf{r}}(z_m)$, it can be written as

$$\hat{\mathbf{p}}_k^-(z_0) = \mathbf{A}_{\omega,\sigma}\hat{\mathbf{r}}, \tag{4.18}$$

where $\mathbf{A}_{\omega,\sigma}$ is a complex matrix of size $N_x \times N_x N_z$, constructed by horizontally chaining the matrices $\left(\overline{\mathbf{W}}_0^{\cup} + \overline{\mathbf{W}}_0^{-}\right)\left(\mathbf{P}_{0,k}^{+} - \mathbf{P}_{0,k}^{-}\right)$, and $\hat{\mathbf{r}}$ is a real vector of length $N_x N_z$, constructed by vertically chaining the vectors $\hat{\mathbf{r}}(z_m)$. Up until now, we have examined the wavefield at a single frequency ω due to a single source, with corresponding source wavefield $\boldsymbol{\sigma}(z_0)$, as represented by $\mathbf{A}_{\omega,\sigma}$ in equation 4.18. The full wavefield for all sources and frequencies can be written as

$$\mathbf{p}_k^{-,\text{full}}(z_0) - \mathbf{p}_{0,k}^{-,\text{full}}(z_0) = \mathbf{A}\hat{\mathbf{r}} \Leftrightarrow \begin{bmatrix} \hat{\mathbf{p}}_k^{-}(\omega_1, \boldsymbol{\sigma}_1, z_0) \\ \vdots \\ \hat{\mathbf{p}}_k^{-}(\omega_{N_\omega}, \boldsymbol{\sigma}_{N_\sigma}, z_0) \end{bmatrix} = \begin{bmatrix} \mathbf{A}_{\omega_1,\sigma_1} \\ \vdots \\ \mathbf{A}_{\omega_{N_\omega},\sigma_{N_\sigma}} \end{bmatrix} \hat{\mathbf{r}}, \tag{4.19}$$

which is constructed by vertically chaining the vectors $\hat{\mathbf{p}}_k^{-}(z_0)$ and matrices $\mathbf{A}_{\omega,\sigma}$ of equation 4.18.

To perform FWM, we first set $\mathbf{p}_k^{-,\text{full}}(z_0) = \mathbf{d}$, with $\mathbf{d}$ a complex vector of length $N_x N_\sigma N_\omega$ containing the recorded wavefield at the surface for all N_σ sources and all N_ω frequencies. We now wish to solve equation 4.19 for the reflectivity vector $\hat{\mathbf{r}}$. The most straightforward approach to obtain $\hat{\mathbf{r}}$ is via the pseudo-inverse of $\mathbf{A}$, hence

$$\hat{\mathbf{r}} = \left(\mathbf{A}^{\mathbf{H}}\mathbf{A}\right)^{-1}\mathbf{A}^{\mathbf{H}}\left(\mathbf{d} - \mathbf{p}_{0,k}^{-,\text{full}}(z_0)\right), \tag{4.20}$$

where the superscript $^{\mathbf{H}}$ represents the conjugate transpose. However, this is impractical, as $\mathbf{A}$ is of size $N_x N_\sigma N_\omega \times N_x N_z$ in 2D. This makes it prohibitively expensive computationally to calculate the matrix inverse. Instead, we define a cost function J, with

$$J = \frac{1}{2}\sum_{i,j}\left\|\left(\mathbf{d}(\omega_i, \boldsymbol{\sigma}_j) - \mathbf{p}_{0,k}^{-}(\omega_i, \boldsymbol{\sigma}_j, z_0)\right) - \mathbf{A}_{\omega_i,\sigma_j}\hat{\mathbf{r}}\right\|^2, \tag{4.21}$$

where $\|\ldots\|$ is the Euclidean norm of the vector. We now perform gradient descent to find $\hat{\mathbf{r}}$. As equation 4.19 is linear in $\hat{\mathbf{r}}$, the gradient of the cost function J is given by

$$\frac{\partial J}{\partial \hat{\mathbf{r}}} = -\sum_{i,j}\text{Re}\left(\mathbf{A}_{\omega_i,\sigma_j}^{\mathbf{H}}\mathbf{e}_k(\omega_i, \boldsymbol{\sigma}_j)\right), \tag{4.22}$$

where

$$\mathbf{e}_k(\omega_i, \boldsymbol{\sigma}_j) = \mathbf{d}(\omega_i, \boldsymbol{\sigma}_j) - \mathbf{p}_{0,k}^{-}(\omega_i, \boldsymbol{\sigma}_j, z_0) - \mathbf{A}_{\omega_i,\sigma_j}\hat{\mathbf{r}}. \tag{4.23}$$

We now use this gradient to update the reflectivity

$$\mathbf{r}^{\cup} = \mathbf{r}_0^{\cup} + \alpha\frac{\partial J}{\partial \hat{\mathbf{r}}}, \tag{4.24}$$

where the (real-valued) scalar α is given by

$$\alpha = \frac{Re\left[\left(\mathbf{A}\frac{\partial J}{\partial \hat{\mathbf{r}}}\right)^{\mathbf{H}}\mathbf{e}_k\right]}{\left\|\mathbf{A}\frac{\partial J}{\partial \hat{\mathbf{r}}}\right\|^2}. \tag{4.25}$$

Setting $\mathbf{r}_0^{\cup} = \mathbf{r}^{\cup}$, we can now repeat this process for multiple iterations to gradually minimize the cost function J. The full FWM process is summarized in algorithm 6. Note that equations 4.22 and 4.25 can be calculated using a depth-recursive approach similar to the one shown in algorithm 5. This significantly reduces the computational cost of algorithm 6.

4.2.2. MODEL-ORDER REDUCED FULL-WAVEFIELD MIGRATION USING PROPER ORTHOGONAL DECOMPOSITION

In this section, we examine an alternative approach to solve equation 4.19, based on Galerkin projections and POD. We begin by describing the method of Galerkin projections for a linear system. Assume the final solution $\hat{\mathbf{r}}$ can be written as a linear combination of N_r known basis vectors $\hat{\mathbf{r}}_{r,i}$ where $N_r \ll N_x N_z$, i.e.

$$\hat{\mathbf{r}} \approx \sum_i c_i \hat{\mathbf{r}}_{r,i} = \hat{\mathbf{R}}_r \mathbf{c}, \tag{4.26}$$

where $\hat{\mathbf{R}}_r$ is a real matrix of size $N_x N_z \times N_r$, with columns $\hat{\mathbf{r}}_{r,i}$, and $\mathbf{c}$ is a vector of the coefficients c_i. Equation 4.19 can then be rewritten as

$$\mathbf{A}\hat{\mathbf{R}}_r\mathbf{c} = \mathbf{d} - \mathbf{p}_{0,k}^{-,\text{full}}(z_0). \tag{4.27}$$

Left-multiplying both sides of equation 4.27 by $\left(\mathbf{A}\hat{\mathbf{R}}_r\right)^{\mathbf{H}}$ and taking the inverse gives

$$\mathbf{c} = \left(\begin{bmatrix} Re\left(\mathbf{A}\hat{\mathbf{R}}_r\right) \\ Im\left(\mathbf{A}\hat{\mathbf{R}}_r\right) \end{bmatrix}^{\mathbf{H}} \begin{bmatrix} Re\left(\mathbf{A}\hat{\mathbf{R}}_r\right) \\ Im\left(\mathbf{A}\hat{\mathbf{R}}_r\right) \end{bmatrix}\right)^{-1} \begin{bmatrix} Re\left(\mathbf{A}\hat{\mathbf{R}}_r\right) \\ Im\left(\mathbf{A}\hat{\mathbf{R}}_r\right) \end{bmatrix}^{\mathbf{H}} \begin{bmatrix} Re\left(\mathbf{d} - \mathbf{p}_{0,k}^{-,\text{full}}(z_0)\right) \\ Im\left(\mathbf{d} - \mathbf{p}_{0,k}^{-,\text{full}}(z_0)\right) \end{bmatrix}, \tag{4.28}$$

where we have separated the real and imaginary parts to ensure that the coefficient vector $\mathbf{c}$ is real. After using equation 4.28 to find the coefficients c_i, the perturbation $\hat{\mathbf{r}}$ can be computed using equation 4.26.

Note the similarity of equation 4.28 to equation 4.20. Both equations represent taking the pseudo-inverse of equation 4.19. However, equation 4.20 requires taking the inverse of a matrix of size $N_x N_z \times N_x N_z$, while equation 4.28 reduces the size of this matrix to $N_r \times N_r$. Therefore, in situations where one can find a small set of basis vectors $\hat{\mathbf{r}}_{r,i}$ that describe the full solution $\hat{\mathbf{r}}$ such that $N_r \ll N_x N_z$, the method of Galerkin projections can dramatically reduce the cost of calculating the (pseudo-)inverse. Note that this method can be applied generally to any linear system, given that one can find an appropriate set of basis vectors $\hat{\mathbf{r}}_{r,i}$.

To find an appropriate set of basis vectors $\hat{\mathbf{r}}_{r,i}$ to form $\hat{\mathbf{R}}_r$ we apply POD. Hence,

Algorithm 6: Conventional Full Wavefield Migration (FWM)

Result: Reflectivity model $\mathbf{r}^{\cup}$.
Input: Measured data $\mathbf{d}$
Set $\mathbf{r}^{\cup} = \mathbf{0}$;
for $k = 1 : K$ **do**
  Set $\mathbf{r}_0^{\cup} = \mathbf{r}^{\cup}$;
  Calculate $\mathbf{p}_{0,k}^{+}(z_n)$ and $\mathbf{p}_{0,k}^{-}(z_n)$ for all z_n using algorithm 5;
  Calculate $\frac{\partial J}{\partial \hat{\mathbf{r}}} = -\sum_{i,j} \mathrm{Re}\left(\mathbf{A}^{\mathbf{H}}_{\omega_i,\sigma_j}\mathbf{e}_k(\omega_i,\boldsymbol{\sigma}_j)\right)$;
  Calculate $\alpha = Re\left[\left(\mathbf{A}\frac{\partial J}{\partial \hat{\mathbf{r}}}\right)^{\mathbf{H}}\mathbf{e}_k\right] \Big/ \left\|\mathbf{A}\frac{\partial J}{\partial \hat{\mathbf{r}}}\right\|^2$;
  Update reflectivity $\mathbf{r}^{\cup} = \mathbf{r}_0^{\cup} + \alpha\frac{\partial J}{\partial \hat{\mathbf{r}}}$
end

4

we will construct $\hat{\mathbf{r}}_{r,i}$ from a set of partial solutions $\mathbf{s}_j$ for $j = 1,\ldots,N_s$, such that $N_r \ll N_s \ll N_x N_z$. These partial solutions may be solutions for a part of the domain, solutions to related problems, or low-fidelity solutions acquired by applying a less expensive approach. Note the correlation to machine learning, where the partial solutions $\mathbf{s}_j$ can be interpreted as the training data for the method.

To construct $\hat{\mathbf{R}}_r$ given the partial solutions $\mathbf{s}_j$, we begin by constructing the so-called solution matrix $\mathbf{S}$, which is a real matrix of size $N_x N_z \times N_s$, with columns $\mathbf{s}_j$. Next, we take the Singular Value Decomposition (SVD) of $\mathbf{S}$ such that $\mathbf{U}\Sigma\mathbf{V}^{\mathbf{T}} = \mathbf{S}$. The basis vectors $\hat{\mathbf{r}}_{r,i}$ are then given by the columns $\mathbf{u}_i$ of the matrix $\mathbf{U}$. The number of basis vectors required depends on the decay of the singular values $\Sigma|_{ii}$. The faster the decay of the singular values, the fewer basis vectors $\hat{\mathbf{r}}_{r,i}$ are required to span the same domain as the domain spanned by the vectors $\mathbf{s}_j$. Note that we assume that the full solution $\hat{\mathbf{r}}$ falls within the span of $\mathbf{s}_j$, as this is required for the resulting vectors $\hat{\mathbf{r}}_{r,i}$ of the POD process to be appropriate basis vectors for $\hat{\mathbf{r}}$.

To apply POD to FWM, we must therefore first construct an appropriate solution matrix $\mathbf{S}$. Recalling the conventional FWM approach described in section 4.2.1, we find that a natural choice for the partial solution vectors $\mathbf{s}_j$ is provided by the components of the gradient $\frac{\partial J}{\partial \hat{\mathbf{r}}}$, i.e.

$$\mathbf{S} = \begin{bmatrix} \mathrm{Re}\left(\mathbf{A}^{\mathbf{H}}_{\omega_1,\sigma_1}\mathbf{e}_k(\omega_1,\boldsymbol{\sigma}_1)\right) & \ldots & \mathrm{Re}\left(\mathbf{A}^{\mathbf{H}}_{\omega_{N_\omega},\sigma_{N_\sigma}}\mathbf{e}_k\left(\omega_{N_\omega},\boldsymbol{\sigma}_{N_\sigma}\right)\right) \end{bmatrix}, \tag{4.29}$$

as these components are partial solutions of equation 4.19 for a given frequency ω and source wavefield $\boldsymbol{\sigma}(z_0)$. Next, we calculate the SVD of the solution matrix $\mathbf{S}$ and construct the low-rank solution matrix $\hat{\mathbf{R}}_r$ from the left singular vectors $\mathbf{u}_i$ as follows:

$$\hat{\mathbf{R}}_r = \begin{bmatrix} \frac{\partial J}{\partial \hat{\mathbf{r}}} & \tilde{\mathbf{u}}_1 & \ldots & \tilde{\mathbf{u}}_{N_\Sigma} \end{bmatrix}, \tag{4.30}$$

with N_Σ the maximum rank we choose to take into account, which can be chosen manually or by using an error criterion. In equation 4.30 we have explicitly included

the conventional gradient $\frac{\partial J}{\partial \hat{\mathbf{r}}}$ and we have applied a Gram-Schmidt procedure to the vectors $\mathbf{u}_i$ to form the vectors $\tilde{\mathbf{u}}$, which are orthogonal to the conventional gradient. This guarantees that the original gradient always falls in the span of $\hat{\mathbf{r}}_{r,i}$, guaranteeing that the reflectivity update produced by MOR-FWM can never be worse than the update produced by the conventional method. Therefore, the method can be seen as a pre-conditioner of the conventional gradient.

Using $\hat{\mathbf{R}}_r$, we now apply equation 4.28 to calculate the coefficient vector $\mathbf{c}$. Finally, knowing $\hat{\mathbf{R}}_r$ and $\mathbf{c}$, we use equation 4.26 to retrieve the reflectivity update, viz. $\hat{\mathbf{r}} = \hat{\mathbf{R}}_r \mathbf{c}$. This process is summarized in algorithm 7.

4.3. NUMERICAL RESULTS

In this section we examine the results obtained with the MOR-FWM method for a synthetic and a field data example. We compare these results with the reconstructions obtained using the conventional FWM method to illustrate the advantages and disadvantages of the approach introduced in this paper.

4.3.1. SYNTHETIC EXAMPLE: MARMOUSI MODEL

We begin with the synthetic example, where we have applied the method on a part of the Marmousi model. Data was generated using a time-domain finite-difference scheme [17] using a source wavefield with a Ricker wavelet signature. The parameters used in the modelling and inversion scheme are given in table 4.1. The imaging results are shown in figure 4.1.

Examining figure 4.1, we see that both the conventional FWM method as well as the MOR-FWM method outlined in section 4.2.2 have produced a reasonable reconstruction of the reflectivity image corresponding to the underlying velocity and density models. However, while the differences between the results of the two methods are modest, in certain areas the MOR-FWM result shows improved consistency and better resolution compared to the conventional method.

Comparing figures 4.1g) and 4.1h), for example, we see that the MOR-FWM method has done a better job of reconstructing the two layers right above the strong reflector in the middle of the figure (bottom three arrows). We also see that the layers in figure 4.1h) are a bit sharper (top two arrows). Figures 4.1j) and 4.1k) show a similar behaviour. The two layers at the top of the image are better resolved in figure 4.1k) compared to figure 4.1j) (top three arrows), and the layers are slightly sharper throughout the MOR-FWM figure (bottom two arrows).

This conclusion is further supported by figure 4.1c), where we have plotted the cost function J as a function of the iteration number k. From this figure, we see that the MOR-FWM method yields a reduced data residual compared to the conventional FWM method, lending further support for the MOR-FWM method.

4.3.2. FIELD DATA EXAMPLE: VØRING BASIN

Next, we examine the field data example, where we have tested the method on a marine field dataset from the Vøring basin in Norway (see [16] for more details). The

Algorithm 7: Model-Order Reduced Full Wavefield Migration (MOR-FWM)

Result: Reflectivity model $\mathbf{r}^{\cup}$.
Input: Measured data $\mathbf{d}$
Set $\mathbf{r}^{\cup} = \mathbf{0}$;
for $k = 1 : K$ **do**
  Set $\mathbf{r}_0^{\cup} = \mathbf{r}^{\cup}$;
  Calculate $\mathbf{p}_{0,k}^{+}(z_n)$ and $\mathbf{p}_{0,k}^{-}(z_n)$ for all z_n using algorithm 5;
  Calculate solution matrix $\mathbf{S}$ using equation 4.29;
  Calculate SVD of $\mathbf{S} \Rightarrow \mathbf{U}\Sigma\mathbf{V}^T = \mathbf{S}$;
  Construct low-rank partial solutions $\hat{\mathbf{r}}_{r,i} = \tilde{\mathbf{u}}_i$;
  Calculate wavefield perturbations $\mathbf{A}\hat{\mathbf{R}}_r$ using a modified version of algorithm 5;
  Solve reduced system $\mathbf{A}\hat{\mathbf{R}}_r\mathbf{c} = \mathbf{d} - \mathbf{p}_{0,k}^{-,\text{full}}(z_0)$ using equation 4.28;
  Update reflectivity $\mathbf{r}^{\cup} = \mathbf{r}_0^{\cup} + \hat{\mathbf{R}}_r\mathbf{c}$
end

parameters used for this dataset are shown in table 4.2 and the results in figure 4.2.

Comparing figures 4.2a) and 4.2b), as well as examining 4.2d), we see that the difference between the two methods is significantly smaller than in section 4.3.1. This can also be seen from the cost functional J, shown in figure 4.4d), we see similar behaviour. Both the conventional FWM method as well as the MOR-FWM method yield very similar values after 5 iterations. However, we note that the MOR-FWM method outperforms the conventional FWM method when fewer iterations are used. This effect is discussed in more detail in section 4.4.2.

Table 4.1: Parameters Marmousi model

Lateral grid spacing Δx	10 m	Vertical grid spacing Δz	5 m
Number of lateral gridpoints N_x	431	Number of vertical gridpoints N_z	500
Peak frequency f_{pk}	17 Hz	Minimum frequency f_{min}	2 Hz
Maximum frequency f_{max}	40 Hz	Number of sources N_σ	44
Source spacing $\Delta\sigma$	100 m	Number of iterations K	8
Number of singular vectors N_Σ	50		

Table 4.2: Parameters Voring data

Lateral grid spacing Δx	25 m	Vertical grid spacing Δz	5 m
Number of lateral gridpoints N_x	399	Number of vertical gridpoints N_z	1001
Minimum frequency f_{min}	2 Hz	Maximum frequency f_{max}	60 Hz
Number of sources N_σ	23	Source spacing $\Delta\sigma$	450 m
Number of iterations K	5	Number of singular vectors N_Σ	50

4.4. DISCUSSION

Based on the results shown in figure 4.1 and 4.2, we observe that the MOR-FWM method generates slightly better reconstructions compared to the conventional FWM method. More distinct layers are recovered and the layers are sharper to the eye when the MOR-FWM method is used. This is consistent with the interpretation of the method as a preconditioner to the conventional approach. In this section, we compare the computational cost of both methods as well as exploring methods to improve the results further.

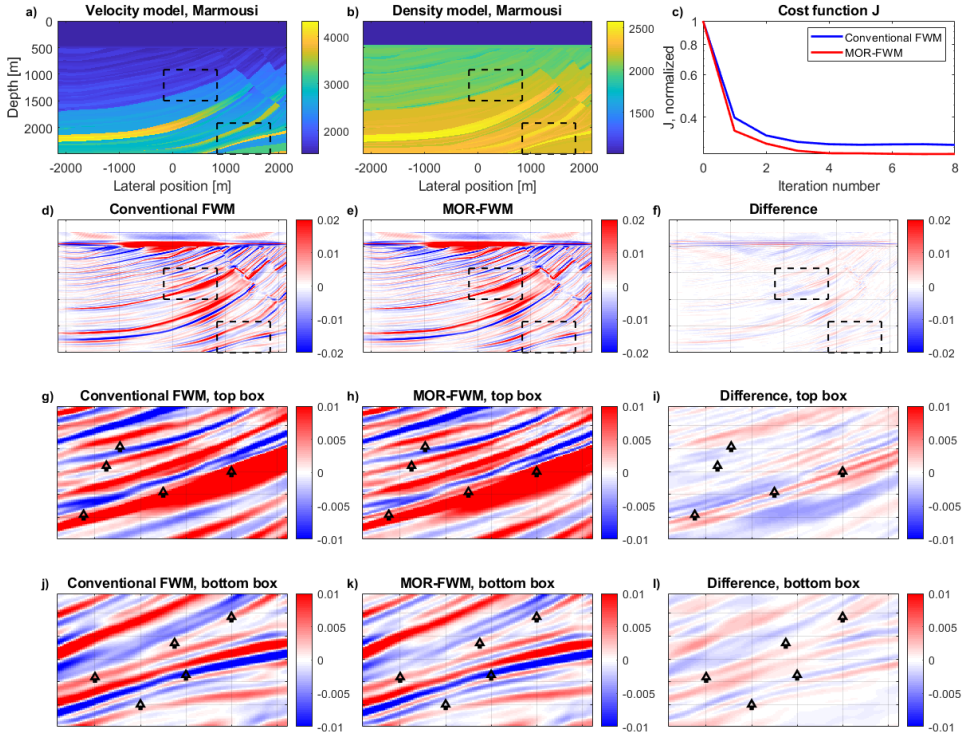

Figure 4.1: FWM and MOR-FWM results for the synthetic Marmousi example. Figures a) and b) show the velocity and density model, respectively, of the part of the Marmousi model under consideration. Figure c) shows the data residual J, which has been normalized with respect to the residual for $\mathbf{p}_{0,1}^{-} = \mathbf{0}$. Figures d), e) and f) show the conventional FWM and MOR-FWM image after 8 iterations, respectively, as well as the difference between the two images. Figures g), h) and i) show a zoom-in of the FWM image, the MOR-FWM image and their difference at the location of the top box, respectively, while figures j), k) and l) show zoom-ins of the bottom box. Arrows indicate regions of interest within the figures.

4.4.1. COMPUTATIONAL COSTS

We begin by comparing the computational costs of algorithm 6, which describes the conventional FWM method, and algorithm 7, which describes the MOR-FWM method.

Both algorithms begin by calculating the forward modelled wavefields $\mathbf{p}^+_{0,k}(z_n)$ and $\mathbf{p}^-_{0,k}(z_n)$ in the background medium, followed by calculating $\mathrm{Re}\left(\mathbf{A}^{\mathbf{H}}_{\omega,\sigma}\mathbf{e}_k(\omega,\boldsymbol{\sigma})\right)$ for all frequencies ω and source wavefields $\boldsymbol{\sigma}(z_0)$, which is either used to calculate the gradient of the cost functional J (conventional FWM, equation 4.22), or construct the solution matrix $\mathbf{S}$ (MOR-FWM, equation 4.29). Next, in the MOR-FWM algorithm, the SVD of the solution matrix $\mathbf{S}$ is calculated to find the basis vectors $\hat{\mathbf{r}}_{r,i} = \tilde{\mathbf{u}}_i$. Assuming that the maximum rank N_Σ taken into account is much smaller than the number of partial solutions $\mathbf{s}_j$, this step has a negligible computational cost.

The real difference between the two methods lies in the next step, the calculation of the wavefield perturbations $\mathbf{A}\frac{\partial J}{\partial \bar{\mathbf{r}}}$ (algorithm 6, step 6) and $\mathbf{A}\hat{\mathbf{R}}_r$ (algorithm 7, step 8). In the MOR-FWM method, the wavefield perturbations for each basis vector $\hat{\mathbf{r}}_{r,i}$ must be calculated, while in the conventional FWM method only the wavefield perturbation due to the gradient $\frac{\partial J}{\partial \bar{\mathbf{r}}}$ is required. Therefore, this step is more expensive computationally by a factor of N_Σ for the MOR-FWM method, where N_Σ is the number of basis vectors taken into account. As the other steps are either identical or have negligible computational costs, this step fully determines the difference in computational cost between the two methods.

To reduce the computational cost of this step, a number of approaches may be used. First, one can reduce the number basis vectors N_Σ used. This will reduce the computational cost, but may lead to smaller improvements to the reconstruction. Alternatively, other choices for the basis vectors may be explored. For example, alternative choices for the partial solutions $\mathbf{s}_j$ may lead to a more rapid decay of the singular values of the solution matrix $\mathbf{S}$, in which case fewer basis vectors are required to yield a high-quality preconditioner. Finally, if the basis vectors $\hat{\mathbf{r}}_{r,i}$ can be estimated a priori, the construction of the solution matrix $\mathbf{S}$ and its SVD can be omitted, and the calculation of $\mathbf{A}\hat{\mathbf{R}}_r$ can be performed offline, as it does not depend on the measured data $\mathbf{d}$. Such a situation may arise in monitoring applications, for example, where high-quality estimates of the reflectivity may already exist.

4.4.2. RESULTS AFTER 1 ITERATION

Next, we compare the performance of the conventional FWM and the MOR-FWM methods after a single iteration, the results of which are shown in figures 4.3 and 4.4. From this figure, we see that the MOR-FWM method requires fewer iterations to produce a sharp image compared to the conventional method. Comparing figures 4.4a) and b), for example, we see that the MOR-FWM method displays an improved resolution at the edges of the model at the first iteration (left-most arrow). Also, we see an improved recovery of the strong reflectors in the zoomed-in image (top-left arrow). Finally, we see an improved continuity of the weaker reflectors deeper in the image (right and bottom arrows).

This result suggests that, using the MOR-FWM method, one may require fewer

iterations to retrieve a sharp image. This is further supported by the cost function J, shown in figure 4.4d), which shows that the MOR-FWM method achieves a smaller data misfit even at the first iteration. This is especially relevant when FWM is applied in the context of One-way Reflection Waveform Inversion [18], also known as Joint Migration Inversion [19], where the (background) speed-of-sound model is also updated. In this context it is important to generate an accurate reflectivity model using only a few iterations, as the reflectivity model must be updated each time the speed-of-sound model is adjusted.

4.4.3. NORMALIZATION

Finally, we examine a potential alternative choice for the partial solutions $\mathbf{s}_j$. Recall that the partial solutions $\mathbf{s}_j$ are given by $\mathrm{Re}\left(\mathbf{A}^{\mathbf{H}}_{\omega,\sigma}\mathbf{e}_k(\omega,\boldsymbol{\sigma})\right)$ for a given frequency ω and source wavefield $\boldsymbol{\sigma}(z_0)$ (equation 4.29). While this is a natural choice, a downside of this approach is that it is sensitive to the source signature. This means that in cases where certain frequencies or sources have larger amplitudes than others, the corresponding partial solutions will also exhibit larger amplitudes. When taking the SVD of the solution matrix $\mathbf{S}$, the basis vectors $\mathbf{u}_i$ will then be weighted towards the partial solutions with the largest amplitudes, meaning that not all sources and frequencies are treated equally in the construction of the basis vectors.

To circumvent this shortcoming, one can choose to normalize each partial solution $\mathbf{s}_j$. This can be done in conventional FWM, where all contributions are simply summed together, or in MOR-FWM, where the normalized partial solutions are used in the SVD. Using this approach, we retrieve the results shown in figure 4.5. Looking at this figure, we see that the imprint of the source signature has been removed, removing a number of spurious reflectors. Due to this effect, we see an improved image in the target zone below the overburden, indicated by the box.

We also notice a more pronounced difference between the two methods. Comparing figures 4.5a) and b), we see that the reflectors in the target zone exhibit a greater continuity when normalized MOR-FWM is applied compared to normalized FWM. This observation is supported by the cost function J, shown in figure 4.4d), which shows an improved data misfit for normalized MOR-FWM. These results underline the sensitivity of the MOR-FWM method to the choice of basis vectors, as a well-chosen set of basis vectors can significantly improve the results.

4.5. CONCLUSION

In this paper, we introduce a novel preconditioner for Full-Wavefield migration, using Proper Orthogonal Decomposition to find a reduced basis. We show that this reduced basis can be used to construct a preconditioner using Galerkin projections. We tested the resulting algorithm on the synthetic Marmousi model and a field data set from the Vøring basin, where we achieve improved results in both cases compared to the conventional FWM algorithm. We discuss the challenge of the computational cost of the method, which depends linearly on the number of basis vectors used, and present some ideas to further improve the results and/or reduce the computational costs. Based on the flexibility of the method, as well as the

results we present in this paper, we conclude that the MOR-FWM method is a useful addition to the existing work on migration in general and FWM in particular.

4.6. ACKNOWLEDGMENTS

The authors thank the sponsoring companies from the Delphi Consortium at Delft University of Technology for their support to this research, and in particular Equinor for providing the Vøring Basin field data.

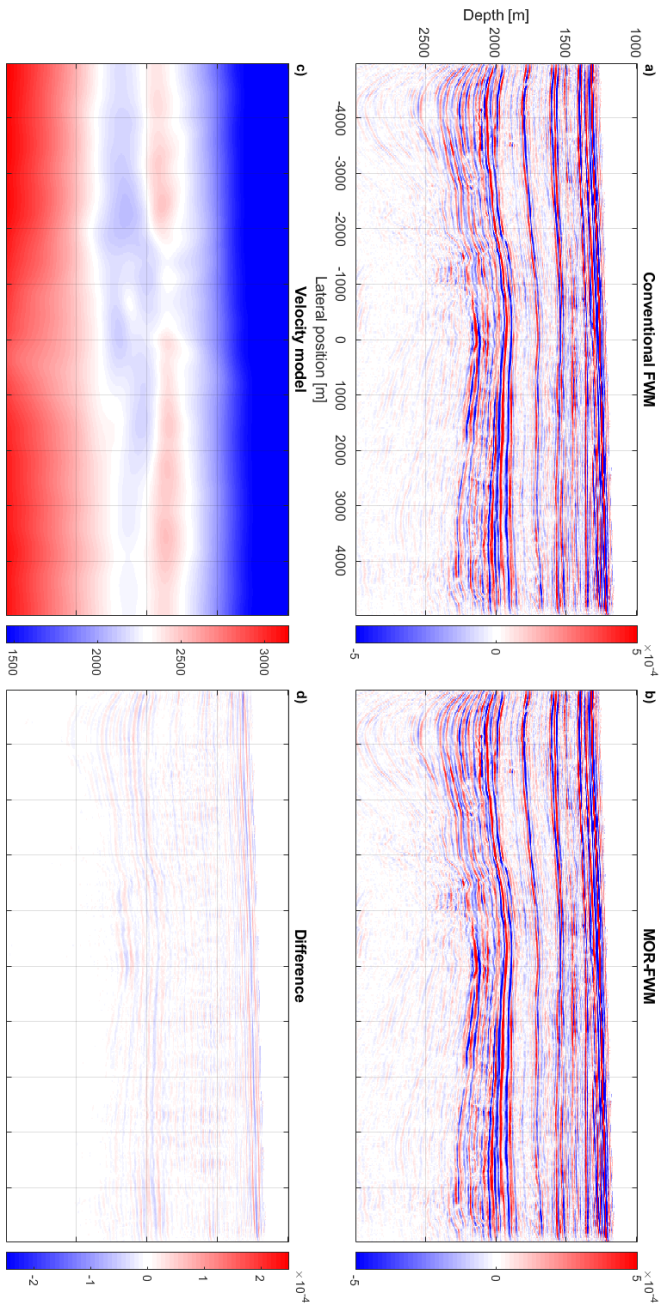

Figure 4.2: FWM and MOR-FWM results for the Vøring field data example. Figure c) shows the velocity model used for migration. Figures a), b) and d) show the conventional FWM and MOR-FWM image after 5 iterations, respectively, as well as the difference between the two images. Note that the difference figures have been plotted with half the clip value of the FWM and MOR-FWM images.

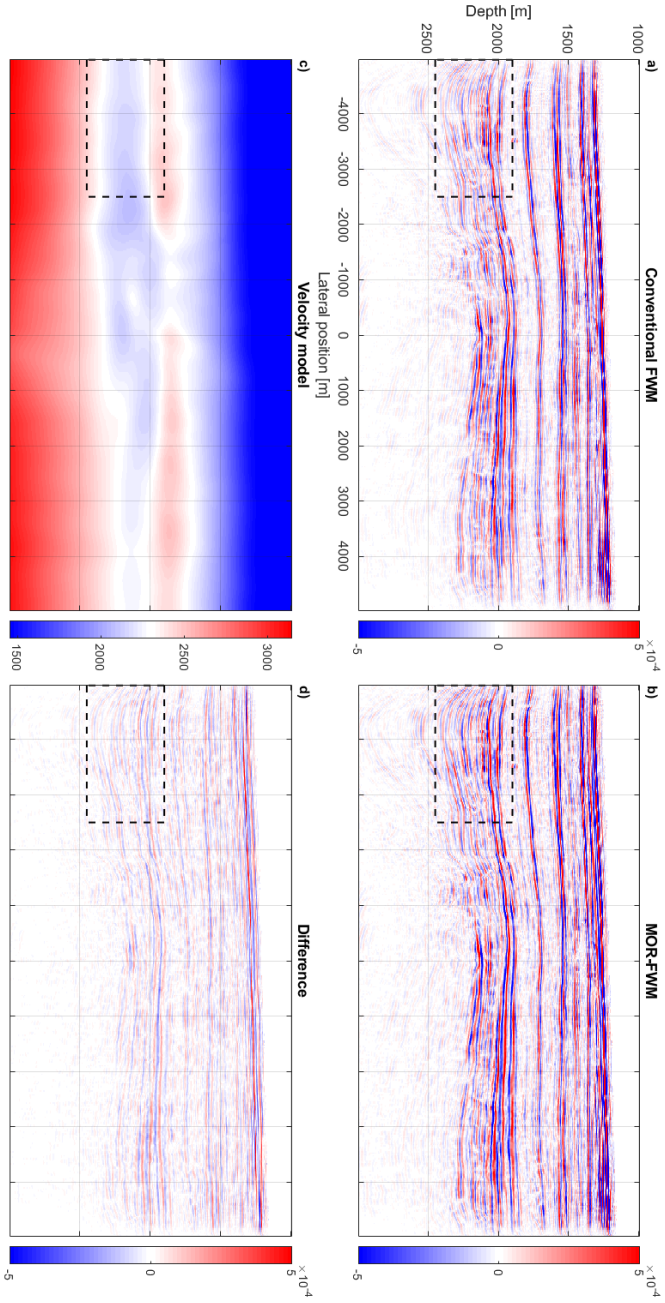

Figure 4.3: FWM and MOR-FWM results for the Vøring field data example after 1 iteration. Figures a), b) and d) show the conventional FWM and MOR-FWM image after 1 iteration, respectively, as well as the difference between the two images. Figure c) shows the velocity model used for migration. Note that the box plotted in the figures indicates the region displayed in figure 4.4.

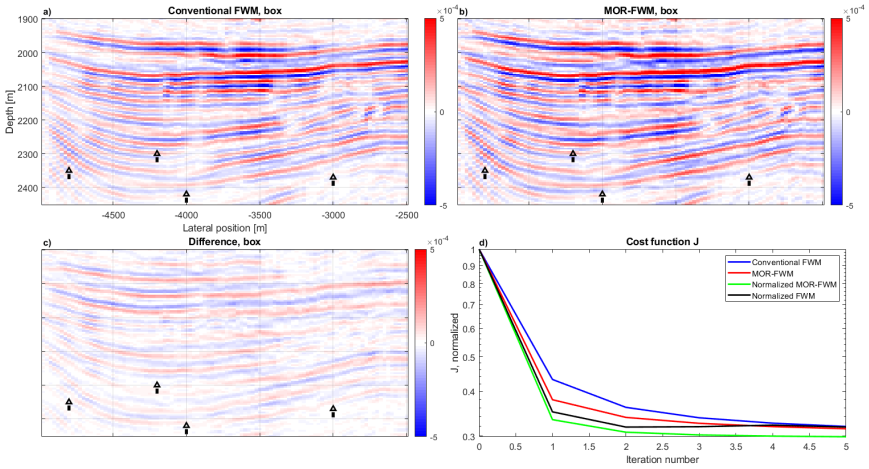

Figure 4.4: Zoom-in of the FWM and MOR-FWM results for the Vøring field data example after 1 iteration. Figures a), b) and c) show the conventional FWM and MOR-FWM image after 1 iteration, respectively, as well as the difference between the two images. Arrows indicate regions of interest within the figures. Figure a) shows the velocity model used for migration. Figure d) shows the data residual J, which has been normalized with respect to the residual for $\mathbf{p}^{-}_{\mathbf{0},\mathbf{1}} = \mathbf{0}$.

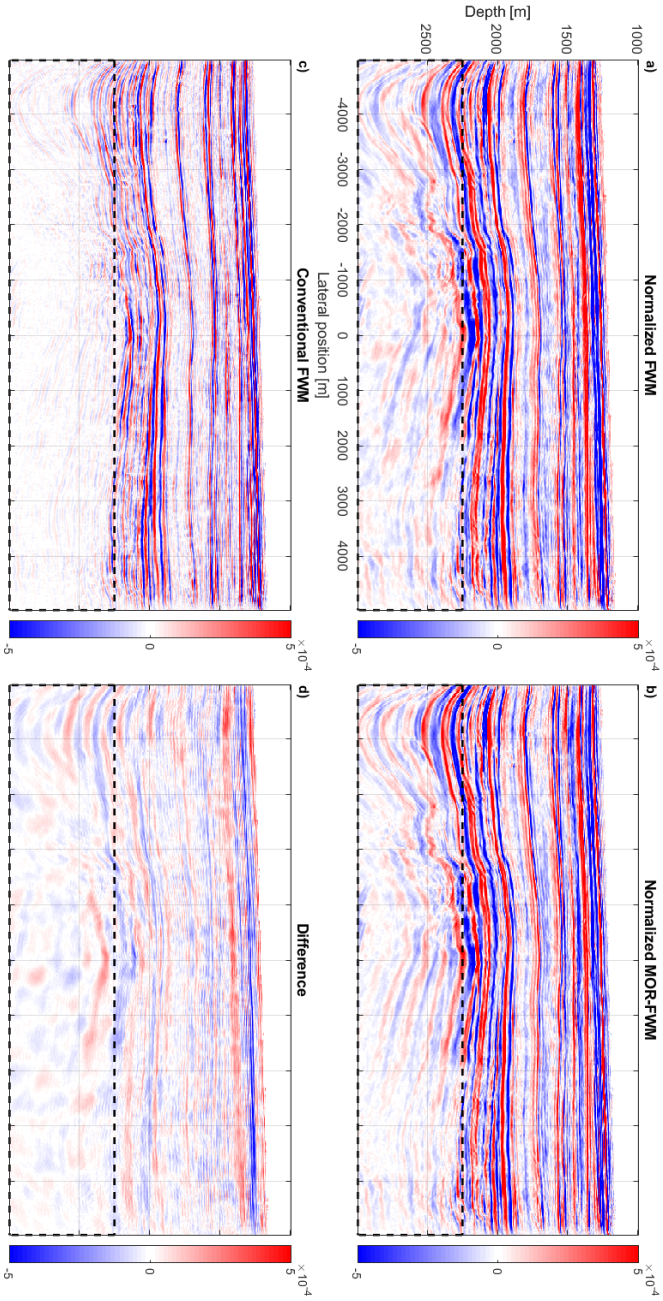

Figure 4.5: FWM and MOR-FWM results for the Vøring field data example. Figures a), b) and d) show the normalized FWM and the normalized MOR-FWM image after 5 iterations, respectively, as well as the difference between the two images. Figure (c) shows the conventional FWM image for comparison. The box indicates the main region of interest in these figures.

REFERENCES

[1] R. Brune, J. Haberkern, S. Wenau, and B. Preu. “Ultra-High-Resolution Marine Seismic Survey for Wind Farm Site Characterization in the German North Sea”. In: *83rd EAGE Annual Conference & Exhibition*. European Association of Geoscientists & Engineers, 2022, pp. 1–5. DOI: 10.3997/2214-4609.202210674. URL: http://dx.doi.org/10.3997/2214-4609.202210674.

[2] J. B. Bednar. “A brief history of seismic migration”. In: *GEOPHYSICS* 70.3 (May 2005), 3MJ–20MJ. ISSN: 1942-2156. DOI: 10.1190/1.1926579. URL: http://dx.doi.org/10.1190/1.1926579.

[3] G. T. Schuster. “Least-squares cross-well migration”. In: *SEG Technical Program Expanded Abstracts 1993*. Society of Exploration Geophysicists, Jan. 1993, pp. 110–113. DOI: 10.1190/1.1822308. URL: http://dx.doi.org/10.1190/1.1822308.

[4] T. Nemeth, C. Wu, and G. T. Schuster. “Least-squares migration of incomplete reflection data”. In: *GEOPHYSICS* 64.1 (Jan. 1999), pp. 208–221. ISSN: 1942-2156. DOI: 10.1190/1.1444517. URL: http://dx.doi.org/10.1190/1.1444517.

[5] G. Dutta, Y. Huang, W. Dai, X. Wang, and G. T. Schuster. “Making the most out of the least (squares migration)”. In: *SEG Technical Program Expanded Abstracts 2014*. Society of Exploration Geophysicists, Aug. 2014, pp. 4405–4410. DOI: 10.1190/segam2014-1242.1. URL: http://dx.doi.org/10.1190/segam2014-1242.1.

[6] G. T. Schuster and W. Dai. “Multi-source Wave Equation Least-squares Migration with a Deblurring Filter”. In: *72nd EAGE Conference and Exhibition incorporating SPE EUROPEC 2010*. European Association of Geoscientists & Engineers, 2010. DOI: 10.3997/2214-4609.201401172. URL: http://dx.doi.org/10.3997/2214-4609.201401172.

[7] A. J. Berkhout. “Review Paper: An outlook on the future of seismic imaging, Part II: Full-Wavefield Migration”. In: *Geophysical Prospecting* 62.5 (Aug. 2014b), pp. 931–949. ISSN: 1365-2478. DOI: 10.1111/1365-2478.12154. URL: http://dx.doi.org/10.1111/1365-2478.12154.

[8] M. Davydenko and D. J. Verschuur. “Full-wavefield migration: using surface and internal multiples in imaging”. In: *Geophysical Prospecting* 65.1 (Feb. 2016), pp. 7–21. ISSN: 1365-2478. DOI: 10.1111/1365-2478.12360. URL: http://dx.doi.org/10.1111/1365-2478.12360.

[9] G. R. Pratt, C. Shin, and G. J. Hick. “Gauss-Newton and full Newton methods in frequency-space seismic waveform inversion”. In: *Geophysical Journal International* 133.2 (May 1998), pp. 341–362. ISSN: 1365-246X. DOI: 10.1046/j.1365-246x.1998.00498.x. URL: http://dx.doi.org/10.1046/j.1365-246X.1998.00498.x.

[10] W. B. Beydoun and M. Mendes. “Elastic Ray-Born L2-Migration/Inversion”. In: *Geophysical Journal International* 97.1 (Apr. 1989), pp. 151–160. ISSN: 1365-246X. DOI: 10.1111/j.1365-246x.1989.tb00490.x. URL: http://dx.doi.org/10.1111/j.1365-246X.1989.tb00490.x.

[11] S. Abolhassani and D. J. Verschuur. “Efficient preconditioned least-squares wave-equation migration”. In: *GEOPHYSICS* 89.3 (Apr. 2024), S275–S288. ISSN: 1942-2156. DOI: 10.1190/geo2023-0048.1. URL: http://dx.doi.org/10.1190/geo2023-0048.1.

[12] J. Hou and W. W. Symes. “An approximate inverse to the extended Born modeling operator”. In: *GEOPHYSICS* 80.6 (Nov. 2015), R331–R349. ISSN: 1942-2156. DOI: 10.1190/geo2014-0592.1. URL: http://dx.doi.org/10.1190/geo2014-0592.1.

[13] H. Chauris and E. Cocher. “From migration to inversion velocity analysis”. In: *GEOPHYSICS* 82.3 (May 2017), S207–S223. ISSN: 1942-2156. DOI: 10.1190/geo2016-0359.1. URL: http://dx.doi.org/10.1190/GEO2016-0359.1.

[14] B. Moore. “Principal component analysis in linear systems: Controllability, observability, and model reduction”. In: *IEEE Transactions on Automatic Control* 26.1 (Feb. 1981), pp. 17–32. ISSN: 0018-9286. DOI: 10.1109/tac.1981.1102568. URL: http://dx.doi.org/10.1109/TAC.1981.1102568.

[15] A. J. Berkhout. “Review Paper: An outlook on the future of seismic imaging, Part I: forward and reverse modelling”. In: *Geophysical Prospecting* 62.5 (Aug. 2014a), pp. 911–930. ISSN: 1365-2478. DOI: 10.1111/1365-2478.12161. URL: http://dx.doi.org/10.1111/1365-2478.12161.

[16] X. Staal. “Combined imaging and velocity estimation by Joint Migration Inversion”. PhD thesis. Delft University of Technology, 2015. DOI: 10.4233/UUID:F9CFA765-DAC4-4954-9B6B-01B8C7345018. URL: http://resolver.tudelft.nl/uuid:f9cfa765-dac4-4954-9b6b-01b8c7345018.

[17] J. W. Thorbecke and D. Draganov. “Finite-difference modeling experiments for seismic interferometry”. In: *GEOPHYSICS* 76.6 (Nov. 2011), H1–H18. ISSN: 1942-2156. DOI: 10.1190/geo2010-0039.1. URL: http://dx.doi.org/10.1190/geo2010-0039.1.

[18] S. Abolhassani and E. Verschuur. “High-Resolution One-Way Reflection Waveform Inversion”. In: *84th EAGE Annual Conference & Exhibition*. European Association of Geoscientists & Engineers, 2023, pp. 1–5. DOI: 10.3997/2214-4609.202310517. URL: http://dx.doi.org/10.3997/2214-4609.202310517.

[19] A. J. Berkhout. “Review Paper: An outlook on the future of seismic imaging, Part III: Joint Migration Inversion”. In: *Geophysical Prospecting* 62.5 (Aug. 2014c), pp. 950–971. ISSN: 1365-2478. DOI: 10.1111/1365-2478.12158. URL: http://dx.doi.org/10.1111/1365-2478.12158.

5

CONCLUSIONS AND FUTURE WORK

5.1. CONCLUSIONS

Full-Wavefield Migration (FWM) is a powerful method for making images of the subsurface of the Earth. It belongs to the class of Least Squares Migration (LSM) methods, which function by iteratively updating the image of the subsurface, based on the misfit between the true data and the forward modelled wavefield at the surface. FWM has several advantages over other imaging methods, most noticeably its low computational cost and the fact that it incorporates multiple scattering effects into the imaging algorithm.

However, there is still significant room for the FWM algorithm to be improved. One area that is of particular interest is the inclusion of converted waves into the FWM framework. In areas with large contrasts, failure to take converted waves into account leads to significant degradation of the image. FWM is well-suited to incorporate these effects in principle, due to its use of integral-based operators, which allow for coarser grids to be used compared to finite-difference-based methods. This leads to an important reduction in computational cost, which is a significant challenge in the modelling and imaging of converted waves.

The primary contribution of this thesis is the development of an extension to the acoustic FWM algorithm which takes converted waves into account. In order to successfully incorporate wave conversions into FWM, accurate elastic reflection and transmission operators are required. However, the true elastic reflection and transmission coefficients, known as the Zoeppritz equations, are notoriously non-linear, making them difficult to work with. To circumvent this issue, we have presented a set of accurate approximations to the Zoeppritz equations in chapter 2, based on taking Taylor expansions of the true elastic reflection and transmission coefficients. These approximations, which we have named the extended Shuey approximations, reduce the non-linearity of the full Zoeppritz equations, making them easier to work with in forward modelling and inversion. To benchmark these extended Shuey approximations, we have compared them to other approximations in literature, where we have shown that the extended Shuey approximations are more accurate in areas with large contrasts. We have also shown that the extended Shuey approximations lead to more accurate results in a simple, 1.5D modelling and

inversion case, compared to the conventional Shuey approximation.

Next, in chapter 3, we have used these extended Shuey approximations, along with the theoretical framework developed by Berkhout [1], to develop a robust, elastic FWM algorithm which takes converted waves into account. By using the extended Shuey approximations, we are able to formulate accurate reflection and transmission operators which are linked through the underlying medium parameters. Doing this allows us to avoid the overparameterisation problem which is otherwise present when incorporating angle-dependent reflection and transmission operators into FWM. We have succesfully tested the resulting elastic FWM method on two synthetic models, providing a proof-of-concept. Also, we have shown that in the models examined, the elastic FWM algorithm outperforms the conventional, acoustic FWM method. This shows the importance of taking converted waves into account when imaging areas with large contrasts.

Finally, we have examined the convergence of the conventional, acoustic FWM method. A known issue of FWM, and LSM methods in general, is their speed of convergence. To improve this, preconditioning is often applied to the gradient, in order to improve the update direction. In chapter 4, we have presented a novel preconditioner, based on approximating the pseudo-inverse using Proper Orthogonal Decomposition (POD). Using this method, we have achieved improved imaging results compared to the conventional FWM algorithm for both the synthetic Marmousi model as well as for a field dataset from the Vøring basin in Norway.

Consequently, this work presents several advancements in the field of FWM.

5.2. FUTURE WORK

In this section we will discuss some potential future areas of research related to the FWM algorithm.

5.2.1. INCORPORATING AVO EFFECTS IN ACOUSTIC FWM

As discussed in chapter 3, one of the main challenges in incorporating angle-dependent reflection and transmission operators in the conventional, acoustic FWM algorithm is the danger of overparametrisation. Therefore, in chapter 2, we introduced a set of accurate approximations to the full, elastic reflection and transmission operators, which are linked through the underlying medium parameters. Using these approximations, we are able to avoid the issue of overparametrisation when formulating the elastic FWM algorithm of chapter 3.

However, this approach can also easily be applied to the conventional, acoustic FWM algorithm. By replacing the angle-independent reflection operator commonly used in acoustic FWM with the approximate PP-reflection operator $\mathbf{R}^{\cup}_{PP}$ introduced in chapter 3, we can take angle-dependent reflectivity effects into account without incurring the additional computational costs associated with full, elastic FWM. This is relevant, as these angle-dependent reflectivity effects, more commonly known as amplitude-versus-offset (AVO) effects, can degrade the image if they are not taken into account properly. Therefore, using this approach, more accurate images may be created in areas which exhibit strong AVO effects.

5.2.2. ELASTIC JOINT MIGRATION INVERSION

As we have discussed briefly in chapter 3, the elastic FWM method introduced in this thesis can be used as a basis for the development of a so-called elastic Joint Migration Inversion (JMI) algorithm. JMI, also known as one-way Reflection Waveform Inversion (ORWI) [2], is a joint velocity and reflectivity estimation method, based on the conventional, acoustic FWM algorithm [3, 4]. In a similar way, an elastic JMI algorithm, which takes converted waves into account, can be developed based on the elastic FWM algorithm.

The main challenge in the development of elastic JMI is the fact that one needs to estimate the *S*- and *P*-wave velocity models simultaneously. In principle, this extension is straightforward, as it is similar to the extension of the propagation operators described in chapter 3. However, in practice the estimation of an accurate velocity model is challenging [5], requiring additional research in order to develop a robust method for combining velocity and reflectivity estimation in elastic JMI.

5.2.3. OMNI-DIRECTIONAL IMAGING

A key challenge for FWM is the imaging of steep reflectors and diving waves. As FWM is based on one-way operators, it cannot take horizontally propagating waves into account. Furthermore, it assumes that downgoing waves are only turned into upgoing waves due to scattering at a reflector. Unfortunately, this is not the case for diving waves, which go from downgoing to upgoing waves due to variations in the velocity profile. Therefore, the conventional FWM framework cannot take these waves into account, leading to inaccurate images in areas with strong diving waves and/or steep reflectors.

While multiple attempts have been made to take these effects into account [6, 7], a comprehensive, omni-directional framework has remained elusive. However, as the FWM method is extended to include more angle-dependent effects, it becomes increasingly important to develop such a framework. In particular, the method currently used to take dipping reflectors into account in elastic FWM, described in chapter 3, is only valid for small dipping angles. In order to take steep reflectors into account, it is therefore important to revisit the challenge of omni-directional imaging in FWM.

5.2.4. FREQUENCY INTERPOLATION

As the focus of seismic imaging slowly shifts away from the exploration of hydrocarbon resources and towards alternative applications, the computational cost of seismic imaging has come under increased scrutiny. While the computational cost of FWM is significantly lower than that of other LSM methods, especially those based on full, two-way finite-difference modelling, its cost is not insignificant.

The main factor in the computational cost of FWM is the need to calculate and store the modelled wavefields for each frequency independently. Therefore, the computational cost of the method can be reduced significantly by only calculating the wavefields for a limited number of frequencies. Using interpolation methods, the wavefields for frequencies which have not been evaluated explicitly can be

recovered. In this manner, both the overall computational cost as well as the memory requirements of the method can be significantly reduced. Initial research into this topic has already begun, most noticeably by Zhao et al. [8], who use machine learning to perform the interpolation. Alternatively, one can use a deterministic method such as POCS [9] to interpolate the missing frequencies.

5.2.5. EXTENSION TO 3D

Finally, as discussed briefly in chapter 3, the elastic FWM algorithm presented in this thesis can be extended to 3D applications. In 3D, the one-dimensional convolutions of the 2D method need to be replaced with two-dimensional convolutions to account for the propagation and scattering in three dimensions. Also, in order to properly incorporate all elastic effects, it is necessary to take S_H waves into account, as well as the S_V waves that we have discussed in this thesis. In principle, these waves can be taken into account using the same framework discussed in chapter 3. However, this will introduce additional complexity into the presented algorithm, requiring further research to properly take into account.

REFERENCES

[1] A. J. Berkhout. “Review Paper: An outlook on the future of seismic imaging, Part I: forward and reverse modelling”. In: *Geophysical Prospecting* 62.5 (Aug. 2014a), pp. 911–930. ISSN: 1365-2478. DOI: 10.1111/1365-2478.12161. URL: http://dx.doi.org/10.1111/1365-2478.12161.

[2] S. Abolhassani and E. Verschuur. “High-Resolution One-Way Reflection Waveform Inversion”. In: *84th EAGE Annual Conference & Exhibition*. European Association of Geoscientists & Engineers, 2023, pp. 1–5. DOI: 10.3997/2214-4609.202310517. URL: http://dx.doi.org/10.3997/2214-4609.202310517.

[3] A. J. Berkhout. “Review Paper: An outlook on the future of seismic imaging, Part III: Joint Migration Inversion”. In: *Geophysical Prospecting* 62.5 (Aug. 2014c), pp. 950–971. ISSN: 1365-2478. DOI: 10.1111/1365-2478.12158. URL: http://dx.doi.org/10.1111/1365-2478.12158.

[4] X. Staal. “Combined imaging and velocity estimation by Joint Migration Inversion”. PhD thesis. Delft University of Technology, 2015. DOI: 10.4233/UUID:F9CFA765-DAC4-4954-9B6B-01B8C7345018. URL: http://resolver.tudelft.nl/uuid:f9cfa765-dac4-4954-9b6b-01b8c7345018.

[5] S. Abolhassani. “One-way Reflection Waveform Inversion: Migration and Tomography”. PhD thesis. Delft University of Technology, 2025.

[6] M. Davydenko. “Full wavefield migration: Seismic imaging using multiple scattering effects”. PhD thesis. Delft University of Technology, 2016. DOI: 10.4233/UUID:1CDA75D5-8998-49FE-997E-B38C9B7F8B8B. URL: http://resolver.tudelft.nl/uuid:1cda75d5-8998-49fe-997e-b38c9b7f8b8b.

[7] S. Masaya. “Seismic imaging based on Joint Migration Inversion”. PhD thesis. Delft University of Technology, 2018. DOI: 10.4233/UUID:4B348428-50DC-4594-90F0-FC1BF90661A2. URL: http://resolver.tudelft.nl/uuid:4b348428-50dc-4594-90f0-fc1bf90661a2.

[8] J. Zhao, N. Akram, N. Savva, and E. Verschuur. “Accelerating 2-D Full Wavefield Forward Modeling via Frequency Interpolation with a Tiny Attention U-Net Based Model”. In: *Eighth EAGE High Performance Computing Workshop*. European Association of Geoscientists & Engineers, 2024, pp. 1–3. DOI: 10.3997/2214-4609.2024636006. URL: http://dx.doi.org/10.3997/2214-4609.2024636006.

[9] K. Iranpour, T. Elboth, S. Tuppen, S. Sachdeva, J. Sun, and D. Van Manen. “Interpolation of Missing Frequencies”. In: *85th EAGE Annual Conference & Exhibition*. European Association of Geoscientists & Engineers, 2024, pp. 1–5. DOI: 10.3997/2214-4609.202410370. URL: http://dx.doi.org/10.3997/2214-4609.202410370.

ACKNOWLEDGEMENTS

This thesis is the culmination of 6 years of my life, and during that time I have had the great fortune to meet a large number of amazing people, a number of whom I want to thank explicitly here.

First of all, I would like to thank dr. **Koen van Dongen**, my main supervisor throughout my PhD, without whom this thesis would never have existed. Koen, we met when I was looking for a research project during my Master's and worked together shortly during that time. Later, you introduced me to Eric for a possible PhD project, which I ended up taking and during which you once again became my primary supervisor. I have always greatly enjoyed working with you, and without your guidance, weekly check-ins and attention to detail this thesis would have never been finished. I also want to explicitly thank you for always believing in me and the project, even during times where many doubted it would ever reach the finish line. Your loyalty and trust towards your students is an amazing quality, and one which is very highly appreciated by all of your students.

Secondly, I want to thank dr. **Eric Verschuur**, my promotor and main supervisor for the first two years of my PhD. Eric, your knowledge and insight in the field of geophysics never ceases to amaze me. Many times I have explained an issue to you, and within seconds you not only understood the exact problem I was facing but had already come up with multiple potential solutions. As the head of the Delphi consortium, you are involved with many many projects, but you always make time for your students and foster an environment of collaboration and friendliness, which makes it a joy to work within Delphi. Thank you for giving me the opportunity to do a PhD and for the superhuman amount of work you do for Delphi and for your students.

Next, I want to thank prof. **Kees Wapenaar**, prof. **Martin van Gijzen**, prof. **Tristan van Leeuwen**, dr. **Peter Haffinger** and dr. **Matteo Ravasi** for being part of my defence committee, and for their insightful comments and remarks on the thesis. Special thanks to Peter Haffinger and Matteo Ravasi for their effort in compiling very thorough feedback on the thesis.

Also thanks to the wonderful support staff at the Computational Imaging department. **Angela** and **Annelies**, thank you for making everything in the department run smoothly and helping me with the contract issues that arose during the years. **Henry** and **Ronald**, thank you for making sure all the computers, clusters and other machines keep running smoothly. Special thanks to Ronald for his comprehensive guide to using the HPC cluster, without which I would have been completely lost. Finally, thanks to **Gerrie** for all her work in ensuring that the Delphi meetings ran smoothly, doing a lot of work behind the scenes so that the students only needed to worry about their presentations.

I also want to thank my lovely colleagues, whom I have learnt a lot from and who have made this whole journey much more enjoyable. First of all, I want to thank my co-authors, **Muhammad Hamza Khalid** and **Joost van der Neut**. Hamza, it has been a

great pleasure both working with you and becoming good friends. Being at your wedding and visiting your home country of Pakistan was definitely one of the highlights of my PhD time! Joost, thank you for your insight and support in getting the elastic FWM algorithm to work. I always appreciate your insightful perspectives, both on work and on life in general.

Next, I want to thank the 'old-guard' of Delphi: **Shan**, **Aparajita**, **Tiexing**, **Billy**, **Andreas**, **Mikhail**, **Apostolos**, **Jan-Willem**, **Nick**, **Bouchaib**, **Matteo**, **Aayush**, **Sixue**, **Aydin**, **Anyu**, **Dieter** and **Inez**. Thank you for incorporating me into the Delphi group and teaching me about seismic imaging and geophysics. I also want to thank the members of 'Delphi 2.0': **Camille**, **Andrea**, **Sverre**, **Boris**, **Sijmen**, **Matthijs**, **Azin**, **Mohammed**, **Alireza** and **Jaihua**. Having gotten to know you all I am convinced that the future of Delphi is in very good hands! Thanks to all of you for the nice dinners, good conversation and general good vibes during the Delphi meetings in Houston and the Hague. Thanks also to my colleagues in the Computational Imaging department: **Qingru**, **Wenxiu**, **Jos**, **Yan**, **Christiaan**, **Enya**, **Loes**, **Kote** and **Sobhan**. While our work is in very different areas, I appreciate the conversations and social meetups we have had in the department. Special thanks to **Peter** for dropping in to my office from time to time with interesting conversations and updates.

Finally, I want to give special thanks to my colleagues and friends from room F230, Delphi 0.0, the old fossils. **Ali**, thank you for your initiative, for being the impetus for so many spontaneous dinners, lunches, board game nights and other activities which really livened up the whole PhD process. I look back very fondly on our lively (and sometimes borderline heated) discussions in the office and at lunch, you made sure our time at the office was never boring. **Siamak** (and **Sanaz**!), thank you for all the lunches we have had together, your support during the (slightly stressful) final months of my PhD and beyond, and for all the interesting technical discussions we have had together. You are a true and genuine friend, and I thank you for that. **Dong**, my 'big brother', thank you for helping me find my footing in the world of geophysics, thank you for all the Chinese dinners and board game nights we spent together, and thank you for all the interesting dicussions and conversations we have had over the years. I have learned a lot from you, both in terms of geophysics as well as in terms of life in general. Most of all, thank you for our trips to New York, Lissabon, and, most importantly, China, to come to your wedding! I look back on these trips very fondly, and they have been the highlight of my PhD journey.

Next, I want to thank my amazing friends, without whom I would have lost my sanity multiple times throughout this process. I want to begin by thanking my teammates and friends from my badminton club, BC Randstad, all of whom mean a lot to me. **Vincent**, thank you for being a great doubles partner and a great friend. Also thank you for actively coaching all of us to make us better, smarter and more technical players. **Bob**, thank you for all the board game nights we have spent together, and putting up with my teasing when things don't go your way. Also special thanks for setting up an online Pandemic game using nothing but a webcam, a pile of books and a laptop during Covid, which remains one of my favorite memories from that time. **Martin**, thank you for your beautifully crafted DnD one-shots, and thank you for all the work you have put into the Randstad Open over the years. In the times when I have been away I never worry about the tournament, because I know that it is in your, very capable, hands. **Emeline**, thank

you for all the delicious cakes and cookies and meals that you have prepared for us over the years! I always look forward to our matches, knowing that there will be an amazing cake waiting at the end of them. **Vera**, thank you for your friendship, and for being a sounding board for me in times when I have needed it. While I may soon have a PhD in physics, you have a PhD in being a kind, genuine and thoughtful friend. Finally, **Linda**, thank you for your optimism, thank you for your kindness, and thank you for always being there for me with good advice and open ears. I really appreciate all our talks, you always bring an interesting and thoughtful perspective to all of our discussions, and you actively try to make my life better and more organized, which I really appreciate. To all of you, thank you for the matches, the board game nights, the DnD sessions, and the overall gezelligheid!

Next, I want to thank my friends from the Technische Natuurkunde Bachelor. **Ronald** (and **Tessa**!), thank you for all the concerts and festivals we have been to together, you have opened my eyes to the joy of live music, for which I am very grateful. **Jelte**, thank you for your activism, and for encouraging us to follow in your footsteps. **Wesley**, thank you for our lively conversations, and for being one my oldest friends. Finally, **Christian**, thank you for getting me through the experimental courses during our Bachelor's, thank you for all the projects we have done together, and thank you for your friendship and support, both technical and non-technical. To all of you, I look back fondly on our times together at university, and I am very glad that we still remain good friends to this day!

I also want to thank my friends from the 'Delft 3.0 DnD group'. **Marijn**, thank you for the board game nights and especially the Cube drafts you have hosted, which have inspired me to make a Cube of my own which gives me great joy. **Boudewijn**, thank you for all the weird and wonderful music you have introduced to me, and thank you for always being, absolutely and without hesitation, yourself. **Stijn**, thank you for the (slightly chaotic) energy you always bring to our sessions, you always add a lot of flair (and some headaches for me as a DM) to our sessions. Finally, **Felix** (and **Brechje**!), thank you for being an amazing friend for all these years. I look back very fondly to the wars we fought out over the Warhammer tables, the beautiful Wie is de Mol weekends you have organized, and the many, many hours we have spent playing all sorts of games. To all of you, thank you for the energy and wild plans you bring to our DnD sessions!

Next, I want to thank my ClayChild band mates: **Erik**, **Kimm** and **Marieke**. Making music together is a beautiful experience, each note falling into place and become much more than the sum of its' parts. Being able to leave everything behind for a few hours and just focus on making music has been very good for me over the years. It also definitely helps that all three of you are lovely, kind and genuine people! Here's to our path to world domination!

Finally, I want to thank three people who do not fit neatly into any of the previous categories. **Sander** (and **Leron**!), thank you for all the board games and video games we have played together over the years. We have fought the War of the Ring countless times, have terraformed the land of Terra Mystica many, many times over, and have died to the aliens of Nemesis more times than I can count. Thank you for introducing me to so many wonderful and amazing games, thank you for all the countless, delicious meals you have cooked over the years, and above all, thank your being such a good friend. **Pascal**, thank you for keeping me in shape throughout this whole process. I never thought I would be

someone that went to the gym, but thanks to you I am now in better shape than I have ever been. Thank you for all your slightly insane training plans (who goes to the gym for 24 hours straight!?), thank you for your unique perspectives on life, and thank you being my friend for so many years. Also thanks to you and **Pishella** for coming to so many ClayChild shows! I wish you both lots of love and happiness in the new stage of your life. Finally, **Eveline**, thank you for being a very close friend over all these years. Thank you for being my mixed doubles partner for so many tournaments, thank you for all the open conversations and talks we have had, and thank you for being my sounding board whenever I have needed it. Even now that you live in Australia, we have still remained close friends, and I hope we will remain good friends for many, many years.

Last, but certainly not least, I want to thank my family. My extended family, **Niek** and **Tanya**, **Sjef**, **Franciska**, **Ilse** and **Wouter**, **Rian**, **Wim** and **Yiannis**, **Ronald** and **Marion**, and **Thomas** and **Sandra** (and **Joep** and **Maud**!), thank you for all your support over the years and for the old-fashioned, Hollandse gezelligheid during countless birthday parties and other gatherings. Special thanks to Niek and Tanya, for the wild and wonderful board games we have tested over the years. They say you cannot choose your family, but I could not wish for a better one. Finally, I want to thank my parents, **Peter** and **Paulien**. There is so much to thank you for that I don't even know where to start. Let me just say thank you for being wonderful parents, thank you for all your support over the years, and thank you for always providing a safe haven for me. I definitely don't say this enough, but I love you.

(And, as a little post-scriptum: if you get bored during all the technical discussions during the defense, which is completely understandable, here's a little puzzle to make the process more enjoyable ;). Feel free to try your hand at it during the defense, I put it in specifically for that reason after all)

7				3	6		4	
	4		1				7	
3						1		
5	3							
2		9	6	4				
	6		9	7			8	
	2		7		4			5
					8			4
	5	4		6	9			1

Curriculum Vitæ

Leonard Arie Hoogerbrugge

02-07-1993	Born in Voorburg, the Netherlands.

Education

2011–2014	B.Sc. Applied Physics Delft University of Technology, the Netherlands
2014–2018	M.Sc. Applied Physics Delft University of Technology, the Netherlands
2018–2025	PhD. Applied Physics Delft University of Technology, the Netherlands

List of Publications

Journal papers

6. **L. Hoogerbrugge**, K. W. A. van Dongen, and D. J. Verschuur. "Extending Shuey's approximation using Taylor expansions for forward and inverse modelling". In: *Geophysical Journal International* (Undergoing review)

5. **L. Hoogerbrugge**, J. R. van der Neut, K. W. A. van Dongen, and D. J. Verschuur. "Including converted waves using Shuey's approximation in elastic Full-Wavefield Migration". In: *Geophysical Journal International* (Undergoing review)

4. **L. Hoogerbrugge**, M. H. Khalid, K. W. A. van Dongen, and D. J. Verschuur. "Model-Order Reduced Full-Wavefield Migration using Proper Orthogonal Decomposition". In: *Geophysical Journal International* (Undergoing review)

3. S. Abolhassani, **L. Hoogerbrugge**, and D. J. Verschuur. "One-way reflection waveform inversion with depth-dependent gradient preconditioning". In: *Geophysical Journal International* (Nov. 2024). ISSN: 1365-246X. DOI: 10.1093/gji/ggae397. URL: http://dx.doi.org/10.1093/gji/ggae397

2. T. Schaeken, **L. Hoogerbrugge**, and E. Verschuur. "A non-reflecting wave equation through directional wave-field suppression and its finite difference implementation". In: *Scientific Reports* 12.1 (Jan. 2022). ISSN: 2045-2322. DOI: 10.1038/s41598-021-04064-3. URL: http://dx.doi.org/10.1038/s41598-021-04064-3

1. D. J. G. Pearce, **L. Hoogerbrugge**, K. A. Hook, H. S. Fisher, and L. Giomi. "Cellular geometry controls the efficiency of motile sperm aggregates". In: *Journal of The Royal Society Interface* 15.148 (Nov. 2018), p. 20180702. ISSN: 1742-5662. DOI: 10.1098/rsif.2018.0702. URL: http://dx.doi.org/10.1098/rsif.2018.0702

Conference papers

5. **L. Hoogerbrugge**, K. van Dongen, and E. Verschuur. "Elastic Full Wavefield Migration Using Shuey's Approximation". In: *85th EAGE Annual Conference & Exhibition*. European Association of Geoscientists & Engineers, 2024, pp. 1–5. DOI: 10.3997/2214-4609.2024101641. URL: http://dx.doi.org/10.3997/2214-4609.2024101641

4. J. van der Neut, **L. Hoogerbrugge**, K. van Dongen, and E. Verschuur. "Elastodynamic Full Wavefield Modelling with Legendre Polynomials". In: *84th EAGE Annual Conference & Exhibition*. European Association of Geoscientists & Engineers, 2023, pp. 1–5. DOI: 10.3997/2214-4609.202310309. URL: http://dx.doi.org/10.3997/2214-4609.202310309

3. **L. Hoogerbrugge**, K. van Dongen, and E. Verschuur. “Interface Contrast Imaging for Omni-Directional Full Wavefield Migration”. In: *83rd EAGE Annual Conference & Exhibition*. European Association of Geoscientists & Engineers, 2022, pp. 1–5. DOI: 10.3997/2214-4609.202210648. URL: http://dx.doi.org/10.3997/2214-4609.202210648

2. **L. Hoogerbrugge** and E. Verschuur. “Including Converted Waves in Full Wavefield Migration”. In: *82nd EAGE Annual Conference & Exhibition*. European Association of Geoscientists & Engineers, 2021, pp. 1–5. DOI: 10.3997/2214-4609.202011693. URL: http://dx.doi.org/10.3997/2214-4609.202011693

1. E. Verschuur and **L. Hoogerbrugge**. “A Modular Wavefield Inversion Process, Including Internal Multiples, Transmission and Converted Waves”. In: *82nd EAGE Annual Conference & Exhibition - Workshop Programme*. European Association of Geoscientists & Engineers, 2021, pp. 1–4. DOI: 10.3997/2214-4609.202012140. URL: http://dx.doi.org/10.3997/2214-4609.202012140